FOSSIL ENERGY

DOE/BC/14994-12
OSTI ID: 9324

MODELING PERMEABILITY ALTERATION IN DIATOMITE RESERVOIRS DURING STEAM DRIVE

SUPRI TR 113

RECEIVED
AUG 2 5 1999
OSTI

By
Suniti Kumar Bhat
Anthony R. Kovscek

July 1998

Work Performed Under Contract No. DE-FG22-96BC14994

Stanford University
Stanford, California

National Petroleum Technology Office
U. S. DEPARTMENT OF ENERGY
Tulsa, Oklahoma

DOE/BC/14994-12
Distribution Category UC-122

Modeling Permeability Alteration in Diatomite Reservoirs During Steam Drive

SUPRI TR 113

By
Suniti Kumar Bhat
Anthony R. Kovscek

July 1998

Work Performed Under Contract DE-FG22-96BC14994

Prepared for
U.S. Department of Energy
Assistant Secretary for Fossil Energy

Thomas Reid, Project Manager
National Petroleum Technology Office
P.O. Box 3628
Tulsa, OK 74101

Prepared by
Stanford University
Petroleum Engineering Department
65 Green Earth Sciences Bldg.
Stanford, CA 94305

Table of Contents

List of Tables

List of Figures

Abstract

There is an estimated 10 billion barrels of original oil in place (OOIP) in diatomaceous reservoirs in Kern County, California. These reservoirs have low permeability ranging from 0.1 to 10 mD. Injection pressure controlled steam drive has been found to be an efficient way to recover oil from these reservoirs. However, steam drive in these reservoirs has its own complications.

The rock matrix is primarily silica (SiO_2). It is a known fact that silica is soluble in hot water and its solubility varies with temperature and pH. Due to this fact, the rock matrix in diatomite may dissolve into the aqueous phase as the temperature at a location increases or it may precipitate from the aqueous phase onto the rock grains as the temperature decreases. Thus, during steam drive silica redistribution will occur in the reservoir along with oil recovery. This silica redistribution causes the permeability and porosity of the reservoir to change. Understanding and quantifying these silica redistribution effects on the reservoir permeability might prove to be a key aspect of designing a steam drive project in these formations.

In this study the first aspect that we examine is the relative importance of the factors that govern the transfer of silica between the rock matrix and the aqueous phase. On the basis of analytical solutions for simple one-dimensional systems and the conditions that typically exist in diatomite reservoirs, we conclude that the silica concentration in the aqueous phase is the equilibrium silica solubility corresponding to the temperature of that location. This is likely true for the whole length of the reservoir, except near injectors and producers. We call this attainment of "local chemical equilibrium". This implies for a given location, that when we know the temperature variation, we can predict the amount of silica transfer between rock grains and the aqueous phase surrounding it.

From a qualitative argument we know that the extent of permeability alteration will depend on the pore-level characteristics of this rock apart from the extent of silica redistribution. We tried to infer the pore-level shapes and distributions of pore-sizes of this rock by a variety of experimental methods including mercury intrusion / retraction porosimetery, scanning electron microscopy, core-level permeability measurements and X-ray computed tomography (CT scanning). On basis of these investigations we inferred the shape of pore-body and pore-throat size distributions for an outcrop sample of diatomite. These were unimodel distributions with a high positive skew. The average pore-throat size was around 6 μm and the average pore-body size was around 40 μm.

In the final phase of this study, we found mathematical relations that are useful to predict the permeability alteration with amount of silica transfer between the rock matrix and the aqueous phase given the pore-level information of diatomite. This was done using pore-network models. To start, we correlated the pore dimensions with properties like permeability and porosity. Next, we modeled the deposition / dissolution processes in terms of changing pore dimensions and then used these altered pore dimensions to find the altered permeability and porosity. This way, we were able to quantify the effect of silica redistribution on permeability of the reservoir.

Acknowledgements

This work was supported by the U.S. Department of Energy, under contract No. DE-FG22-96BC14994 to Stanford University and from the SUPRI A Industrial Affiliates Program. Partial support was also provided by Lawrence Livermore National Laboratory under contract No. DE-AC03-76SF00098 to the University of California.

1. INTRODUCTION

There are a large number of diatomaceous petroleum reservoirs in Kern County, California. These fields include South Belridge, North Belridge, Cymric, Midway Sunset and Lost Hills diatomite. Collectively, they contain an estimated 10 billion barrels of original oil in place (OOIP) (Ilderton *et al.,* 1996*)*. The diatomaceous formations in these areas are thick, highly layered, and relatively shallow (1000-2000 ft.). They are primarily composed of the consolidated remains of microscopic single-cell aquatic plankton called diatoms. They are primarily siliceous formations.

Experience is beginning to show that steam drive with careful control of injection pressure can be an efficient technique for oil recovery from siliceous reservoirs that are relatively shallow, low permeability, thick, and highly layered. In the case of steam drive, recovery occurs by direct displacement of oil by steam and condensate and also by volumetric expansion of oil due to thermal conduction of heat through the formation. In contrast, water flood recovery relies on direct physical contact of water with the oil in the reservoir.

Steam injection has been used successfully to recover heavy and light oil from the South Belridge and Cymric diatomite (Kovscek *et al.*, 1997; Kumar and Beatty, 1995; Johnston and Shahin, 1995; Murer *et al.*, 1997; Kovscek *et al.*, 1996; and Kovscek *et al.*, 1996). They have permeability ranging from about 0.1 mD to 10 mD (Schwartz, 1988 and Stosur and David, 1971) and porosity that ranges from 38 % to 65 % (Schwartz, 1988 and Stosur and David, 1971). The low permeability results from extremely small-sized pore throats usually 1 to 6 μm in diameter. Steam injection into diatomite is not without complications. One factor is the solubility of diatomite in hot water. Diatomite is a hydrous form of silica or opal composed of microscopic shells of diatoms that are the remains of single-celled microscopic aquatic plankton. During steam injection, diatomite, which is principally silica (SiO_2) can dissolve in hot aqueous condensate and this dissolved silica is carried forward by the moving condensate. As the condensate travels away from the injector, it cools and the dissolved silica precipitates. Experiments (Koh *et al.*, 1996) where silica-laden hot water was injected into diatomite suggest that silica deposition in diatomite leads to plugging. Later, the deposited silica may dissolve again if the local temperature increases. This process causes permeability redistribution within the reservoir, which is already relatively impermeable. Similarly, silica dissolution might increase permeability around the injection wells, thereby improving injectivity.

Silica deposition could also be a concern for waterflood operations. In the San Joaquin Valley, diatomaceous reservoirs underlay permeable sands containing heavy oil (Schwartz, 1988). This heavy oil is recovered by steam injection. Produced hot condensate from the heavy oil recovery operations is sometimes re-injected in the diatomites. These waters are frequently laden with silica that might precipitate when contacting the cooler diatomaceous reservoirs.

To quantify changes in permeability that occur in diatomite during silica dissolution and precipitation we need to take into account the transient heat and mass transfer processes that could possibly affect the process of permeability change. For example, during hot fluid injection into the reservoir, there will be a temperature profile in the reservoir at any given instant of time. This temperature profile will propagate with time. At locations within the reservoir where water is heated or cooled, there can be silica transfer between the rock phase and the hot water. The extent of this transfer will depend on the relative magnitudes of the competing mechanisms of rate silica deposition/ dissolution and the bulk movement of silica in the fluid due to advection through the pore spaces. The magnitude of silica deposition/ dissolution will be dependent on factors such as temperature, reaction mechanism, pH and the rate of fluid movement (Thornton and Radke, 1988; Saneie and Yortsos, 1985; Bunge and Radke, 1982; and Udell and Lofy, 1989). Finally, the extent of permeability alteration that occurs in diatomite due to silica diagenesis will depend also on the pore-level characteristics of the rock.

In this report, we have studied the last three aspects in some detail. We assume that given a heat injection rate into the formation there are adequate simulation tools existing in practice that could help in predicting the temperature profiles at some given instant of time during the steam injection process. The rest of the problem has been divided into three major tasks:

- Given some temperature conditions at a given location, we determine the amount of silica transfer that occurs between the diatomite rock matrix and the fluid moving through it. We also determine the dominating factors that govern the silica transfer the between the diatomite rock matrix and the moving fluid phase.
- Next, we try to characterize the diatomite rock using experimental techniques such as scanning electron microscopy (SEM), X-ray computed tomography (CT), and mercury intrusion porosimetery to determine the pore-level and core-level properties of the rock .
- Finally, we quantify the effect of diagenesis on the permeability of a porous medium. We develop a network model and incorporate evolving pore shapes. The concepts of percolation theory are used to predict the effects of dissolution and deposition on permeability and porosity of the porous medium. We consider only the flow of liquid water in this study. To model the diagenetic process, various dissolution and deposition patterns are considered.

The following chapters of this report describe in detail the approach we use to study these aspects of silica diagenesis in diatomite. In Chapter 2, we describe our study of the kinetics of silica dissolution and deposition. Also examined is the role that those kinetics play during hot fluid injection specifically in the case of diatomite given the temperature and flow conditions that typically are seen in diatomite. In Chapter 3, we describe the methods that we use to characterize the pore-level properties of diatomite. We characterize the porous medium using methods such as scanning electron microscopy, CT imaging and mercury intrusion porosimetery. In Chapter 4, we discuss the modeling strategy that we have used to study the effects of diagenesis given the pore-level information that we obtained experimentally.

2. Kinetics Modeling

2.1 Introduction

Understanding the kinetics of silica dissolution and precipitation is an important facet of predicting permeability changes due to silica redistribution in diatomite. The problem of silica kinetics has been studied extensively in the literature (Koh *et al.*, 1996; Saneie and Yortsos, 1985; Thornton and Radke, 1988; Bunge and Radke, 1982; Dehghani, 1983; Mohnot, *et al.*, 1984; Bohlmann *et al.*, 1980; and Rimstidt and Barnes, 1980) in regard to alkaline flooding and steam flooding in sandstone. It has already been shown that the silica dissolution mechanism depends on factors such as pH, temperature, pressure, and the presence of other ionic species in the aqueous phase (Koh *et al.*, 1996; Saneie and Yortsos, 1985; Thornton and Radke, 1988; Bunge and Radke, 1982; Dehghani, 1983; Mohnot, *et al.*, 1984; Bohlmann *et al.*, 1980; and Rimstidt and Barnes, 1980). For diatomite, previous studies also indicate that the flowing aqueous solution is buffered by diatomite and a pH in the vicinity of 8 is always maintained (Bruton, 1996). For this range of pH and temperature around $300^{\circ}C$, which corresponds roughly to the steam injection pressure in diatomite, the reaction mechanism is a first order reaction (Dehgani, 1983; Mohnot *et al.*, 1984). We use the first order mechanism of silica dissolution/ precipitation, and, then solve the advective-reactive transport equation for silica analytically using Laplace transforms to infer the nature of the solution for the particular case of diatomite.

2.2 Advective-Reactive Transport Modeling

The one-dimensional mass balance equation for silica transport through a porous medium considering only aqueous phase flow through the pore space can be written as,

$$\frac{\partial C}{\partial t}+\frac{u}{\phi}\frac{\partial C}{\partial x}=r \tag{2.1}$$

where ϕ is porosity, r is rate of reaction, u is darcy velocity and C is silica concentration. In this equation we have neglected mass transfer that could occur due to dispersion and/or diffusion. Solving Eq. 2.1 analytically requires a mathematical expression for the rate of reaction in terms of silica concentration C.

Like any other mineral oxide, silica, which is SiO_2, dissolves by hydrolysis of active sites (Saneie and Yortsos, 1985) on the surface of the solid silica containing rock. This process of hydrolysis causes formation of an intermediate complex, which exists in equilibrium with the aqueous solution. This process is a first-order reaction with some particular rate constant only for pH in the vicinity of 8. It has already been seen in experiments by others (Stosur and David, 1971) that in the case of hot water injection in diatomite core plugs, the pH of the water solution coming out of the core plugs is around 8 due the buffering process that takes place within the cores. Thus, for our modeling studies we assume that the silica dissolution/ precipitation reaction is a first-order reaction as given below,

$$r = -k\left(C - C^{\circ}\right) \tag{2.2}$$

where C^o is the equilibrium concentration of silica in the aqueous phase at the reaction temperature of T and k is the reaction rate constant. The equilibrium concentration of silica in aqueous phase at a given temperature between $0^o C$ and $250^o C$ is given by Fournier and Rowe (1977),

$$\log C^o = \left(\frac{-731}{T} + 4.52\right) \tag{2.3}$$

where T is in degrees K. The constant appearing in Eq. 2.2 is the rate constant k. It also depends on the temperature of reaction. This temperature dependence of k and C^o, couples Eq. 2.1 to temperature.

We consider that in a conventional thermal simulator the temperature equation is solved independently, and thus the temperature profile is already known approximately before the kinetics calculations are done. So we model the mass balance equation at a given known temperature. We solve (Appendix I) the silica mass balance equation for the following set of parameters,

(i) The whole grid block is at a single temperature T, initial concentration C_I.

(ii) The hot water entering the grid blocks is at a silica concentration C_J.

(iii) The equilibrium silica concentration corresponding to temperature T is C^o.

The solution is then,

$$C(x.t)=C^o+\left(C_J-C^o o\right)\exp\left(\frac{-\phi xk}{u}\right) \qquad ;\, t\geq\frac{\phi x}{u}$$

$$C(x,t)=C^o+\left(C_I-C^o\right)\exp(-kt) \qquad ;t\leq\frac{\phi x}{u} \tag{2.4}$$

The nature of this solution can be summarized as follows:

a) The concentration travels as a front. The front location at any time 't' is given by,

$$x=\frac{ut}{\phi} \tag{2.5}$$

b) Behind the front, the concentration is a function of position only and does not depend on the time elapsed.

c) Ahead of the front, the concentration is dependent only on time elapsed and is independent of the position.

The solution given as Eq. 2.4 is valid for any silica-containing medium given that the conditions for first order reaction rates and uniform T exist within the medium.

2.3 Nature of Solution for Diatomite

To explore the nature of the solution as given by Eq 2.4 for diatomite we need reaction rate models that can predict the reaction rate constant k in terms of temperature T of the system. In this study, we consider two such models and investigate the nature of the solution for both of these models. The models we consider are that proposed by Koh *et al.* (1996) on basis of their experiments and the model proposed by Rimstidt and Barnes (1980) assuming that the dissolution is a surface reaction.

Reaction model of Koh et al: This model is based on experiments carried out on diatomite core plugs, and the reaction rate constant expression is based on results from the experiment. It is valid for temperature ranges from $49^\circ C$ to $177^\circ C$. The rate constant expression according to this model is given by,

$$m = 1.9 \times 10^{6} \exp\left(\frac{1192}{T}\right) \text{ sec}^{-1} \tag{2.6}$$

where the temperature T is in degrees K.

Reaction model of Rimstidt & Barnes: In their model, they consider that the reaction is a surface reaction and the rate constant k can be linked to surface rate constant k^{-} by the expression

$$k = k^{-}\left(\frac{A}{M}\right) \tag{2.7}$$

where *A*/*M* is the ratio of surface area to mass of water available for deposition. The surface reaction rate constant is related to temperature by,

$$\log k^{-} = -0.707 - \frac{2598}{T} \tag{2.8}$$

where T is measured in degrees K. The ratio *A*/*M* is found in terms of porosity and specific surface area S_v of the porous medium using,

$$\frac{A}{M} = \frac{(1-\phi)S_v}{\phi\rho_l} \tag{2.9}$$

Once we find the reaction rate constant k either by Eq. 2.6 or by Eqs. 2.7 - 2.9, we construct the concentration profiles of silica at different times. These concentration profiles are constructed using the following information,

(i) The darcy velocity of the fluid within the diatomite reservoirs (Bruton, 1996) is 0.3 m/day.

(ii) The specific surface area of diatomite (Bruton, 1996), S_v, is 20 m^2/gm

(iii) The bulk density of diatomite (Stosur and David, 1971) is 0.88-1.3 gm/cm^3 depending on the porosity.

(iv) The length scale L, over which these profiles are constructed is 35 meters which is typically the injector -producer distance in diatomite fields and corresponds to an approximate breakthrough time of 57.4 days for the injected phase.

Using these parameters and the analytical solution, we plot the ratio of $C(x,t)/C^o$ for different possible conditions. The distance over which $C(x,t)/C^o$ becomes unity indicates how quickly the system attains local chemical equilibrium. To study precipitating cases, we consider that the injected aqueous phase has a silica concentration corresponding to $350^o C$ and set the initial system temperature to a lower value and maintain it at a lower temperature during the entire injection process. To study dissolution cases, we set the injected aqueous phase silica concentration to a value corresponding to 0 $^o C$ and assume that the system is at a higher temperature and maintain the higher temperature.

The parameters used for calculating the concentration profiles at different times during the injection process for both dissolution and deposition cases are listed in Table 2.1. Figure 2.1 is such a plot of $C(x,t)/C^o$ versus non-dimensional distance, $x_D = x/L$, for different times considering the reaction mechanism of Koh *et al.* (1996) for deposition cases. The results of this plot show that $C(x,t)/C^o$ attains a value equal to unity within $x_D = 0.04$, *i.e*, one and a half meters, of the injection point even for the early elapsed time of 1 day. The same type of graph is plotted for similar parameters but evaluating k from Rimstidt and Barnes' mechanism in Fig. 2.2. In this case, we see a similar trend. In Figs. 2.3 and 2.4 similar calculations are again made for both reaction mechanisms for the case of silica dissolution. The trend shown by these figures in respect to attainment of local chemical equilibrium is the same as that seen in the case of precipitation. Equilibrium is reached very close to the injection point.

To find the effect of initial system temperature on the analytical solution, we plot similar graphs of $C(x,t)/C^o$ versus non-dimensional distance x_D for different temperatures ranging from $50^o C$ to $200^o C$ for dissolution and precipitation cases for both reaction mechanisms. Various other parameters that are fixed in these calculations are listed in Table 2.2. The results from these calculations are seen in Figs. 2.5 through

Table 2.1: Parameters Used in Calculations Presented in Figs.2.1 Through 2.4

Case	Deposition	Dissolution
Velocity	1.0 ft/day	1.0 ft/day
Porosity	0.5	0.5
Injection temperature	350°C	0°C
Bulk density of rock	0.88	0.88
Initial temperature	60°C	60°C
System temperature	60°C	60°C

Table 2.2: Parameters Used in Calculations Presented in Figs.2.5 Through 2.8

Case	Deposition	Dissolution
Velocity	1.0 ft/day	1.0 ft/day
Porosity	0.5	0.5
Injection temperature	350°C	0°C
Bulk density of rock	0.88	0.88
Initial temperature	50°C-200°C	50°C-200°C
System temperature	50°C-200°C	50°C-200°C

Table 2.3: Parameters Used in Calculations Presented in Figs.2.9 Through 2.12

Case	Deposition	Dissolution
Velocity	1.0 ft/day	1.0 ft/day
Porosity	0.3-0.65	0.3-0.65
Injection temperature	350°C	0°C
Bulk density of rock	0.88	0.88
Initial temperature	60°C	60°C
System temperature	60°C	60°C

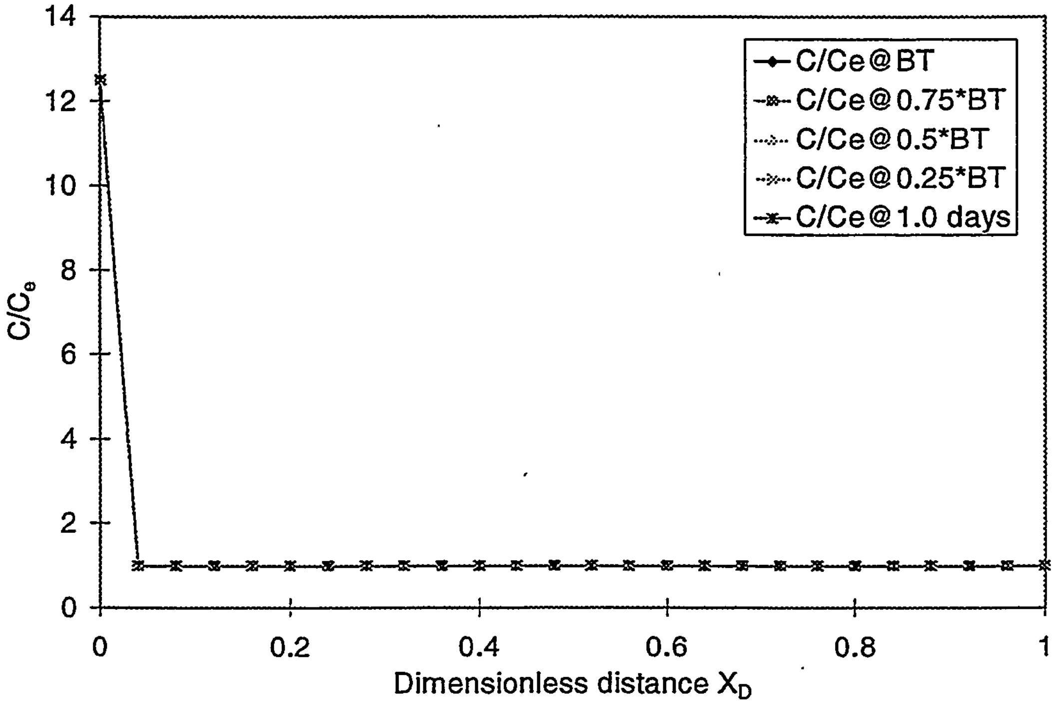

Figure 2.1: Concentration profiles at different times assuming *Koh et al* (1996) mechanism during deposition

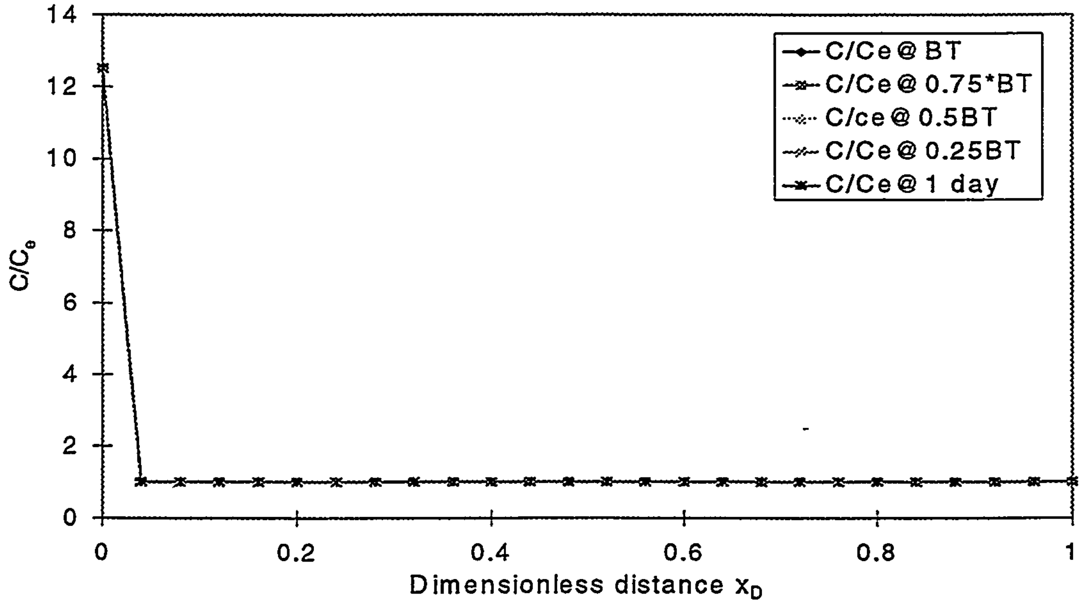

Figure 2.2. Concentration profiles at different times assuming Rimstidt and Barnes (1980) mechanism during deposition.

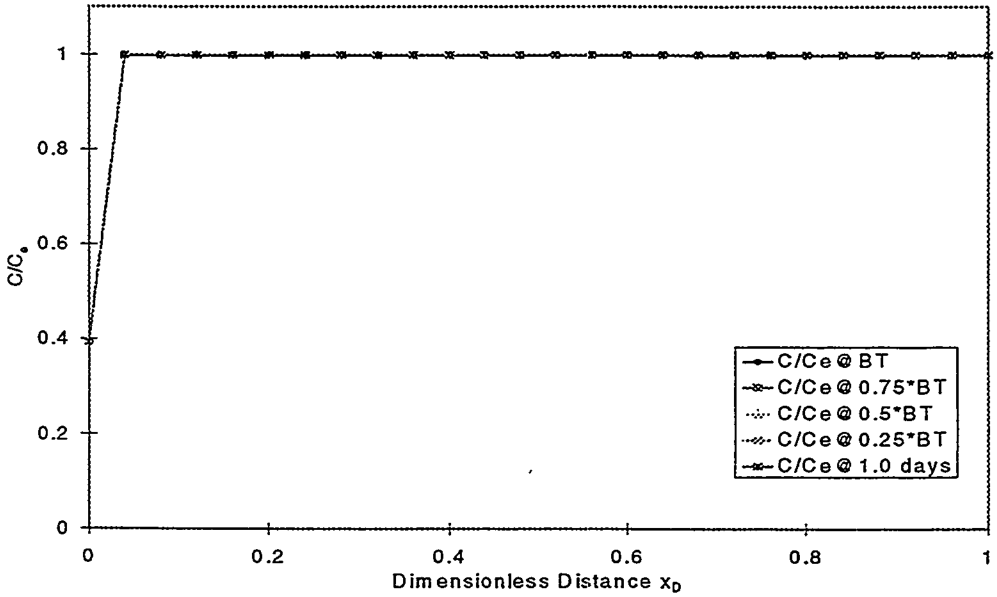

Figure 2.3. Concentration profiles at different times assuming Koh *et al.* (1996) mechanism during dissolution.

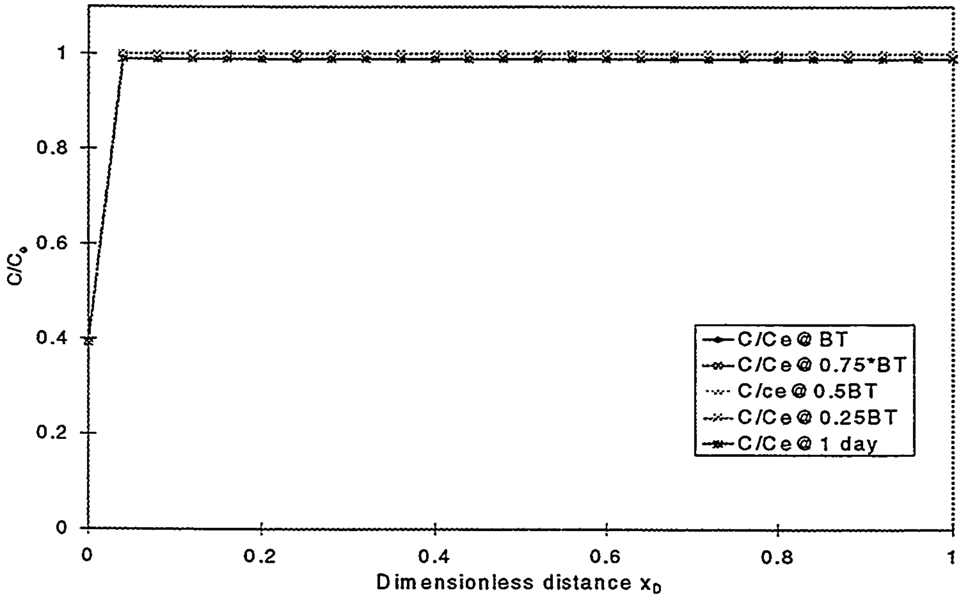

Figure 2.4. Concentration profiles at different times assuming Rimstidt and Barnes (1980) mechanism during dissolution.

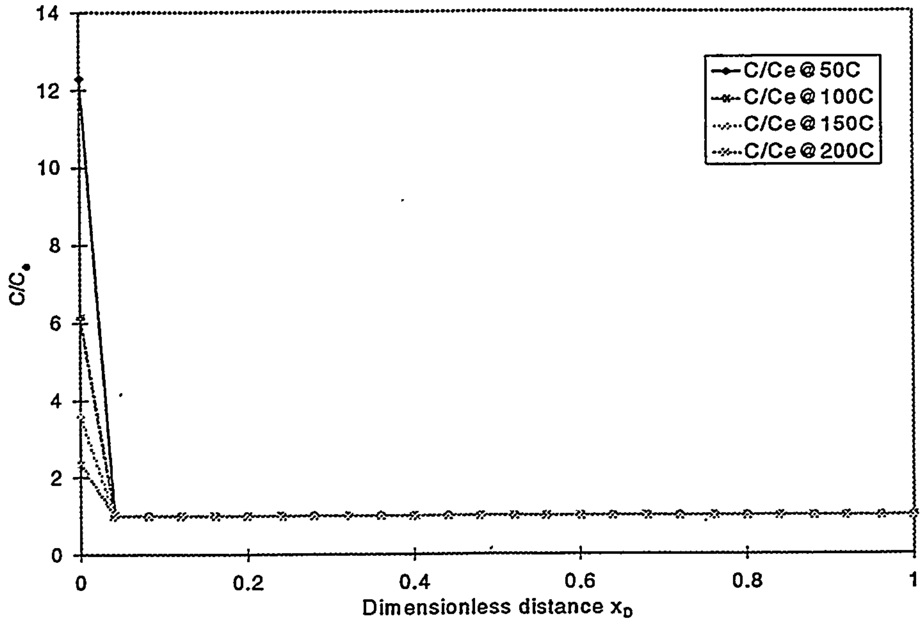

Figure 2.5. Concentration profiles at different temperatures assuming Koh *et al.* (1996) mechanism during deposition.

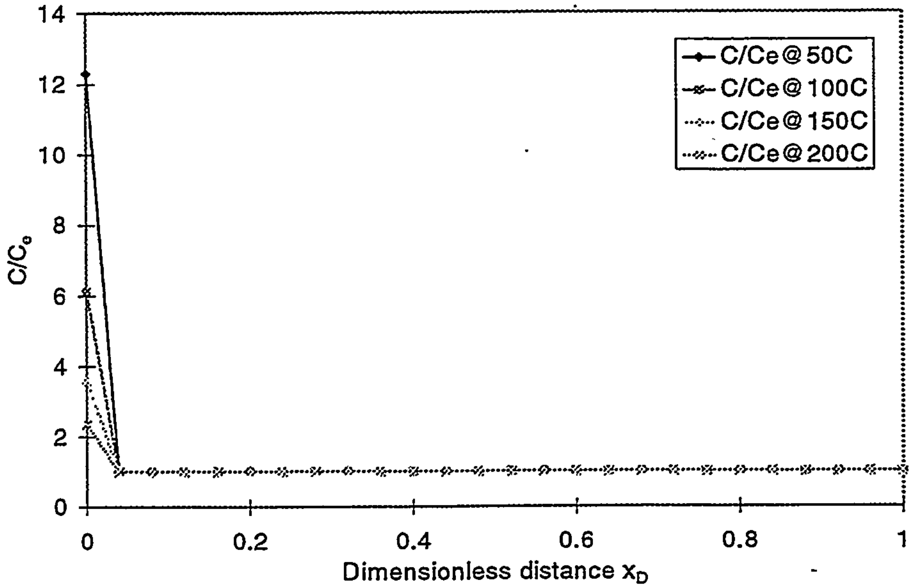

Figure 2.6. Concentration profiles at different temperatures assuming Rimstidt and Barnes (1980) mechanism during deposition.

2.8. The trends of these graphs also show that for all the temperatures local chemical equilibrium is attained very near the injection point.

The other factor that could vary considerably in diatomite and particularly during the diagenetic process is porosity. To assess the effect of porosity on the concentration profiles in diatomite, we plot $C(x,t)/C^o$ versus distance, *x*, for various porosity values ranging from 30 % to 65 %. The other parameters are fixed as per Table 2.3. The plots generated are given in Figs. 2.9 through 2.12. The trends of these graphs also show that for all porosity values local chemical equilibrium is attained very near the injection point in case of diatomite.

Based on the trends in Figs. 2.1 through 2.12 and known mechanisms and kinetics, we can generalize, that during condensate flow in diatomite reservoirs, the silica concentration in water is equal to the equilibrium concentration corresponding to the temperature at that location. This remains true over the whole length of the reservoir except for areas near the injection point. Thus, if we are able to predict the temperature profile within the reservoir, we can easily find the silica concentration in the aqueous phase by assuming local chemical equilibrium.

2.4 Conclusions

The advective-reactive transport of silica during hot condensate flow through distomite is advection dominated. The rate of reaction is very fast compared to the rate of advection.

If we consider the reservoir to be made up of different grid blocks, each having some temperature within it, the silica concentration in the grid block is the equilibrium solubility of silica in water at the grid-block temperature. This is called local chemical equilibrium. This will be true for all the blocks except for injectors and producer, which will have very high advection rates assuming radial flow in and out of wells.

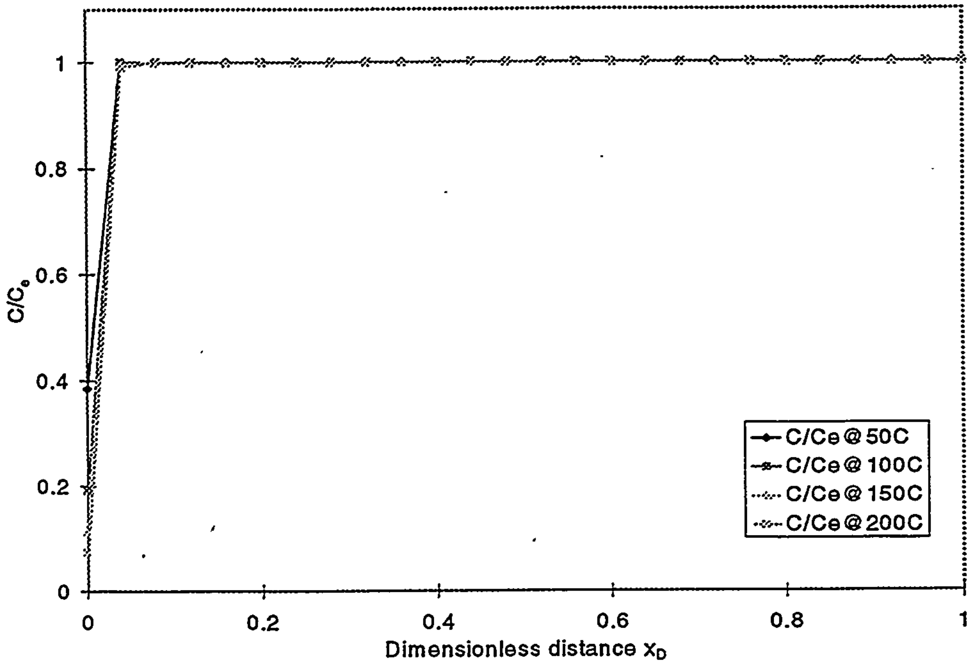

Figure 2.7 Concentration profiles at different temperatures assuming Koh *et al.* (1996) mechanism during dissolution.

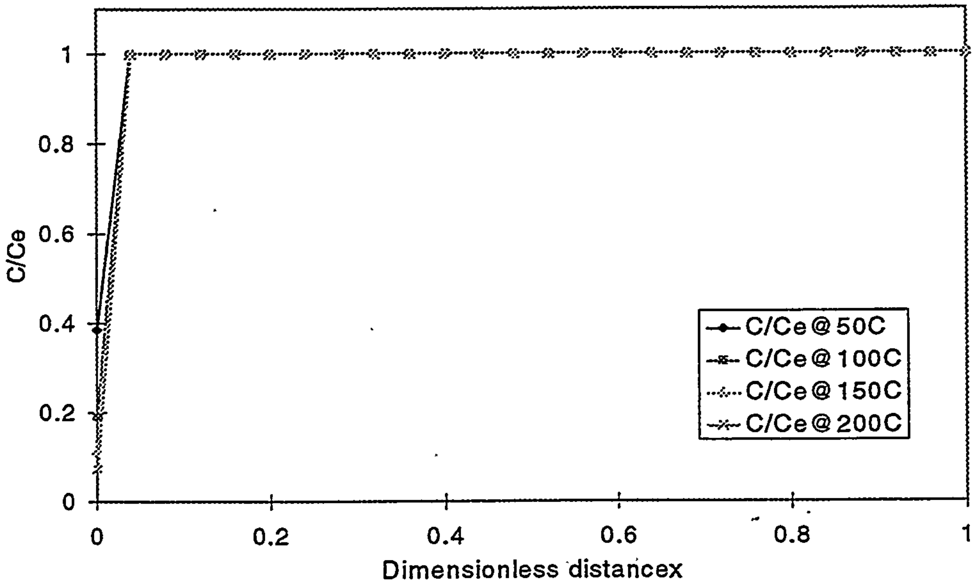

Figure 2.8. Concentration profiles at different temperatures assuming Rimstidt and Barnes (1980) mechanism during dissolution.

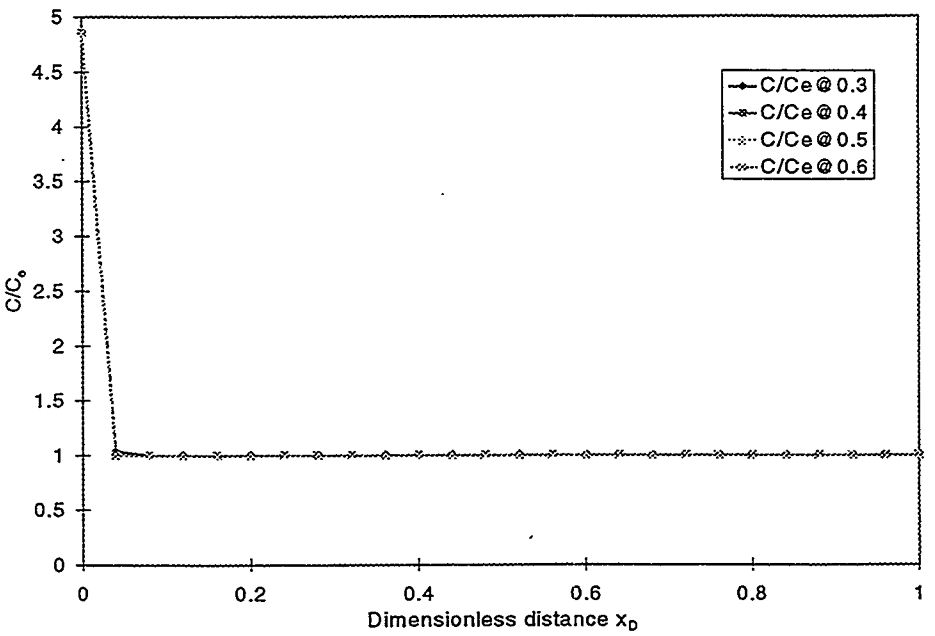

Figure 2.9. Concentration profiles at different porosity assuming Koh *et al.* (1996) mechanism during deposition.

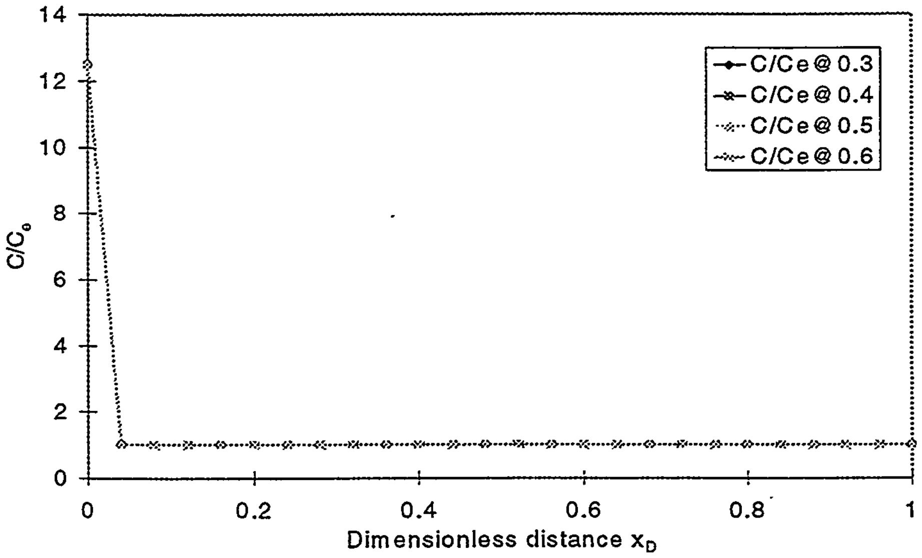

Figure 2.10. Concentration profiles at different porosity assuming Rimstidt and Barnes (1980) mechanism during deposition.

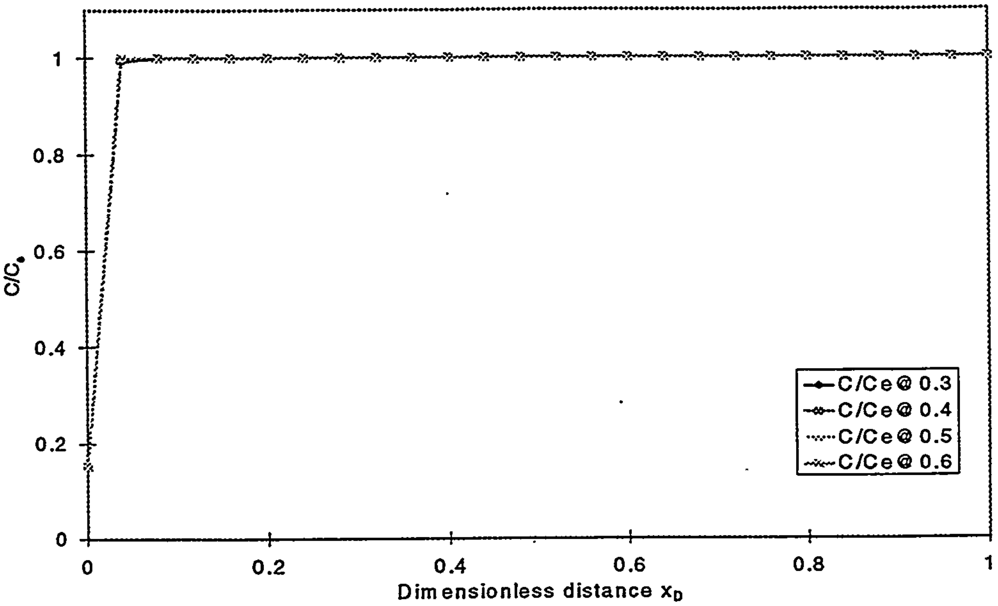

Figure 2.11. Concentration profiles at different porosity assuming *Koh et al.* (1996) mechanism during dissolution.

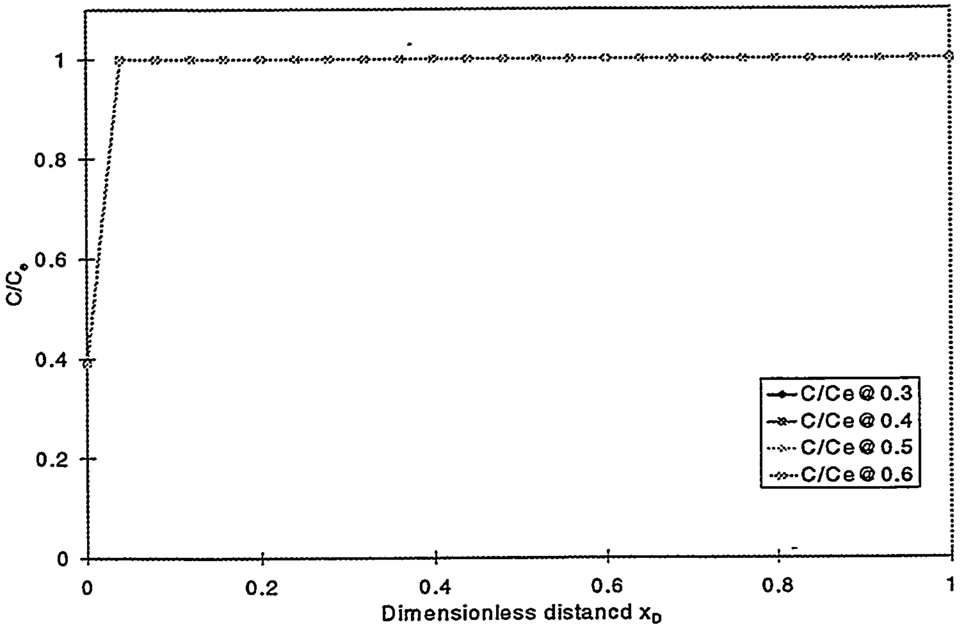

Figure 2.12. Concentration profiles at different porosity assuming Rimstidt and Barnes (1980) mechanism during dissolution

3. Pore-Level Characterization

3.1 Introduction

The extent, to which a quantity of deposited or dissolved silica will alter the permeability of a porous medium, depends on the pore-level structure of the medium. Thus, to quantify correctly the impact of dissolution or deposition on the permeability of diatomite, we need the knowledge of pore-scale properties of this rock. We need the average pore-body and pore-throat sizes, their distributions, and connectivity. We will also need to know properties such as permeability and porosity of this rock before any of the dissolution and deposition processes start.

Diatomite is characterized by a very low permeability of the order of 0.1 to 10 mD. Curiously, this low permeability occurs with a very high porosity ranging from 35 to 65 %. This permeability/porosity profile indicates that this rock is different from sandstone or chalk in pore-level characteristics. In this study, we explore the peculiar characteristics of diatomite with a variety of tools including X-ray computed tomography (CT scanning), mercury intrusion porosimetery and scanning electron microscopy. The study of this rock is done at both the pore level and the core level.

At the pore level, we characterize diatomite by studying its features under a scanning electron microscope (SEM). We try to identify the pore-level features that explain its peculiar properties. We identify regions of the rock that could be called pore throats and pore bodies. At the core level, we characterize this rock using mercury intrusion porosimetery. We measure a capillary pressure curve for this rock and try to infer pore-level characteristics from this data. To complement the core-level work, we also study the rock via X-ray computed tomography (CT). We analyze the CT images and obtain the distribution of porosity. In the end, we compare the results obtained for the pore-level properties by direct investigation via SEM and the indirect investigation by observing core-level behavior.

Diatomite samples were obtained from the Grefco Quarry in Lompoc, CA. They had no initial oil or water saturation. Studies of a similar nature have been performed on diatomite by other investigators. Stosur and David (1971) studied samples from the Lost Hills Field (Kern Co., CA). Their finding were based on well-log measurements, core-level studies and SEM pictures. They concluded that the diatomite has a high initial water saturation of 0.58 and a low rock matrix density of 2.4 gm/cc on the average. They found an in-situ porosity averaging around 36.7 %. Their SEM analysis showed that most of the silica in diatomite was amorphous silica. Schwartz (1988) also has studied the diatomaceous formations of the South Belridge oil field and their depositional origin. He studied the deposition environment for these formations based on well-log studies and SEM images. He concludes that the high porosity, low permeability and high oil saturation in these formations is due to relatively clean diatomite. In this study, we have tried to connect SEM images and CT images to the pore-size distributions obtained with mercury intrusion.

3.2 Petrophysical Evaluation

The largest scale at which we studied diatomite was a block roughly 30 cm by 30 cm by 12 cm. The block was placed in a CT scanner and scanned at different locations. These were dry scans of the block, i.e., the CT images were taken on a dry sample. The results of these dry scans are shown in Fig. 3.1. The slices are roughly 2 cm apart. These scans show that for most purposes the rock is relatively homogeneous at this scale. The white portion in the lower left-hand corner of the images results because a corner of the block is missing. The lighter colored streaks are evidence of bedding planes, although the CT number contrast is not large.

Next the rock was cut and shaped into cylindrical cores of 2.5 cm diameter and 9.5 cm length and dry CT scans of these cores were taken. Then the cores were saturated with water, and again CT images were taken. The difference between the dry and wet images of these cores was used to construct porosity maps. Figure 3.2 shows porosity maps of two such cores. The gray shading of Fig. 3.2 is the porosity scale that has a notably narrow range. The porosity distribution of these cores corresponding to the porosity maps of Fig. 3.2 are shown in Fig. 3.3. All these results indicate that the average porosity of all the samples taken out of the block was around 65-67%. Also, the porosity

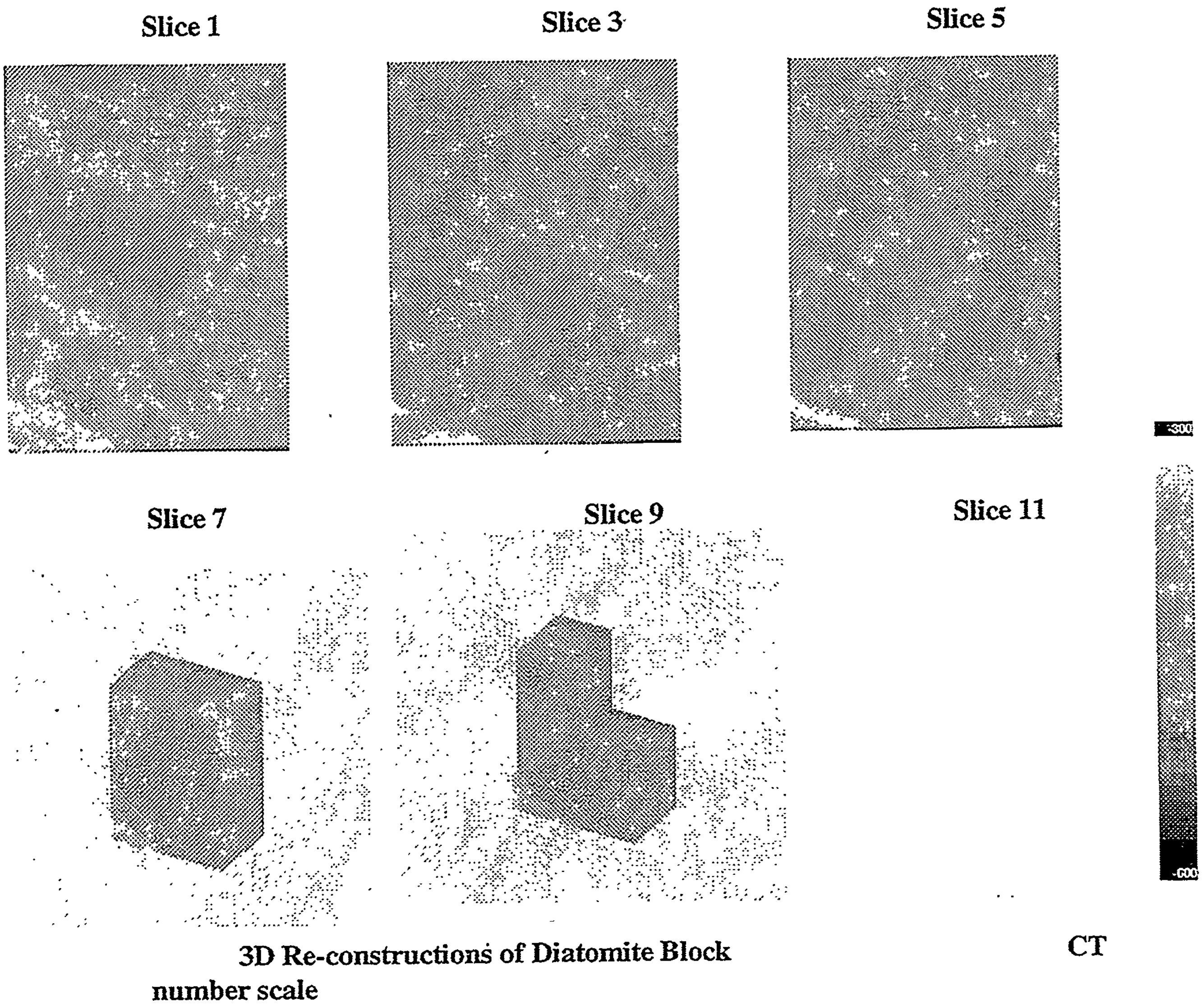

Figure 3.1: CT images of 30 cm by 30 cm by 12 cm block of diatomite.

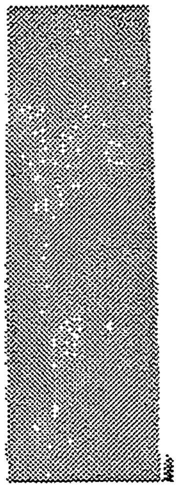

(a) Core 1 Image

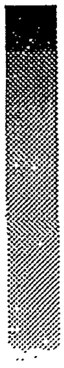

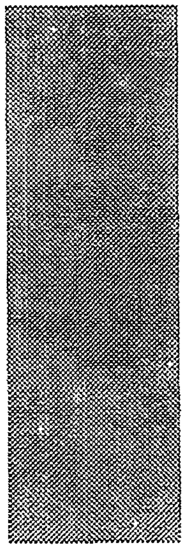

(b) Core 2 Image

Figure 3.2: Porosity maps of diatomite cores 2.5 cm in diameter and 9 cm long

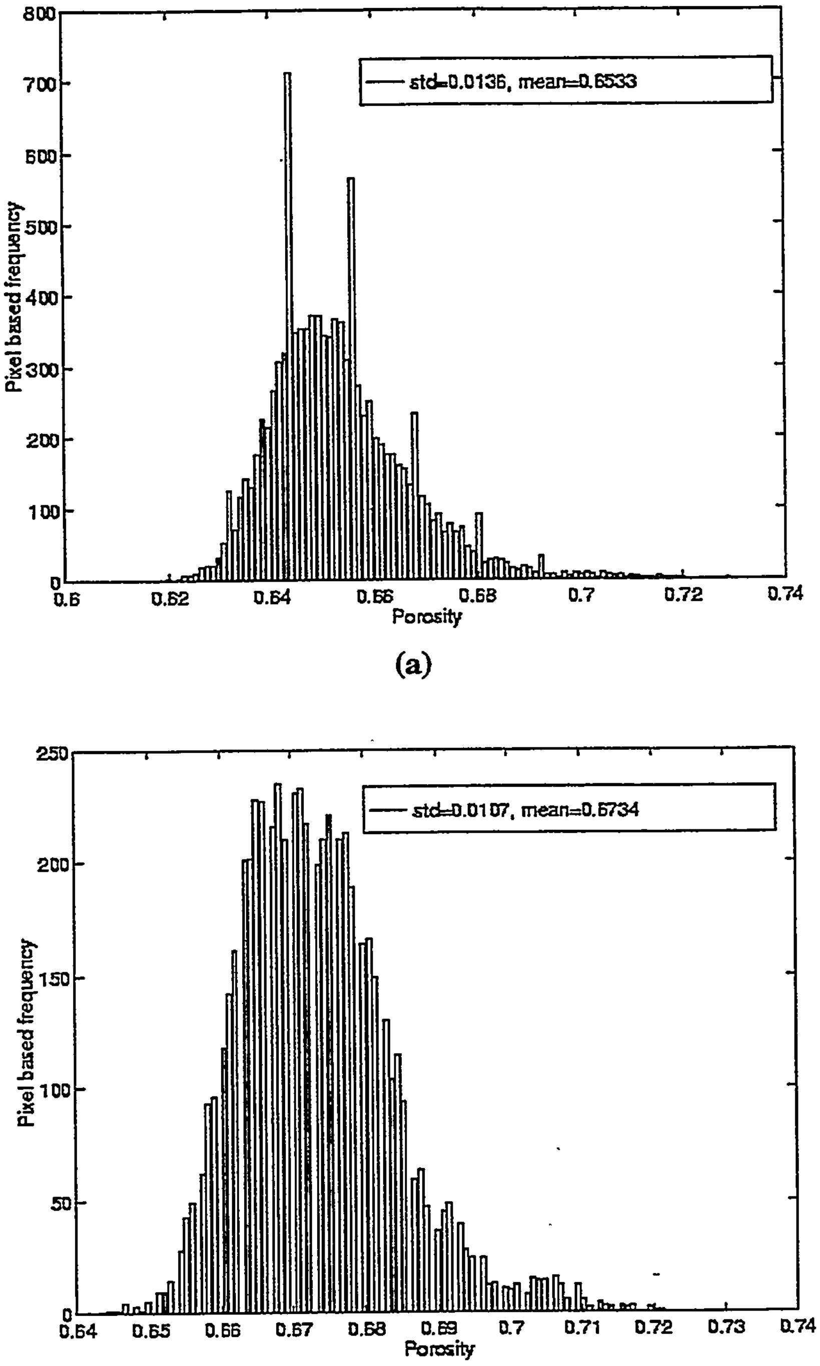

(a)

(b)

Figure 3.3: Porosity distribution of diatomite cores obtained from maps of Fig 3.2.

distributions as shown in Fig 3.3 demonstrate that there is not much variation in porosity and it lies in the range of 61-68 %. The standard deviation for core 1 is 0.0136 and for core 2 is 0.0107. The narrow distributions of Fig. 3.3 confirm that we can consider diatomite as relatively homogenous at this scale.

3.3 Core-Level Studies

We performed mercury injection porosimetery to measure pore-throat and pore-body size distributions, as well as porosity of the rock sample. For this purpose, we used a Ruska porometer model number 1051-801. The experiments were performed using the guidelines listed in the operating manual of the porometer for determining the porosity of a rock sample (RUSKA). We performed two runs. The volume of the rock sample in the first run was 6.975 cm^3 and in the second run it was 5.29 cm^3. The apparatus was vacuum evacuated before the start of each run. The mercury was injected into the sample at different pressures and the pressure versus volume of mercury injected into the sample recorded (Appendix III). The maximum injection pressure possible with the porometer was 850 psig. After reaching the maximum pressure limit, the pressure was gradually decreased and the volume of mercury inside the sample was noted. The experiments were performed at an average temperature of $22^{\circ}C$. Then it was assumed that 850 psig was a pressure large enough to completely invade all accessible pore space of the rock. Based on this assumption, the non-wetting phase saturation inside the sample was determined using,

$$S_{nw} = \frac{V_{corr}}{V_{corr,850}} \tag{3.1}$$

where S_{nw} is the non-wetting phase saturation and V_{corr} and $V_{corr,850}$ represent the corrected mercury volume in the rock at current pressure and 850 psig, respectively. Based on Eq. 3.1 and the pressure versus volume data, the mercury-vacuum capillary pressure curve for diatomite is shown in Fig. 3.4. For these two samples, the porosity determined is reported in Table 3.1. These values are slightly lower than the averages reported in Fig. 3.3.

Table 3.1: Porosity Measurements by Mercury Intrusion

SAMPLE VOLUME	POROSITY
6.975 cm^3	0.61147
5.29 cm^3	0.619093

The last core-level experiments performed on diatomite determined the absolute permeability. Two samples from the same outcrop were used. The air permeability of these samples was measured using a Ruska permeameter model 1101-801 at three different gas flow rates. The air permeability versus flow rate data (Appendix IV) was then used to find the absolute permeability of the samples after correcting for the Klinkenberg effect. The average permeability of the samples was 8.5 mD. The measured permeability data is listed in Table 3.2.

Table 3.2: Permeability Measurements by Gas Permeameter

SAMPLE LENGTH	SAMPLE DIAMETER	PERMEABILITY
2.54 cm	2.54 cm	8.4753 mD
2.6924 cm	2.5781 cm	6.4255 mD
1.7272 cm	2.54 cm	8.5538 mD
2.159 cm	2.54 cm	8.7965 mD

The permeability measurements and the air-water capillary pressure data were used to find the Leverett-J function, $J(S_w)$ for diatomite using the fact that,

$$J(S_w)Cos\theta = \frac{p_c\sqrt{k/\phi}}{\sigma} \tag{3.2}$$

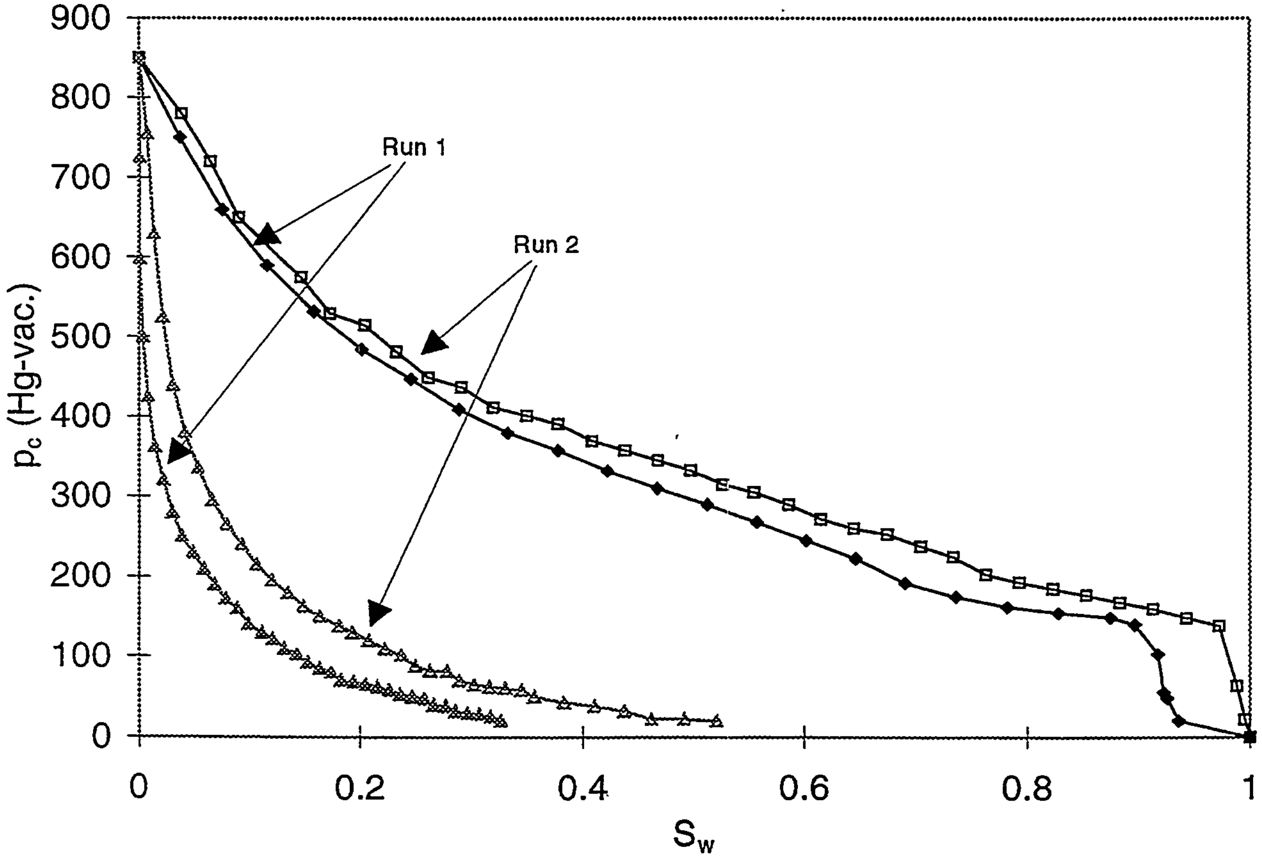

Figure 3.4: Mercury-vacuum capillary pressure data.

where, θ is the contact angle between the rock and the fluid being injected, k is the absolute permeability of the porous medium, ϕ is the porosity, and σ is the surface tension of the fluid being injected. The resulting curve is shown in Fig. 3.5.

3.4 Pore-level Studies

The pore-level studies were conducted on three samples from the same rock block. The samples were sputtered with palladium-gold (Pd-Au) coating to make the surfaces conducting. The thickness of the coating was quite thin such that all the surface features of these samples are retained. To explain the reason for low permeability of diatomite, we first obtained an image of diatomite at the magnification that is comparable to the magnification where pore-level features in sandstone are seen. Figures 3.6 and 3.7 show such a comparison. Figure 3.6 is the SEM of a sandstone sample at a magnification level of 100X. We are able to see features that could be characterized as flow paths typically of the size of 200 µm. Sand grains are also evident and are about 200 µm in size. At the same magnification level in diatomite, i.e. Fig. 3.7, there are no visible surface features that could be interpreted as flow paths. Note that the granular size of diatomite is much smaller than that of sandstone.

To identify features that could be associated with the flow properties of diatomite, a magnification level of 1400X was used as shown in Fig. 3.8. Surface features are evident at this magnification. Regions of the rock that could be acting as pore bodies, range in size from 50 µm to 10 µm. The features that could be acting as pore throats in Fig. 3.8 have size in the range of 5 µm. These features are fairly regular, perhaps owing to the organic origin of the rock.

Another observation in this SEM study is that for most part there are not many complete intact diatoms. One such complete diatom is shown in Fig. 3.9 at a magnification level of 3400X. The streaks in the upper left-hand portion of the SEM photograph arise due to low conductivity of the surface. The diatom has a diameter of

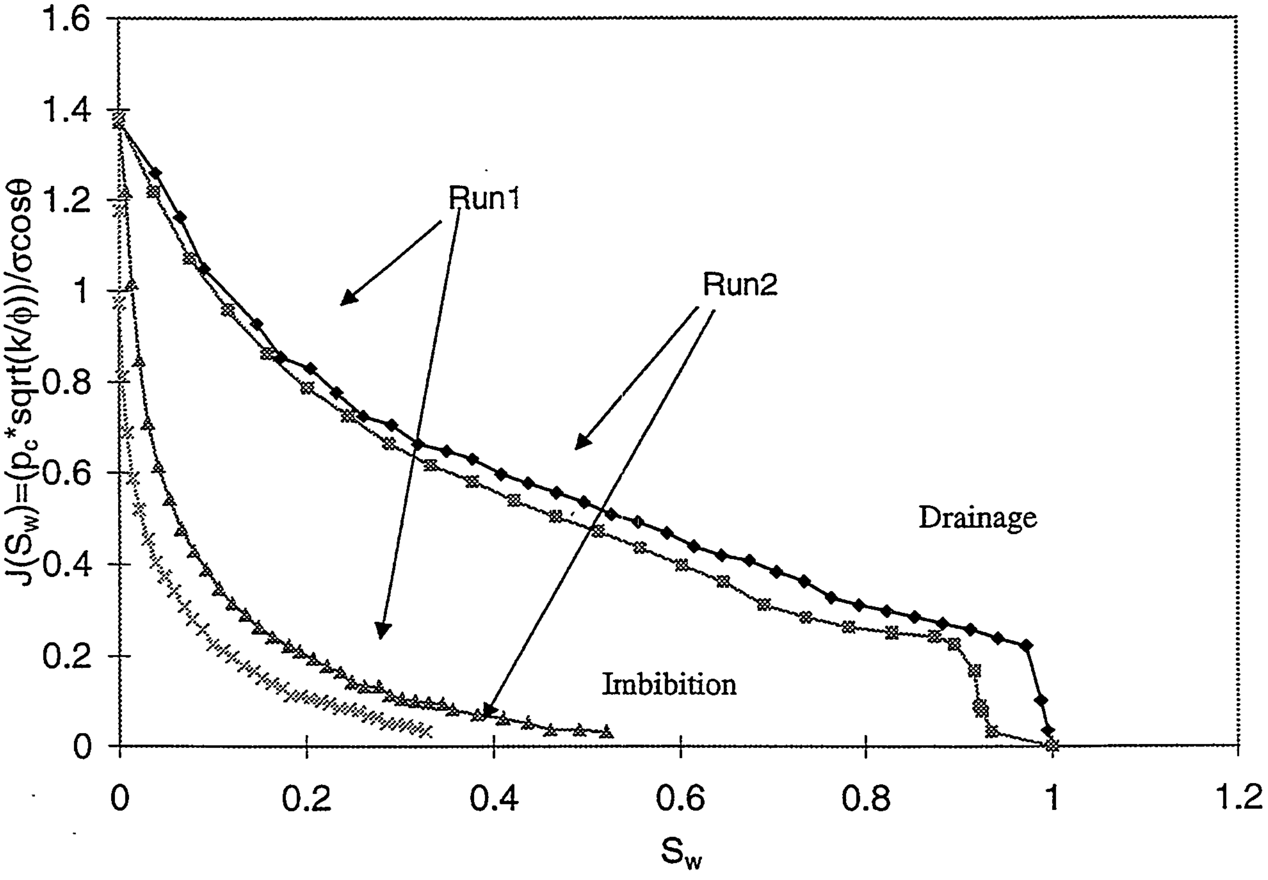

Figure 3.5: Leverett-J function data for diatomite.

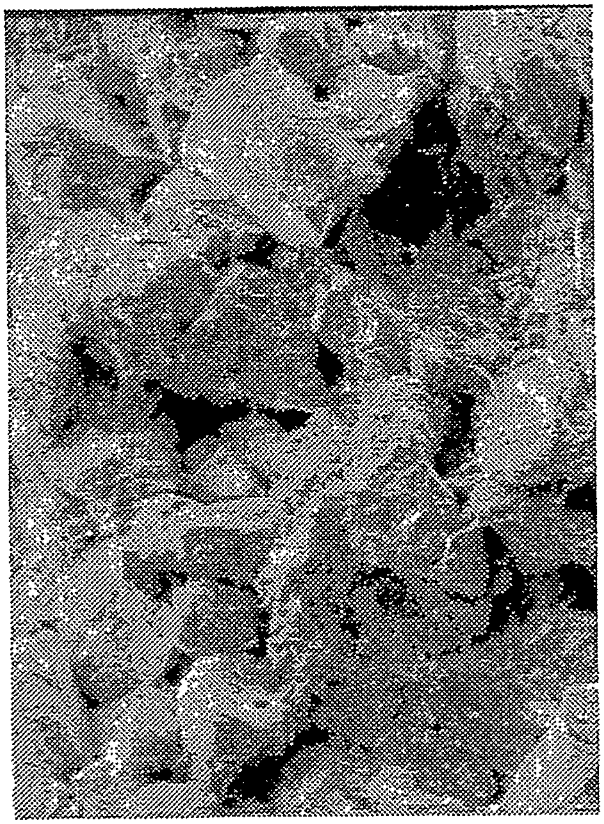

Figure 3.6: SEM image of sandstone at a magnification level of 100X.

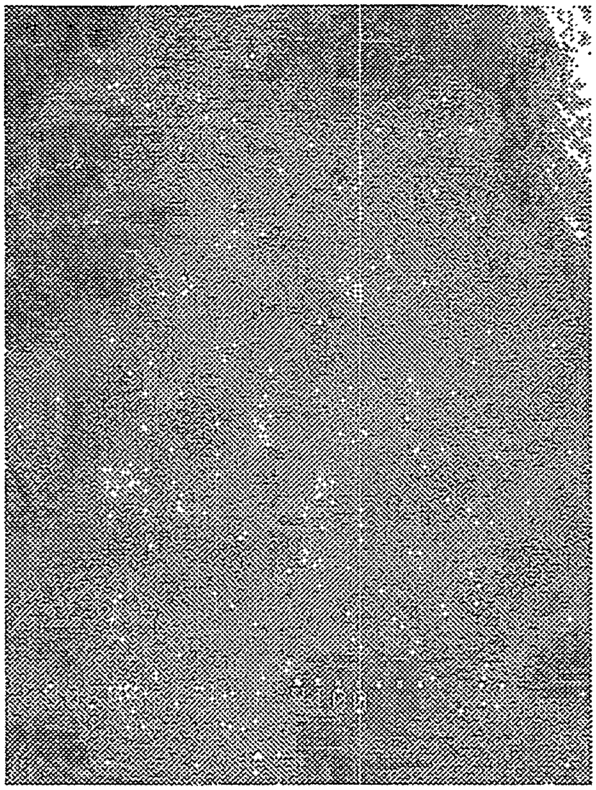

Figure 3.7: SEM image of diatomite at a magnification level of 100X.

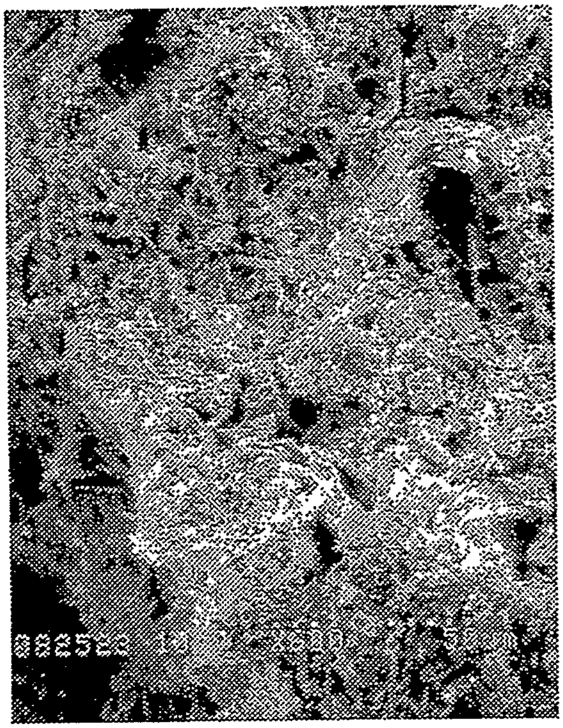

SCALE:25.2 μm

Figure 3.8: SEM image of diatomite at 1400X.

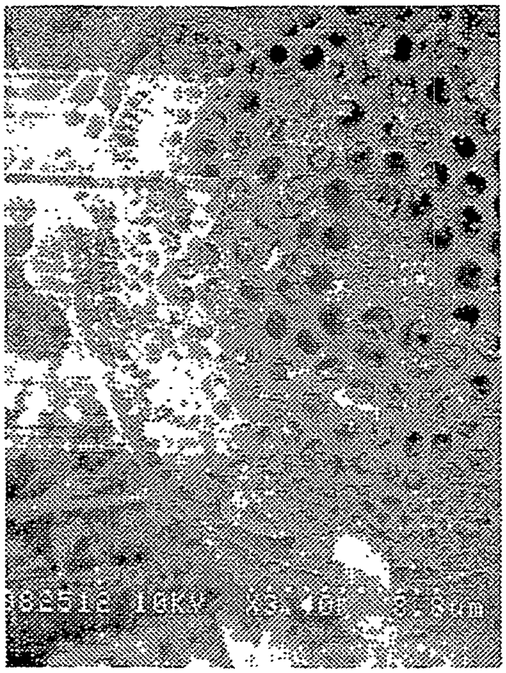

SCALE:8.8 µm

Figure 3.9: SEM image of a complete diatom at 3400X.

is around 75 µm. Even though we were not able to see many complete diatoms, we do see many features that could be interpreted as broken diatom remains. One such broken diatom is shown in Fig. 3.11 at a magnification of 3000X. The feature seems to be the outer rim of a diatom. Another important fact that we observed under the microscope was that most of the flow paths contain the debris of broken diatomite at most levels of magnification. This is another reason for low permeability of diatomite. In Fig. 3.12 we see that the features possibly identified as throats seen are clogged by the debris of broken diatomite.

The other microscopic structures that we were able to see in the SEM images were micro-fractures. We identified a micro fracture at a magnification level of 25X in Fig. 3.13. The length of the fracture is around 2.5 mm. The same fracture seen at a magnification of 500X in Fig. 3.14 shows that the width of the fracture is around 20 µm and the depth may be of the same order. The depth of the micro-fracture reveals the highly layered nature of the rock. Also, we see that in spite of this layered structure there is significant porosity within the layers. This could be a reason contributing to the low mechanical strength and high porosity of this rock. The frequency of the micro-fractures encountered was not large.

3.5 Core-Level Findings Versus Pore-Level Investigation

The correlation consists in trying to generate pore-level information from core-level studies.

Generating pore information from mercury intrusion: The mercury intrusion data obtained from experiments was used to generate pore-size distributions using the Ritter-Drake technique. It is true that this type of approach does not take into account the connectivity of the rock and is an over simplification of the porous medium, but it still has the capacity to give us an idea about the size distribution if used properly. We assume the porous medium can be characterized as a combination of pore bodies and pore throats as shown that the pores in Fig. 3.15. The capillary pressure for any position of

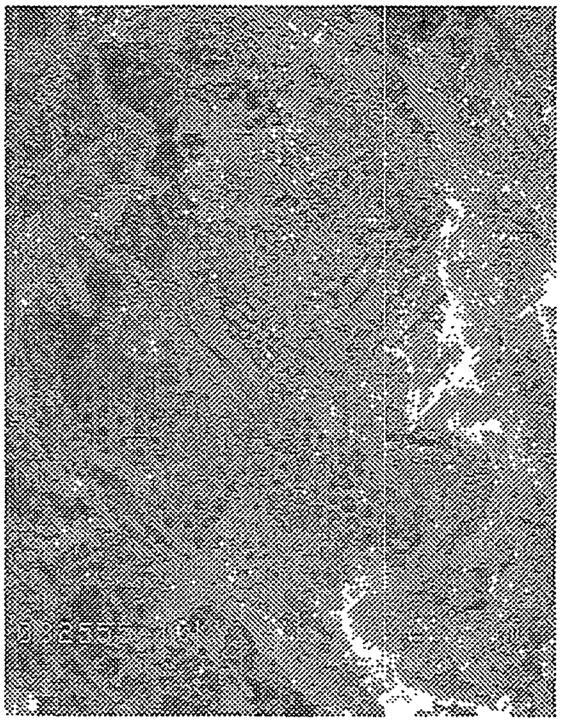

SCALE:25.2 μm

Figure 3.10: SEM Image of a complete diatom at 1190X.

Figure 3.11: SEM image of a broken diatom at 3000X.

SCALE:15µm

Figure 3.12: SEM image at 2000X, showing debris blocking flow paths.

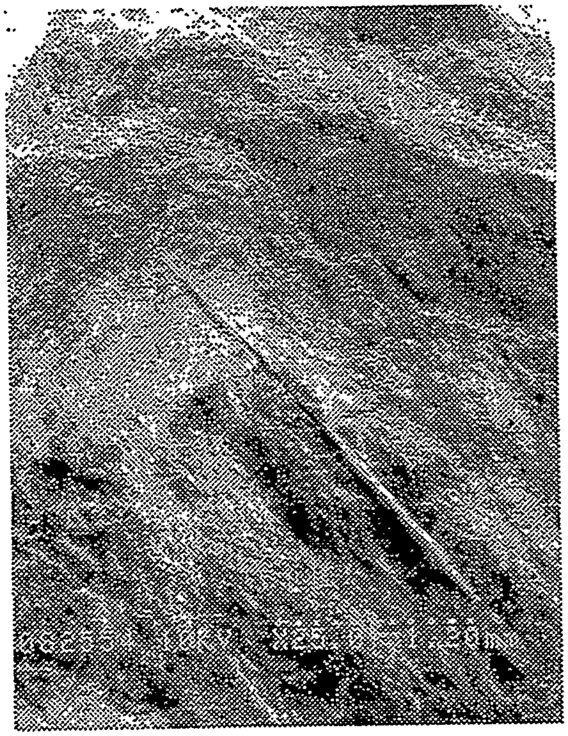
SCALE:1.2mm

Figure 3.13: SEM image of a micro-fracture at 25X.

SCALE:60µm

Figure 3.14: SEM image of the micro-fracture at 500X.

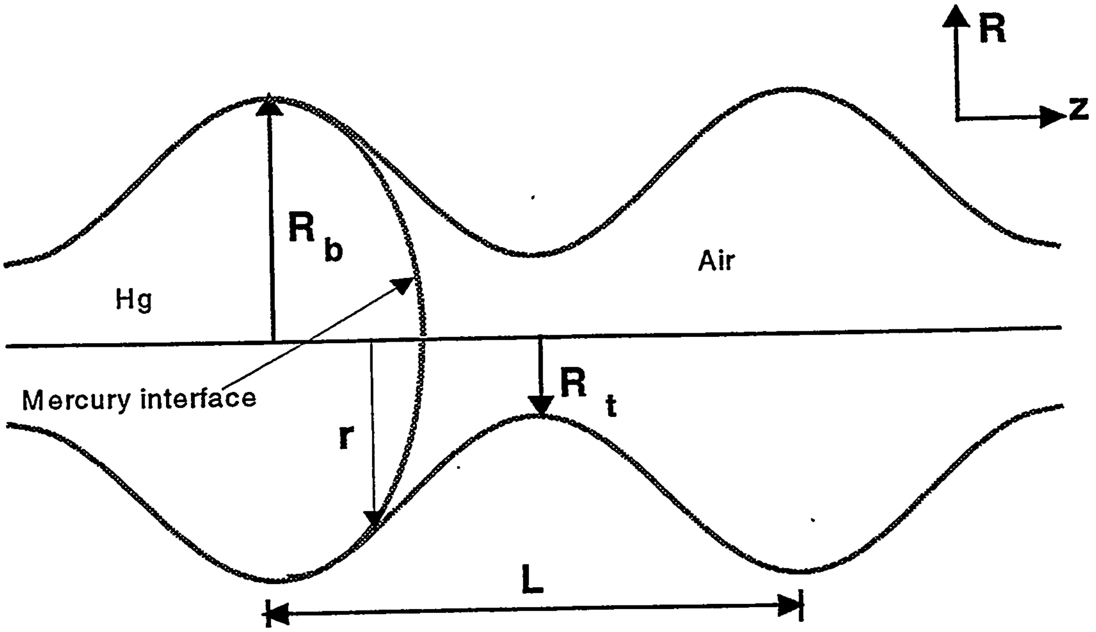

Figure 3.15: Single Pore-model used to interpret mercury intrusion experiments.

non-wetting and wetting phase interface is given by,

$$p_c = p_{nw} - p_w = \frac{2\sigma Cos\ \theta}{R} \tag{3.3}$$

where, p_{nw} and p_w are the pressure in the non-wetting and wetting phase, respectively, and R is the radius at that location. This equation assumes that the radius at a location is roughly the radius of curvature of the interface. Equation 3.3 can be differentiated to yield the following expression,

$$p_c dR + R dp_c = 0 \tag{3.4}$$

Now if we make the assumption that volume of pores with sizes between R and $R + dR$ where V_T is the total volume of the sample and V_{sample} is the volume of mercury injected in the sample at a given capillary pressure. Thus the, term dV_{sample}/dp_c represents the slope of volume injected versus pressure curve. The value of R can be found for a given p_c by using Eq. 3.3. Based on these two equations, the pore-size distribution is found. Mercury is the non-wetting phase and the pressure needed to fill completely the pore of Fig. 3.15 is governed by the size of throat R_t and the process is drainage. The drainage capillary pressure is given by,

$$p_{c,drainage} = p_{nw} - p_w = \frac{2\sigma Cos\theta}{R_t} \tag{3.7}$$

The mercury intrusion data is used to generate the pore-throat size distribution for diatomite as given in Fig. 3.16. On the other hand, when mercury is retracted from the pore in Fig. 3.15, the limiting capillary pressure is determined by the pore-body size R_b and the process is imbibition. The imbibition capillary pressure is given by,

$$p_{c,imbib} = p_{nw} - p_w = \frac{2\sigma Cos\theta}{R_b} \tag{3.8}$$

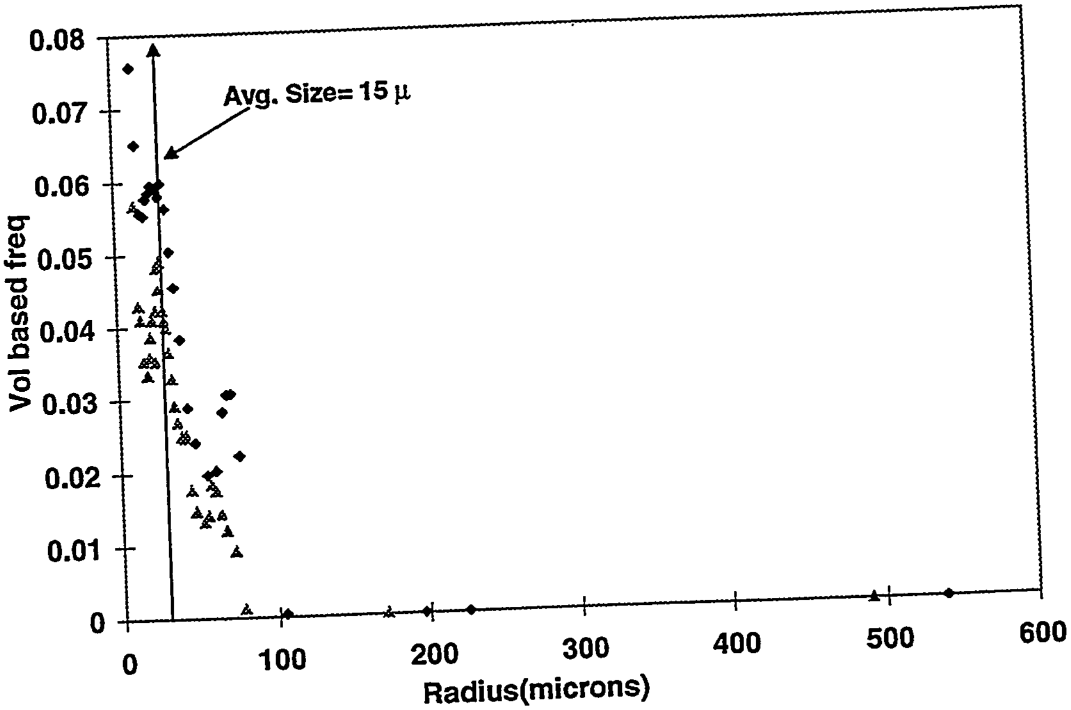

Figure 3.16: Pore-throat size distribution obtained from mercury intrusion data.

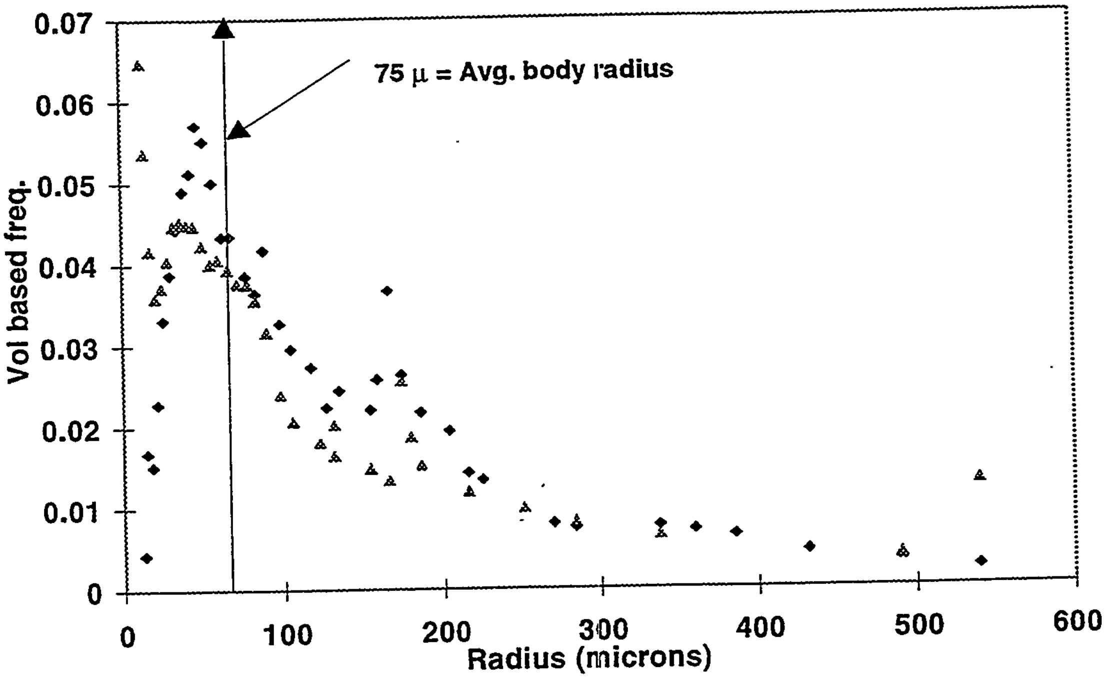

Figure 3.17: Pore-body size distribution obtained from mercury retraction data.

The mercury retraction data is used to generate the body-size distribution as given in Fig. 3.17. The frequency distributions generated by this method are in fact volume-based frequencies. These distributions have a shape similar to a log-normal curve. On the basis of the data, the average body size is around 75 μm and the average throat size is around 15 μm.

3.6 Discussion of Results

The results of the large length scale investigations, *i.e.*, study at the block level indicate that the rock has a fairly homogenous composition at this scale, though certain large-scale features like bedding planes also can be seen. At the next smaller scale, *i.e.*, cylindrical cores of 2.5 cm diameter and 9 cm length, this homogenous nature is still valid. The porosity distributions created at this scale indicated very little spread around the average value of 68 %.

The next smaller level of investigation, *i.e.*, mercury intrusion and retraction into rock samples of volume 6.975 and 5.29 cubic cm, reveals the heterogeneous nature of the rock at the pore-level. The porosity values obtained by this method are nearly 61 %. These values are lower than the average porosity values obtained from cylindrical samples using CT scanning. Inferring the pore-body and pore-throat size distributions from these experiments indicated that both these distributions are uni-modal with a positive skew. The average pore-body and pore-throat sizes obtained from these experiments is 75 μm and 15 μm respectively.

At the smallest scale of investigation, *i.e.*, pore-level, diatomite is fairly heterogeneous. There is evidence of some large scale features like micro-fractures. One such fracture observed was 20 μm in diameter and 2 mm in length. There are very few complete diatoms present in the rock. Diatoms are mostly crushed and present as debris, blocking the flow paths and giving rise to low permeability. The flow paths observed under the SEM indicated that the pore-body size was around 40 μm and the pore-throat size was around 5 μm. The discrepancy between the average pore dimensions obtained by SEM images and porosimetery can be explained by the limitation on maximum injection pressure possible in mercury intrusion experiments. The maximum possible injection pressure in the experiments was 850 psig. This pressure corresponds to intrusion into a pore throat of 12.7 μm. Thus, in our experiment pores smaller than 12.7 μm were not invaded. This also explains the lower values of porosity obtained by mercury porosimetery as compared to CT scanning. This part of the pore space of diatomite (approximately 7%) is left un-invaded and has pores smaller than 12.7 μm. Thus, the average throat and body sizes obtained by mercury intrusion technique are larger.

3.7 Conclusions

From the investigation of diatomite at various length-scales we can conclude that at relatively large scales i.e. up to core-scale, the rock is fairly homogeneous. The rock has a high porosity of the order of 65 % and a low permeability of the order of 8.5 mD. The pore-body and pore-throat size distributions are uni-modal with a positive skew resembling log-normal shapes. The average pore-body size is 40 μm and average pore-throat size is 5 μm.

4. Permeability Alteration Modeling

4.1 Introduction

To quantify changes in permeability and porosity of the porous medium undergoing diagenesis, we develop a network model and incorporate evolving pore shapes. The porous medium is represented by a Bethe lattice of known properties, and percolation theory used to predict the effects of dissolution and deposition on permeability and porosity of the porous medium. We consider only the flow of liquid water. Changes in permeability are correlated with changes in conductivity of the lattice, and the amount of silica deposited is related to available porosity of the lattice at any stage of deposition or dissolution. To model the diagenetic process, various dissolution and deposition patterns are considered. Based on these dissolution and deposition patterns, the network is updated to generate network conductivity and porosity. The networks are anchored to real porous medium through pore-throat and pore-body distributions as well as pore body to throat aspect ratios garnered from outcrop diatomite samples as described in detail in Chapter 3.

The following sections describe our network approximation of porous media, the rationale for our choice, and how pore-throats and bodies are represented. Next, incorporation of silica dissolution and precipitation into first a single-pore model and then the network is discussed. The network is used to generate absolute permeability versus porosity relationships for silica redistribution in diatomite.

4.2 Network Approximation

Porous media can be approximated by lattices as illustrated in Fig. 4.1. Examples shown in the figure are a Bethe lattice (Fig. 4.1A), a hexagonal lattice (Fig. 4.1B), and a 2D-square lattice (Fig. 4.1C). A lattice is a connected network of flow paths between various points in space (2D or 3D). An advantage of the Bethe lattice is that analytical solutions are available for network conductivity.

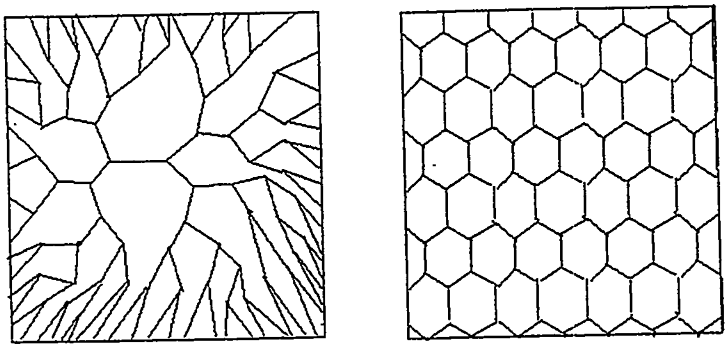

A. Bethe Lattice

B. Hexagonal Lattice

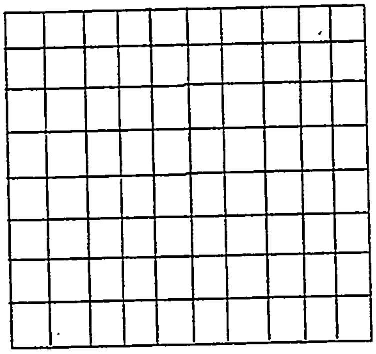

C. Square Lattice

Figure 4.1: Different types of lattices.

Lattices are used to represent porous media, because they can capture at least two important properties of porous media. Firstly, porous media are a collection of pore bodies connected by pore throats. Secondly, porous media have connectivity between pore throats normally given as the coordination number Z. This number is used to quantify the connectivity of the lattice. These two properties of lattices coupled with the fact that flow properties like flow resistance can be randomly associated with the various bodies or throats or both make lattices a good choice for approximating flow in porous media.

We use a Bethe lattice, as illustrated in Fig. 4.1A, to approximate the matrix of diatomite pores. It is an endlessly branching network characterized by the coordination number and distribution of pore sizes. Because the problem of Bethe lattice conductivity has been solved analytically (Stinchcombe, 1974), these networks are especially attractive for our work. Moreover, Bethe lattices have been used to reproduce two and three-phase relative permeabilities in porous media (Heiba *et al.*, 1983; Heiba, *et al.*, 1984; and Heiba *et al.*, 1992). Although networks more complicated than Bethe lattices are certainly possible, our ignorance in regard to pore-size, pore-shape, the distribution of connectivity, and pore topology of diatomite makes implementation difficult. Thus, the porous medium is represented by a Bethe lattice, with each flow connection having some conductivity governed by a conductivity distribution $G(g)$ where g is the conductivity of a single pore. The effective conductivity G_{eff} for such a network is given by the first derivative of a generating function $C(x)$ at the origin ,

$$G_{eff} = -ZC'(0) \tag{4.1}$$

where Z is the coordination number of the Bethe lattice (Stinchcombe, 1974) and the prime on C indicates differentiation with respect to the variable x which parameterizes the network.

The Laplace transform of the generating function satisfies the following recursive integral equation,

$$\int_0^\infty e^{-tx} C(x) dx = \frac{1-f}{t} + f \int_0^\infty G(g) \left\{ \frac{1+t}{g} + \frac{g^2}{(t+g)^2} \int_0^\infty \exp\left(\frac{x-g}{g+t}\right) C(x)^{Z-1} dx \right\} dg \qquad (4.2)$$

subject to the boundary condition, *C(0)* =1. In Eq. 4.2, *f* is the fraction of throats of the Bethe lattice that are available for flow. In the case of single phase flow and in the absence of silica diagenesis, all the throats of the network are available to flow and *f* equals 1.0. This remains true for dissolution as well. But in the case of deposition, some throats will clog, and hence, all of the throats will not contribute to flow. As deposition proceeds, the value of *f* decreases as pores fill with silica. Equation 4.2 can not be solved analytically as it is implicit in *C*(*x*), but various series approximations have been developed. For our model, we use the series approximation of Heiba *et al.* (1992) and Heiba, (1985) (Appendix VIII).

The effective volume of a network at any stage in the diagenetic process is found from the volume distribution of the various throats, *V*(*v*). The effective pore volume of the network is,

$$V = \int_0^\infty V(v) dv \qquad (4.3)$$

where *v* is the volume of an individual pore. Evaluating effective network conductivity and available network pore volume using Eq. 4.2 and Eq. 4.3 requires functional forms for the distribution functions *G*(*g*) and *V*(*v*) which correctly represent the porous medium under investigation. We consider a porous medium to have pores characterized by a dimensionless throat radius *r* and a frequency of occurrence *α*(*r*). Since *f* is the fraction of pores that are open, the distribution functions can be represented (Yortsos and Sharma,

1986) as,

$$G(g) = (1-f)\delta(g) + fX^A\alpha(r)g(r) \tag{4.4}$$

$$V(v) = (1-f)\delta(v) + fv(r) \tag{4.5}$$

where $g(r)$ and $v(r)$ are the functions that relate the size, r, of a pore to its individual conductivity and volume, respectively. The Dirac delta function, δ, indicates that the clogged pores do not contribute to conductivity and pore volume. The factor X^A, called accessibility of the network, accounts for the random distribution of throats in the network that causes some non clogged pores to be unavailable for flow because they are cut off from the main mass of open pores by clogged pores. The value of X^A depends on the fraction of throats that are clogged and the connectivity, Z, of the network.

For a Bethe lattice, the accessibility function of the network has been found analytically (Fisher and Essam, 1961). It is related to the fraction of open throats by,

$$X^A(f) = \begin{cases} f\left(1-(f^*/f)^{\frac{2Z-2}{Z-2}}\right) & ;f \geq f_c \\ 0 & ;f < f_c \end{cases} \tag{4.6}$$

where f_c is the percolation threshold, *i.e.* the minimum value of the allowable fraction of throats below which no flow across the lattice occurs and f^* is the root of the following equation,

$$f^*(1-f^*)^{Z-2} - f(1-f)^{Z-2} = 0 \tag{4.7}$$

such that the root $f^* \to 0$ as $f \to 0$ and $f \to 1$. In our calculations to follow, we use the series approximation to Eq. 4.7 provided by Larson and Davis (1982) as illustrated by Heiba (1985) (Appendix VIII).

The network model equations, Eqs. 4.1 to 4.7, are anchored to a real porous medium by a two step process:

(i) The functional forms of $g(r)$ and $v(r)$ are developed analytically, using a single-pore model suggestive of observed pore structure.

(ii) The form of $\alpha(r)$ is based on measured pore-size distributions for diatomite. Likewise, actual body-size distribution information is included. These steps are described in detail in the following sections.

4.3 Single-Pore Model

Every pore in a porous medium has at least two distinct parameters, throat size and body size. We use sinusoidal pores as shown in Fig. 4.2. The pore is periodically constricted according to the following dimensionless equation,

$$\lambda(z) = 1 - \left(\frac{1-\lambda_t}{2}\right)\left(1 + \cos\frac{2\pi z}{\xi R_b}\right) \tag{4.8}$$

where z is the distance along the axis, $\lambda = R(z)/R_b$, R_b is a characteristic pore-body dimension, $\lambda_t = R_t/R_b$ is the dimensionless throat radius sometime referred to as an aspect ratio, R_t is pore-throat radius, $\xi = L/R_b$, and L is the pore wavelength. Based on this representation of shape for a single pore and restricting the cross section to be circular, we find the single-phase conductivity and volume of a single pore analytically. Neglecting the influence of pore corners does not have a major effect on single-phase conductivity calculations.

4.3.1 Single-Pore Conductivity

We solve for single-phase Hagen-Poisuelle flow in a constricted pore analytically and relate pressure drop to flow by the following equation (see Appendix V),

$$\frac{\Delta p \pi R_b^4}{8qL\mu} = \frac{\left(9\lambda_t^2 - 6\lambda_t + 5\right)}{\sqrt{\lambda_t^7}} \tag{4.9}$$

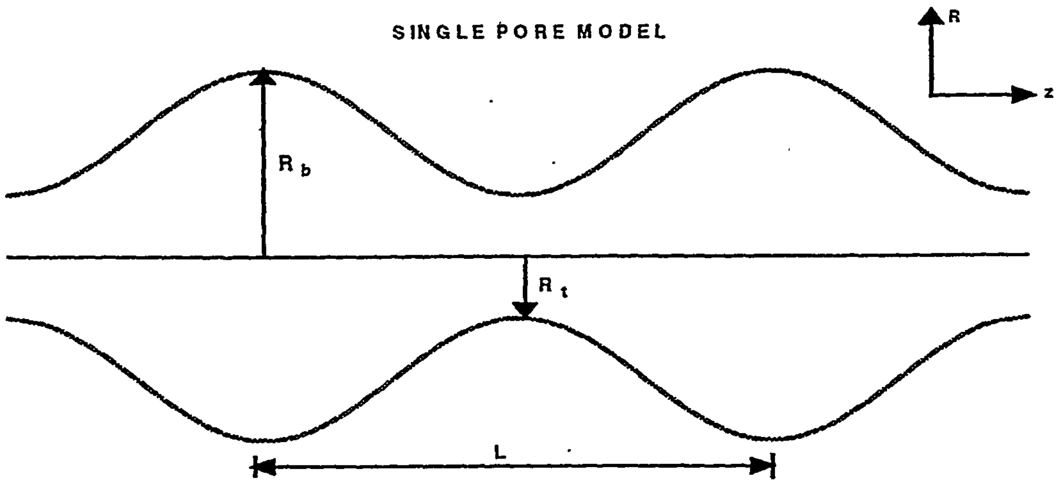

Figure 4.2a: Single-pore model.

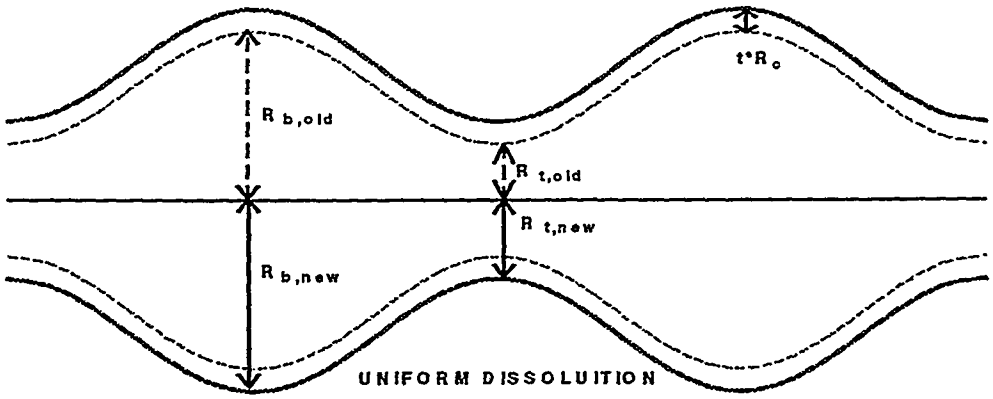

Figure 4.2 b: Uniform dissolution model.

where Δp is the pressure drop, μ is the viscosity, and q is the volumetric flow rate through the pore. In spite of periodic constrictions we suppose that flow is creeping because flow rates are very low and the Reynolds number is thereby small. We define a dimensionless hydraulic conductivity g for a single pore related to the pressure drop through it by,

$$g = \frac{qL\mu}{\Delta p}\frac{8}{\pi R_c^4} \tag{4.10}$$

where R_c is a characteristic radius. These two equations are combined to give the dimensionless single-phase conductivity of a single pore as,

$$g(r_t,\lambda_t) = \frac{8r_t^4}{\sqrt{\lambda_t}\left(9\lambda_t^2 - 6\lambda_t + 5\right)} \tag{4.11}$$

where $r_t = R_t/R_c$.

4.3.2 Single-Pore Volume

Assuming circular cross section, we find the volume of a single pore per unit wavelength to be (see Appendix VI),

$$V(R_b, R_t) = \frac{\pi}{8}R_b^2\left(3\lambda_t^2 + 2\lambda_t + 3\right) \tag{4.12}$$

Based on this equation, we define dimensionless volume per unit wavelength as follows,

$$V(\lambda_t, r_b) = \frac{\pi}{8}r_b^2\left(3\lambda_t^2 + 2\lambda_t + 3\right) \tag{4.13}$$

where $r_b = R_b/R_c$.

The single pore model, Eqs. 4.11 and 4.13, takes into account both body and throat sizes characterizing a pore. But the expressions generating conductivity and volume distributions require that the single-pore equations be in terms of a single characteristic dimension. We select the dimensionless throat radius to be this characteristic dimension. The choice is made because the Bethe lattice effective conductivity Eq. 4.1 is for the bond percolation problem, and bonds are analogous to throats in a porous medium. Thus Eq. 4.11 and Eq. 4.13 are modified to yield a form containing throat size only while still retaining embedded body size information.

4.3.3 Incorporation of Body Size Information

Equations 4.11 and 4.13 are made single variable equations without losing body-size information by averaging the equations over all possible body sizes associated with a given throat size. If $\alpha_b(r_t, r_b)$ is the frequency distribution of the dimensionless body radius, r_b, associated with a given dimensionless throat radius, r_t, then the effective conductivity and available volume associated with a throat size is given by (Appendix VII),

$$\langle g(r_t)\rangle = \int_r^\infty \alpha_b(r_t, r_b) g(r_t, \lambda_b) dr_b \tag{4.14}$$

$$\langle V(r_t)\rangle = \int_r^\infty \alpha_b(r_t, r_b) V(\lambda_t, r_b) dr_b \tag{4.15}$$

4.4 Porous Medium Characterization

A real porous medium is composed of pores of varying sizes with each pore characterized by a large main body and a narrow throat. The porous medium is characterized by the sizes of bodies and throats and their distributions. The body and throat size distributions can be accurately represented with bivariate gamma distribution functions,

$$\alpha = \frac{r^{a-1} e^{-br} b^a}{\Gamma(a)} \tag{4.16}$$

where a and b are parameters that characterize the distribution. The use of this function for diatomite body and throat distributions is supported by experimental results and scanning electron microscope (SEM) images as discussed in Chapter 3 of this report. Based on Eq. 4.16, we generate body and throat-size distributions; examples are shown in Fig 4.3 for diatomite. While developing our single-pore model, we also use the distribution $\alpha_b(r_t, r_b)$ to average over all possible body sizes that can be associated with a given throat size. This is the constrained pore distribution, also shown in Fig. 4.3 as a dashed line marked with solid circles. Physically, a throat must be connected to a body that is greater than or equal to throat size,

$$\alpha_b(r_t, r_b) = \begin{cases} 0 & ; r_b < r_t \\ \alpha_b(r_b) \,/ \int\limits_{r_t}^{\infty} \alpha_b(r_b).dr_b & ; r_b \geq r_t \end{cases} \tag{4.17}$$

4.5 Relating Porous Medium to Network

The properties we calculate from the network model are effective hydraulic conductivity and available network volume. These properties are related to permeability and porosity. Permeability can be related to effective conductivity by invoking Darcy's law and the definition of hydraulic conductivity, respectively,

$$\frac{q}{A} = -\frac{k}{\mu}\frac{\Delta p}{L} \tag{4.18}$$

$$k \propto \frac{\phi R_c^4 G_{eff}}{A_c} \tag{4.19}$$

where A_c ($=\phi A$)is the cross sectional area available to flow of fluid, k is permeability, and ϕ is porosity. We assume that this area depends on the average throat size $<R_t>$ squared and that porosity is proportional to available network volume. Thus, the permeability

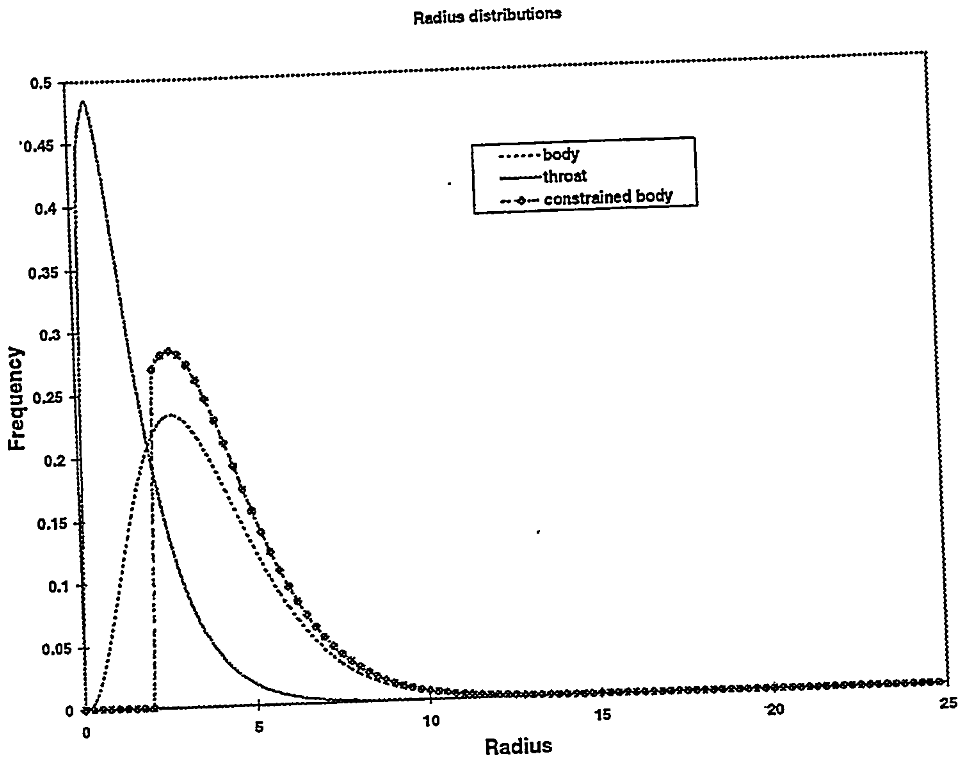

Figure 4.3: Body-size, throat-size and constrained body-size distributions.

change at any stage based on these equations is related to original permeability and pore volume, k_0 and $V_{eff,0}$, by the following relation,

$$\frac{k}{k_0} = \frac{V_{eff}}{V_{eff,0}} \frac{\langle R_t \rangle^2}{\langle R_{t,0} \rangle^2} \left(\frac{R_c}{R_{c,0}} \right)^4 \frac{G_{eff}}{G_{eff,0}} \tag{4.20}$$

Similarly, porosity at any stage of diagenesis can be related to original porosity and network parameters as,

$$\frac{\phi}{\phi_0} = \frac{V_{eff}}{V_{eff,0}} \tag{4.21}$$

Equations 4.20 and 4.21 relate network parameters to the porous medium at any stage in the diagenetic process. Thus, given the mass of silica dissolved or precipitated we obtain k and ϕ.

4.6 Pore Evolution Models

There are two distinct pore evolution mechanisms that occur in diatomite during steam drive. One is dissolution of the rock matrix and the other is precipitation of rock minerals. The following subsections describe the models that we choose for representing these aspects of diagenesis.

4.6.1 Dissolution

Silica dissolution has been studied widely in regard to alkaline water flooding. For instance, dissolution kinetics have been examined (Thornton and Radke, 1988; Saneie and Yortsos, 1985) as well as the migration of alkali (Bunge and Radke, 1982). The evolution of grain sizes and shapes during dissolution has also been studied via glass bead packs (Udell and Lofy, 1989). On the basis of observation of grain shapes and from assessing surface chemical potentials, it was suggested that silica dissolution was most likely to occur uniformly along pore walls (Udell and Lofy, 1989). In our pore network, we follow these results and dissolve pore walls uniformly. Each pore in the network suffers the same amount of dissolution as shown schematically in Fig. 4.2b.

We denote the dissolved thickness by t in dimensionless form. It has been non dimensionalized by the characteristic radius R_c. Based on this thickness, the dimensions of a pore after dissolution can be related to its original dimensions by,

$$r_{t,new} = r_{t,old} + t \tag{4.22}$$

$$r_{b,new} = r_{b,old} + t \tag{4.23}$$

These single pore equations are used to model the effect of dissolution at the network level. The body and throat size distributions are still given by the gamma distributions of Eq. 4.16. The distribution parameter a is related to average size by,

$$\langle r \rangle = a - 1 \tag{4.24}$$

The new average radius can be related to the old average radius and the thickness by,

$$\langle r \rangle_{new} = \langle r \rangle_{old} + t \tag{4.25}$$

Based on Eqs. 4.24 and 4.25, the parameters for generating the body or throat size distributions can be updated in the case of dissolution by,

$$a_{new} = a_{old} + t \tag{4.26}$$

Thus, body and throat size distributions during dissolution can be generated by parameters in Eq. 4.26. Since dissolution of the network does not block any pore, the pores at any stage of dissolution are always accessible to flow and X^A for dissolution will always be 1.0.

Based on this approach, different stages of dissolution of the rock matrix are denoted by different values of dimensionless thickness t. Then, the pore size distributions are updated and effective network conductivity and pore volume recalculated. Finally, the permeability and porosity change associated with a particular t is found.

4.6.2. Deposition

We use two different deposition models as given in Fig. 4.4. to explore clogging of pores. The first model, Fig. 4.4a, considers deposition to be a pore lining process and the second considers deposition to occur only at throats. Deposition at pore throats is indicated on Fig. 4.4b by dark gray shading. In both models, deposition takes place in a series of steps. Each step in the deposition sequence depends on the network condition in the previous step. At any stage of deposition, the condition of the network is determined by the condition of the throats constituting the network. Even though the radii change as deposition proceeds, we characterize all throats of the network at any stage of deposition by their original radii, *i.e.*, before the process of deposition starts. The extent of deposition is given by the largest blocked throat with original size r_i. The current size of this throat is zero. This implies that the frequency of a throat with current radius r is given by $\alpha_t(r+r_i)$ when r_i has been clogged. We also define X_i as,

$$X_i = \int_0^{r_i} \alpha_t(r)dr \tag{4.27}$$

This X_i defines the fraction of the original throats that are not allowed to the main flow due to deposition. The fraction of throats that are allowed to flow is, $1\text{-}X_i$. All of these allowed pores are not accessible to flow due to random connectivity of the network. Based on the current value of $1\text{-}X_i$ we estimate the current accessible fraction of allowable pores of the network by using Eq. 4.6. The fraction of completely blocked pores X_b is found by a population balance (Yortsos and Sharma, 1986),

$$X_b = \int_0^{X_i} \frac{X_A}{1-X_i} dX_i \tag{4.28}$$

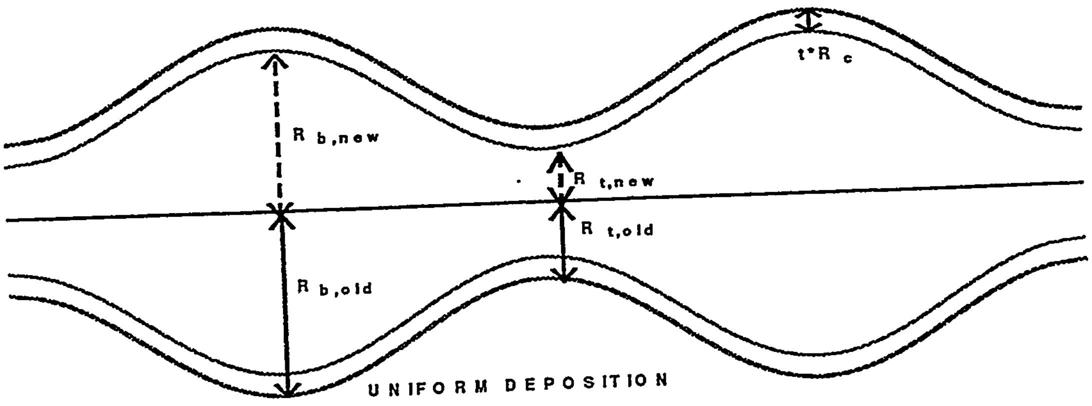

Figure 4.4a: Uniform deposition model.

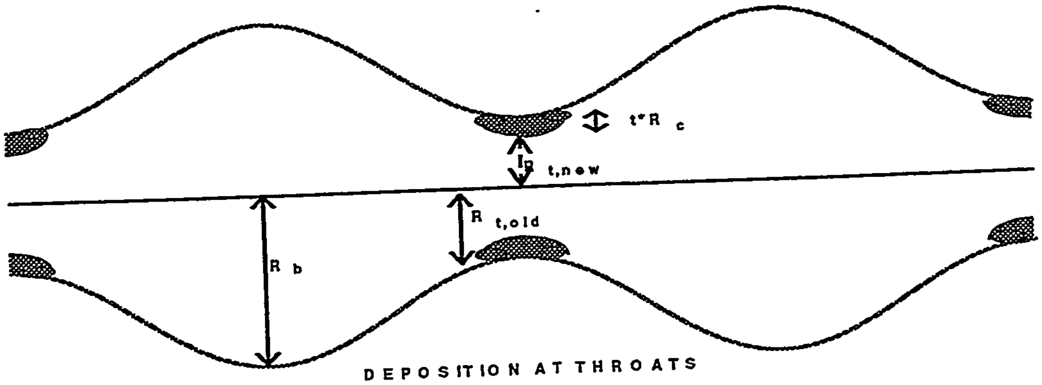

Figure 4.4b: Deposition at throats only.

Determination of these parameters at any stage of deposition thus tells us the condition of our network. A deposition step implies that pores with original throat size between r_i and $r_i+\Delta r_i$ block. First, we completely block accessible throats with current radius between 0 and Δr_i,. That is, for pores with the original radius between r_i and $r_i+\Delta r_i$. We call this amount of precipitate deposited volume V_1. Second, we deposit a layer of thickness Δr_i in all currently accessible throats with current radius between Δr_i and infinity. We call this deposited volume V_2.

To find the available pore volume at the stage $r_i+\Delta r_i$ of deposition we calculate V_1 and V_2 and subtract their total from network volume at start of the deposition step. Thus,

$$V_{eff}(r_i+\Delta r_i)=V_{eff}(r_i)-(V_1+V_2) \tag{4.29}$$

The deposition calculations start at $r_i=0$, and we go on successively subtracting volume from the base volume as calculated in Eq. 4.3. Formulas for V_1 and V_2 depend on where silica deposition occurs.

Deposition at throats only. In calculating the volumes V_1 and V_2 for deposition occurring only at pore throats, we hold the body size distribution constant and change only the throat-size distribution. Thus, the current body sizes are the same as the original body sizes. The volumes are calculated as,

$$V_1=\frac{X^A}{1-X_i}\int_0^{\Delta r_i}\alpha_t(r+r_i)\rangle V(r)\rangle dr \tag{4.30}$$

$$V_2=\frac{X^A}{1-X_i}\left[\int_{\Delta r_i}^{\infty}\alpha_t(r+r_i)\rangle V(r)\langle dr-\int_0^{\infty}\alpha_t(r+r_i+\Delta r_i)\rangle V(r)\langle dr\right] \tag{4.31}$$

Uniform deposition model. To find the volume change associated with a uniform deposition, we consider a single-pore model and calculate the volume that is deposited by a uniform layer of thickness t,

$$V_{dep}(r_b, r_t, t) = \pi t(r_b + r_t - t) \tag{4.32}$$

We then average V_{dep} over all possible body sizes to get volume change associated with a throat for a given thickness. The expression is,

$$\langle V_{dep}(r,t) \rangle = \int_r^{\infty} \alpha_b(r_b, r_t) V_{dep}(r_b, r_t, t) dr_b \tag{4.33}$$

We use this equation to calculate the deposition occurring in all throats with current radii ranging from 0 to ∞. Thus, for the uniform deposition case, the volume deposited is given by,

$$V_1 + V_2 = \frac{X^A}{1 - X_i} \int_0^{\infty} \alpha_t(r + r_i) \rangle V_{dep}(r,t) \langle dr \tag{4.34}$$

Conductivity calculation. The effective conductivity of the network is found by considering the three kinds of throats in the network at any deposition stage r_i:

- Throats that had original size less than r_i and are currently blocked completely and so do not contribute towards network conductivity.
- Throats that had original size greater than r_i and are accessible to flow and, hence, contribute towards network conductivity.
- Throats that had original size between 0 to ∞ but are not accessible to flow due to random connectivity of the network and, thus, do not contribute to flow.

The conductivity distribution function of the network is generated by,

$$G(g) = \left(X_b + X^{NA}\right)\delta(r) + \frac{X^A}{1 - X_i}\alpha_t(r + r_i)\rangle g(r)\langle \tag{4.35}$$

Once the conductivity distribution is known, we calculate the effective network conductivity using Eq. 4.2.

4.7 Discussion of Results

The models for deposition and dissolution were translated into the following algorithm to gauge the effect of dissolution and precipitation on permeability.

- A base case with given network connectivity, Z, average aspect ratio, λ_t, pore-body distribution, and pore-throat distribution is constructed.
- Next, we calculate the effective conductivity and available network volume of the base case.
- We then update the pore-body and pore-throat distributions according to the rules given above for a specified amount of silica precipitated or dissolved.
- The effective conductivity and available volume of the updated network are recalculated.
- Finally, Eqs. 4.20 and 4.21are used to relate the conductivity and available volume changes to permeability and porosity changes.

Connectivity and aspect ratio are varied independently for new base cases and the process given above is repeated. The code used to perform these calculations is attached as appendix IV of this report.

In the case of uniform dissolution, Fig. 4.5 represents the permeability versus porosity relationship for an aspect ratio of 20/3 and different values of coordination number Z. The plot has two distinct trends. First, the permeability increases rather dramatically for all values of Z. An order of magnitude increase in permeability is predicted if the porosity increases by 50%. Second, for a fixed value of porosity change,

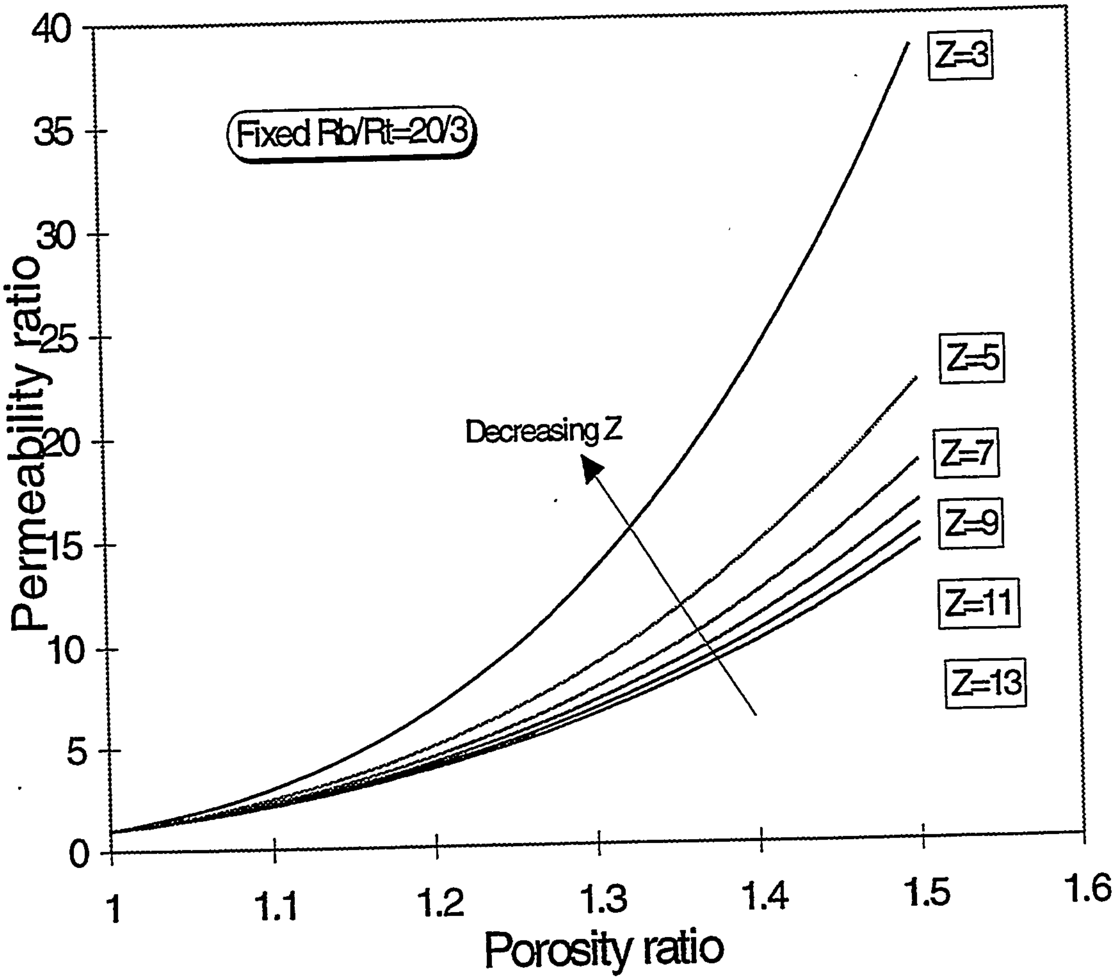

Figure 4.5: Dissolution case, permeability-porosity relation for different coordination numbers.

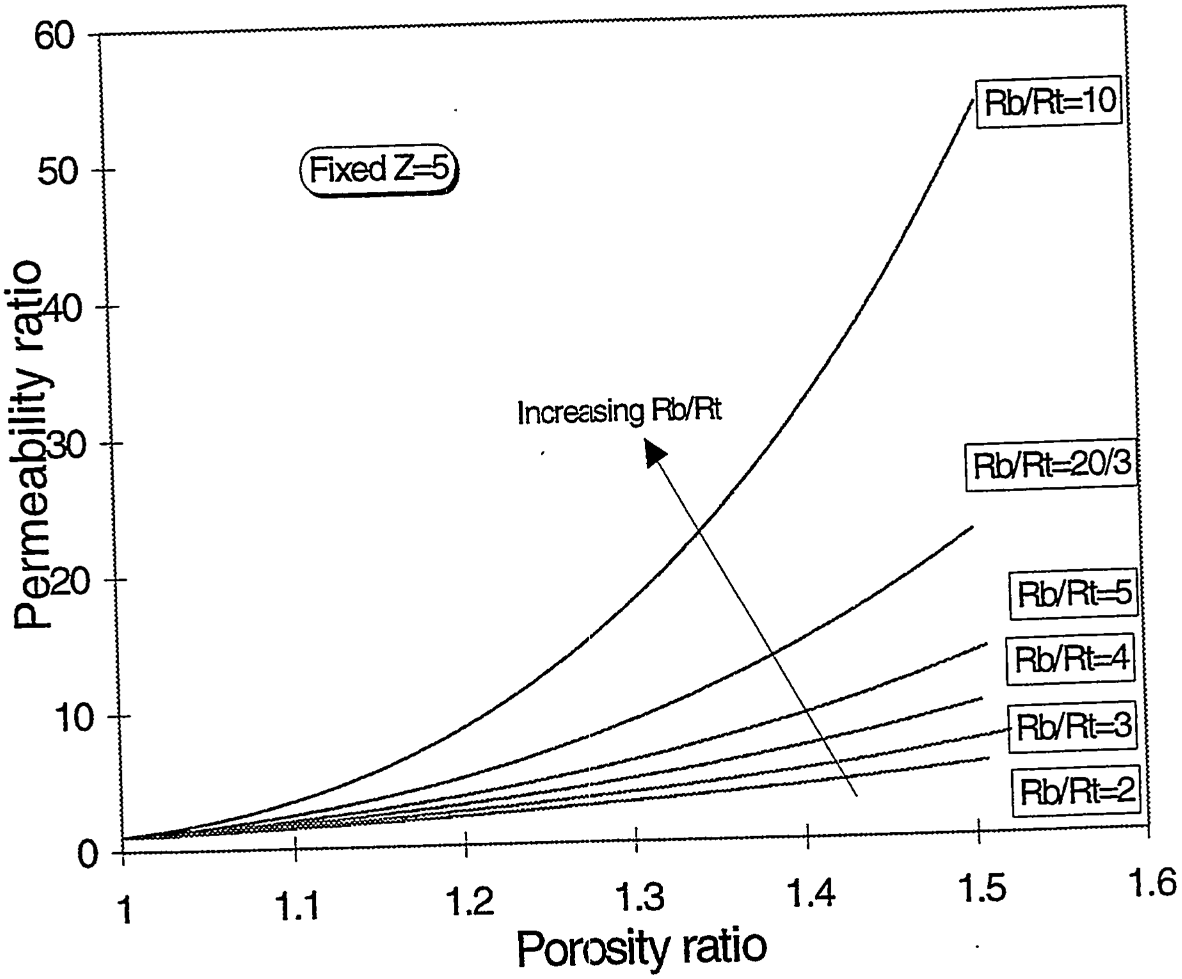

Figure 4.6: Dissolution case, permeability-porosity relation for different aspect ratios.

permeability increases most for small Z. For Z equal to 3, the permeability has increased 40 times when ϕ/ϕ_o reaches 1.5. As Z becomes larger the effect is less. It is reasonable that permeability increases most sharply and more severely for rocks with low connectivity as compared to rocks with high connectivity. The role of an individual pore throat on permeability is accentuated in networks with small connectivity.

Figure 4.6 displays similar dissolution calculations for the case of Z equal to 5 and variable pore aspect ratio. The most dramatic increases in permeability occur for the most constricted pores. When pore throats are small relative to pore bodies, a small amount of dissolution dramatically increases permeability. Note that the least constricted pores display the smallest amount of permeability increase relative to the base case.

Deposition results are similar to dissolution, except that the trends are reversed. Permeability decreases with porosity. Figure 4.7 shows the permeability versus porosity relationship for an R_b/R_t of 20/3 and various connectivities. Deposition occurs at throats only. For all values of Z, the decrease in permeability is very marked near ϕ/ϕ_o equal to 1 and becomes less steep as the network approaches blockage. Again, the most dramatic effects are seen in the networks with the least connectivity. Figure 4.8 displays the permeability versus porosity relationship for a Z of 5 and various pore throat to body size ratios. A small amount of silica deposited in a narrow throat in a poorly connected network, can substantially decrease network conductivity, and hence permeability.

For completeness, Figs. 4.9 and 4.10 present results for uniform deposition. Figure 4.9 applies to a fixed aspect ratio of 20/3 with variable Z, whereas Fig. 4.10 shows results for fixed connectivity and various R_b/R_t. Trends are similar to Figs. 4.7 and 4.8, but the trend of decreasing permeability with silica deposition is not as strong. Because deposition is pore lining rather than throat blocking, it takes a greater change in porosity to affect the same change in permeability. As expected, the most dramatic decreases in permeability are found for small Z and large λ_t.

The porosity changes shown in Figs. 4.5 to 4.10 are extreme and not expected in the field far away from the well bore. Changes up to about 10 % are likely the maximum (Koh, *et al.*, 1996). If we limit the porosity changes to 10 % and examine permeability

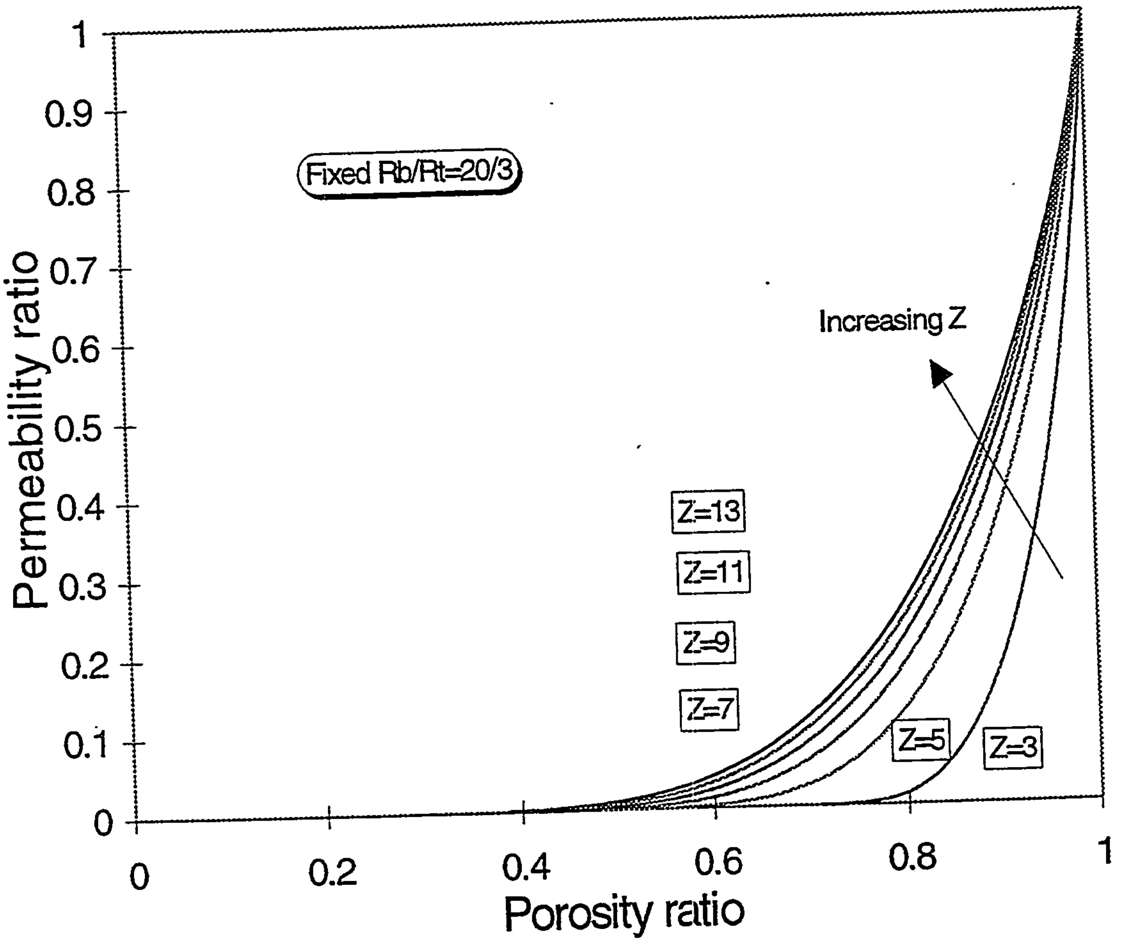

Figure 4.7: Throat deposition case, permeability-porosity relation for different coordination numbers.

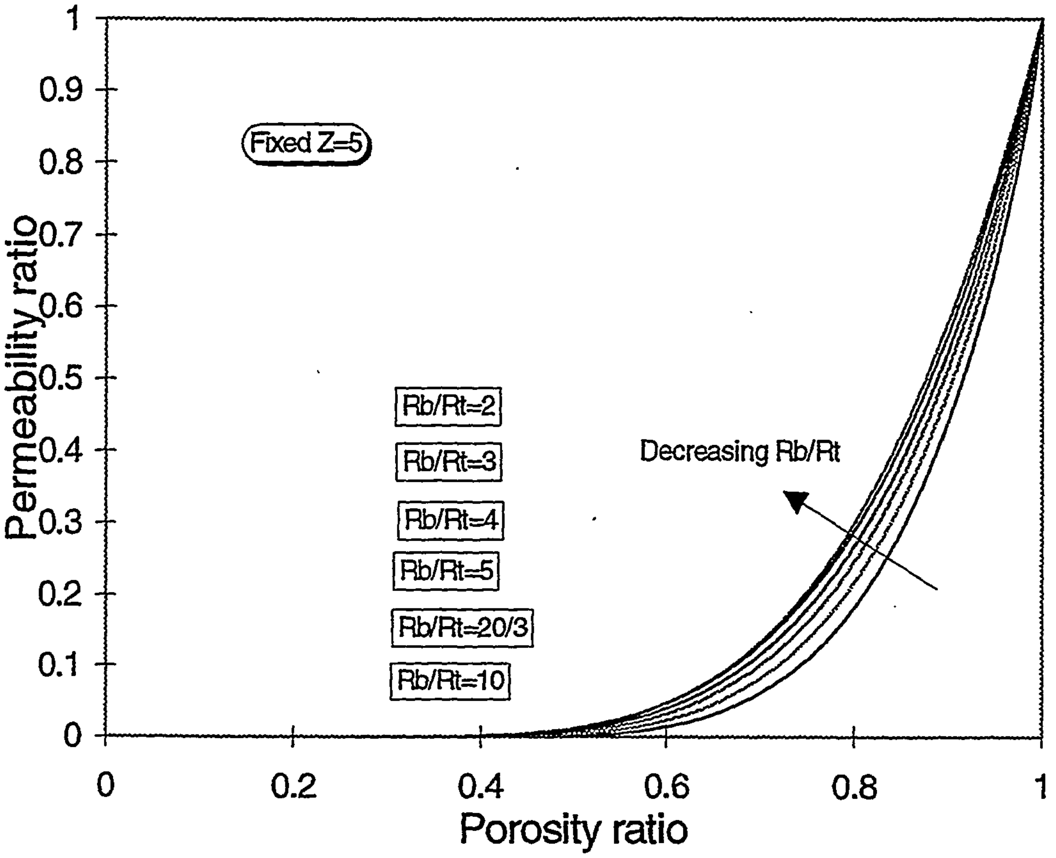

Figure 4.8: Throat deposition case, permeability-porosity relation for different aspect ratios.

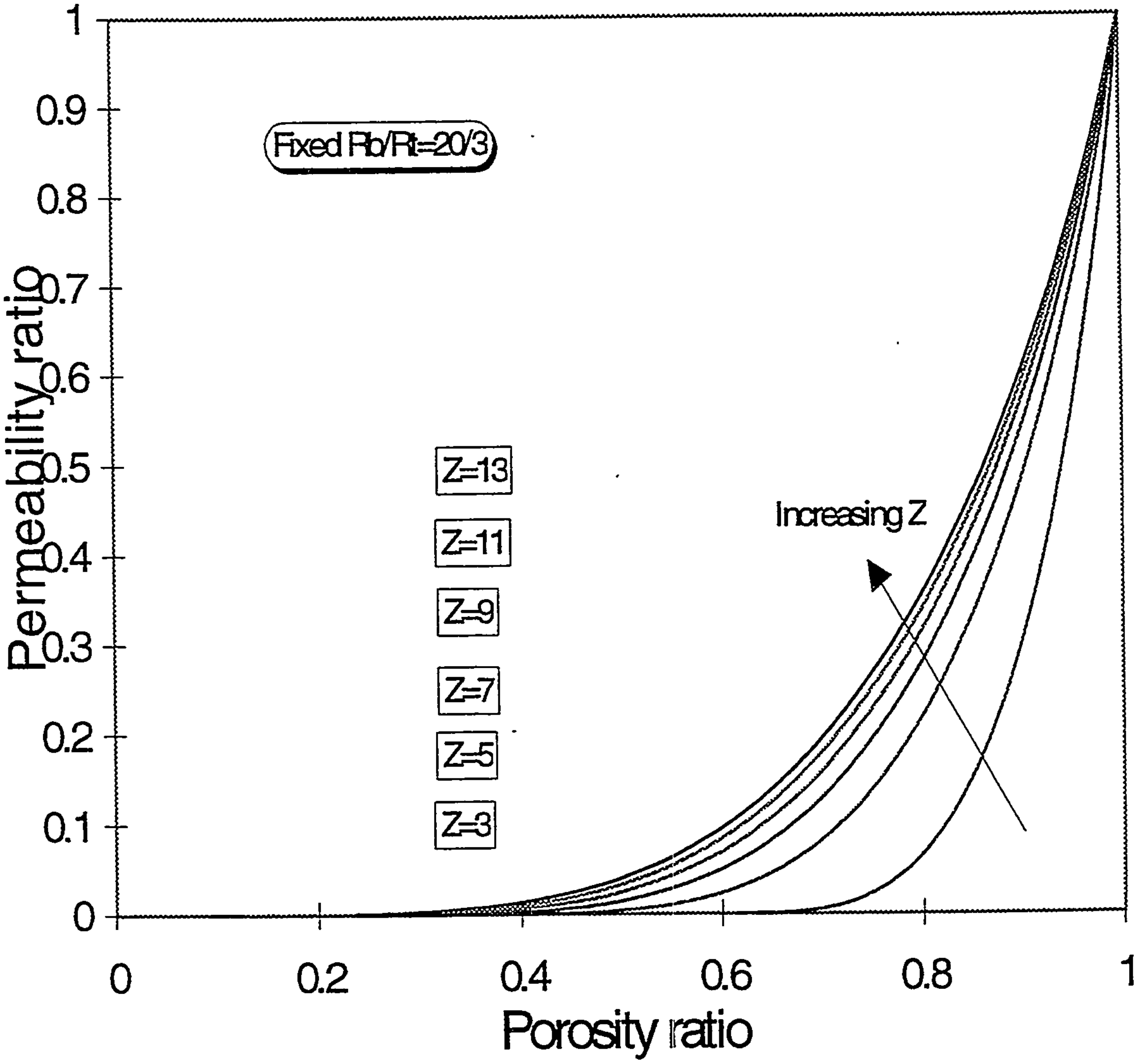

Figure 4.9: Uniform deposition case, permeability relation for various coordination numbers.

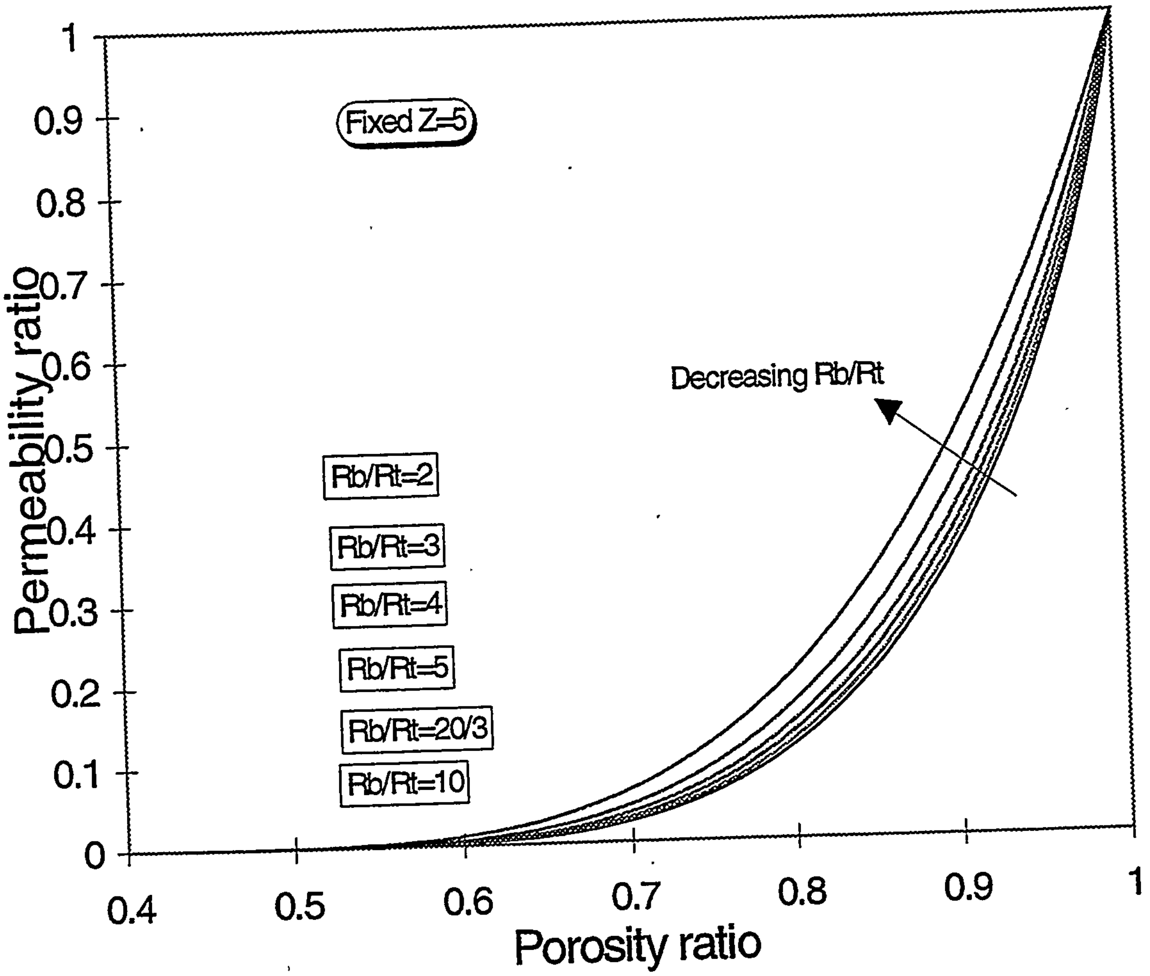

Figure 4.10: Uniform deposition case, permeability-porosity relation for various aspect ratios.

versus porosity on a log-log plot, a straight line relationship is found for dissolution and both modes of deposition. That is, the ratio of permeabilities varies with ϕ/ϕ_o raised to some power.

This point is illustrated graphically in Fig. 4.11 for the case of deposition at pore throats. The pore throat to body aspect ratio is fixed at 20/3, the network connectivity varies between 3 and 13, and deposition is limited to 10%. The power-law exponent increases with decreasing Z as indicated by the slopes of the lines. For a Z of 3 the exponent is about 16.5 while for Z = 13 it is about 6.6. The power-law trends exhibited in Fig 4.11 can be compared with the experimental results of Koh *et. al* (1996). They measured permeability of diatomite plugs that were flushed with hot, saturated silica laden water (204 °C). The diatomite plug was maintained at 49°C to induce silica deposition. Experimentally, they found that permeability reduction correlated with porosity decrease according to a power-law relationship. Their best-fit power-law exponent was 9. We find this power-law exponent for Z between roughly 5 and 7 on Fig. 4.11. In the case of pore-lining silica deposition, this model exhibits an exponent of 9 when Z is between 3 and 4 and R_b/R_t is 20/3. Hence, for reasonable network parameters, we reproduce the experimentally observed trend.

The power-law form exhibited in Fig. 4.11 suggests that the network results can be expressed according to

$$\frac{k}{k_0}=\left(\frac{\phi}{\phi_0}\right)^{\gamma} \tag{4.36}$$

where the power-law exponent γ is correlated with the network parameters Z and $\lambda_t = R_b/R_t$. We choose the following form for γ

$$\gamma = B(\lambda_t) + \frac{D(\lambda_t)}{Z - E(\lambda_t)} \tag{4.37}$$

The coefficients B, D, and E are functions of λ_t. We obtain them by fitting polynomial expressions to network results. Table 4.1 details the exact functional forms for each of these coefficients.

Table 4.1: Coefficients in Expression for Power-Law Exponent

CASE	$B(\lambda_t)$	$D(\lambda_t)$	$E(\lambda_t)$
Dissolution	$0.0201\lambda_t^2 + 0.645\lambda_t + 1.8633$	$-0.0168\lambda_t^3 + 0.3126\lambda_t^2 + 0.0525\lambda_t + 2.7042$	$-0.0279\lambda_t + 0.5886$
Uniform Dep.	$0.0003\lambda_t^2 + 0.147\lambda_t + 2.827$	$-0.0059\lambda_t^3 + 0.08\lambda_t^2 + 0.614\lambda_t + 5.2683$	$-0.0299\lambda_t + 1.7014$
Dep at Throats	$-0.0311\lambda_t^2 + 0.5699\lambda_t + 2.884$	$0.0128\lambda_t^3 - 0.3715\lambda_t^2 - 3.876\lambda_t + 2.9961$	$-0.0185\lambda_t + 1.6878$

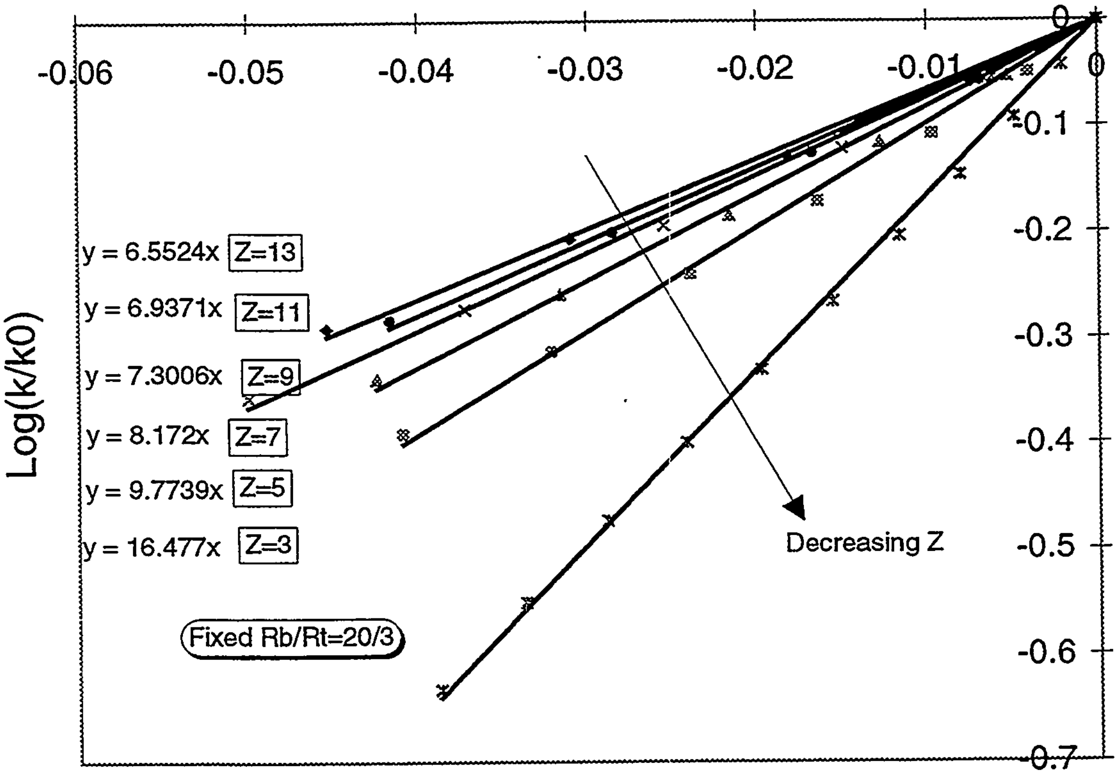

Figure 4.11: Straight line fits for permeability-porosity relations on log-log scale.

To verify the data reduction approach and Eqs. 4.36 and 4.37 , we plot network predicted changes in permeability (log k/k_0), such as those displayed in Figs. 4.5 to 4.10, versus the product of the power law exponent and logarithm of porosity change (γ log ϕ/ϕ_0). Deposition or dissolution is limited to a maximum of 10%. Figure 4.12 gives the results of this procedure for deposition at pore throats. Network results are given as individual data points and lie quite close to the straight line representing Eq. 4.36. Different symbols indicate differing values for network parameters Z and λ_t. Deviations from the straight-line behavior likely result from small errors in the polynomial representation of coefficients B, D, and E. Figures 4.13 and 4.14 show that the data reduction is successful for the pore-lining deposition and uniform dissolution cases as well. Hence, we obtain from our network calculations useful correlations of macroscopic porous medium properties. The power-law exponent is parameterized in terms of measurable rock quantities. Apart from checking the accuracy of the data reduction an error analysis (Appendix V) was also performed on the fits obtained from this method. The details of the analysis showed that the maximum difference introduced in the absolute values of permeability if predicted using Eq. 4.36 as compared to a detailed network calculation was at most of the order of 2 %.

4.8 Conclusions

Beginning with a simple network representation of diatomite, we are able to model permeability evolution as a function of porosity change. For moderate increases or decreases in porosity, we find a power-law relationship describing permeability alteration. Such a trend for silica deposition has been determined experimentally elsewhere. The power-law feature holds promise that permeability change during steam drive, or water flood, in diatomite can be incorporated into reservoir simulators.

Specifically, we find that the porosity-permeability relationship can modeled as a simple power-law relation only for moderate ranges of deposition and dissolution. At low

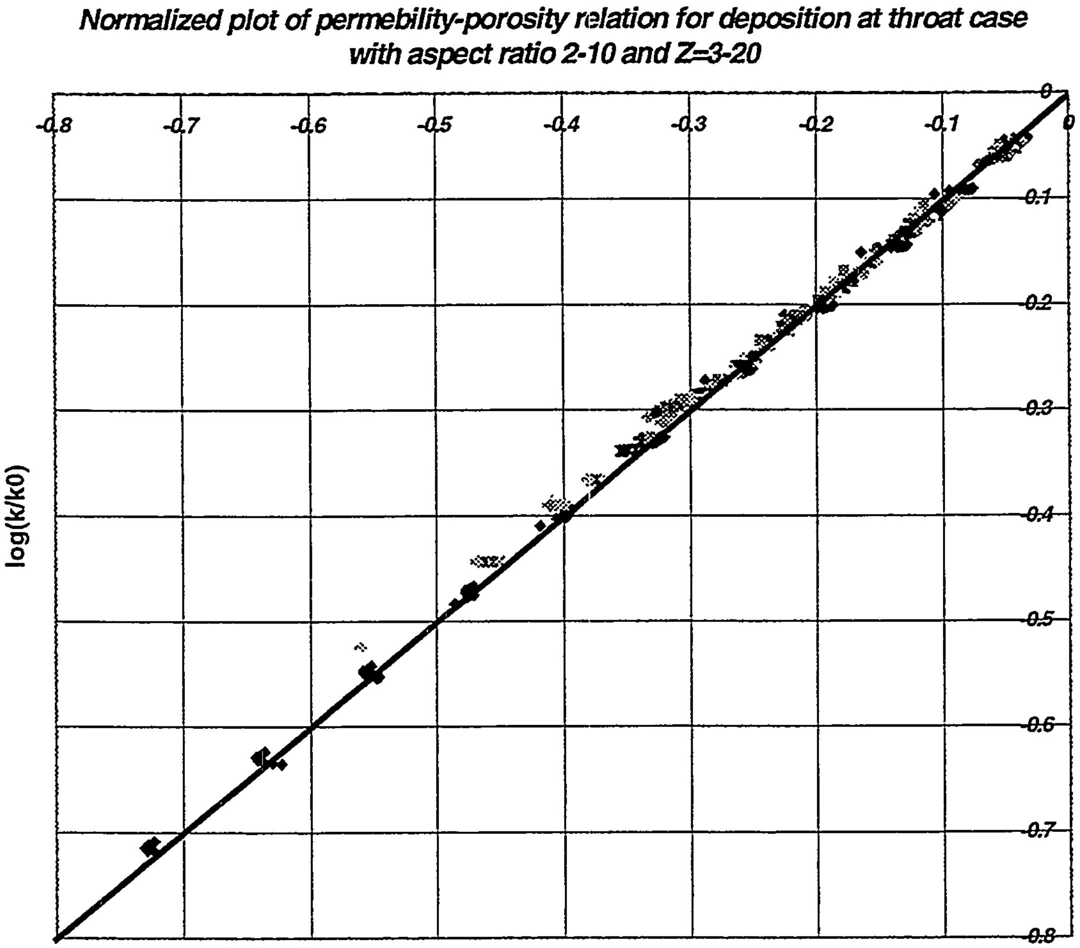

Figure 4.12: Normalized plot for deposition occurring at pore-throats only.

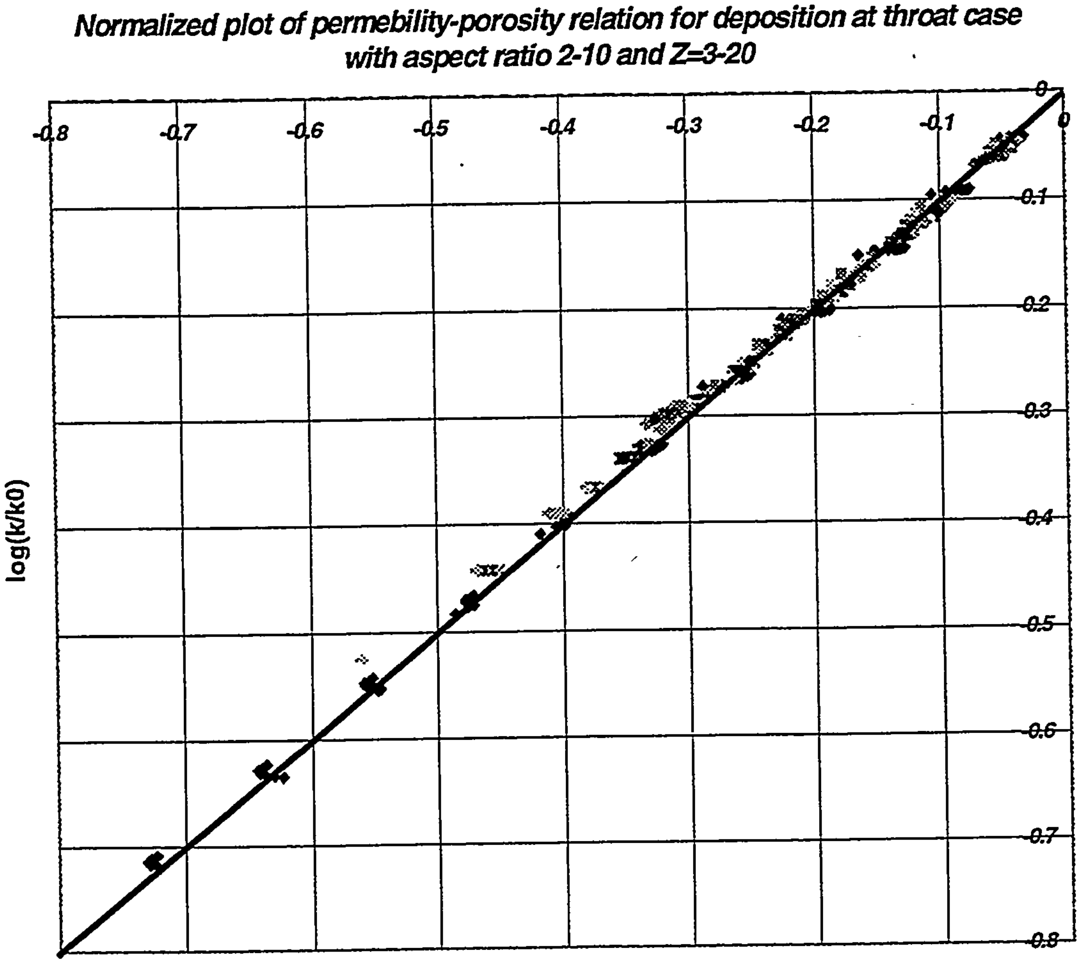

Figure 4.13: Normalized plot for uniform deposition.

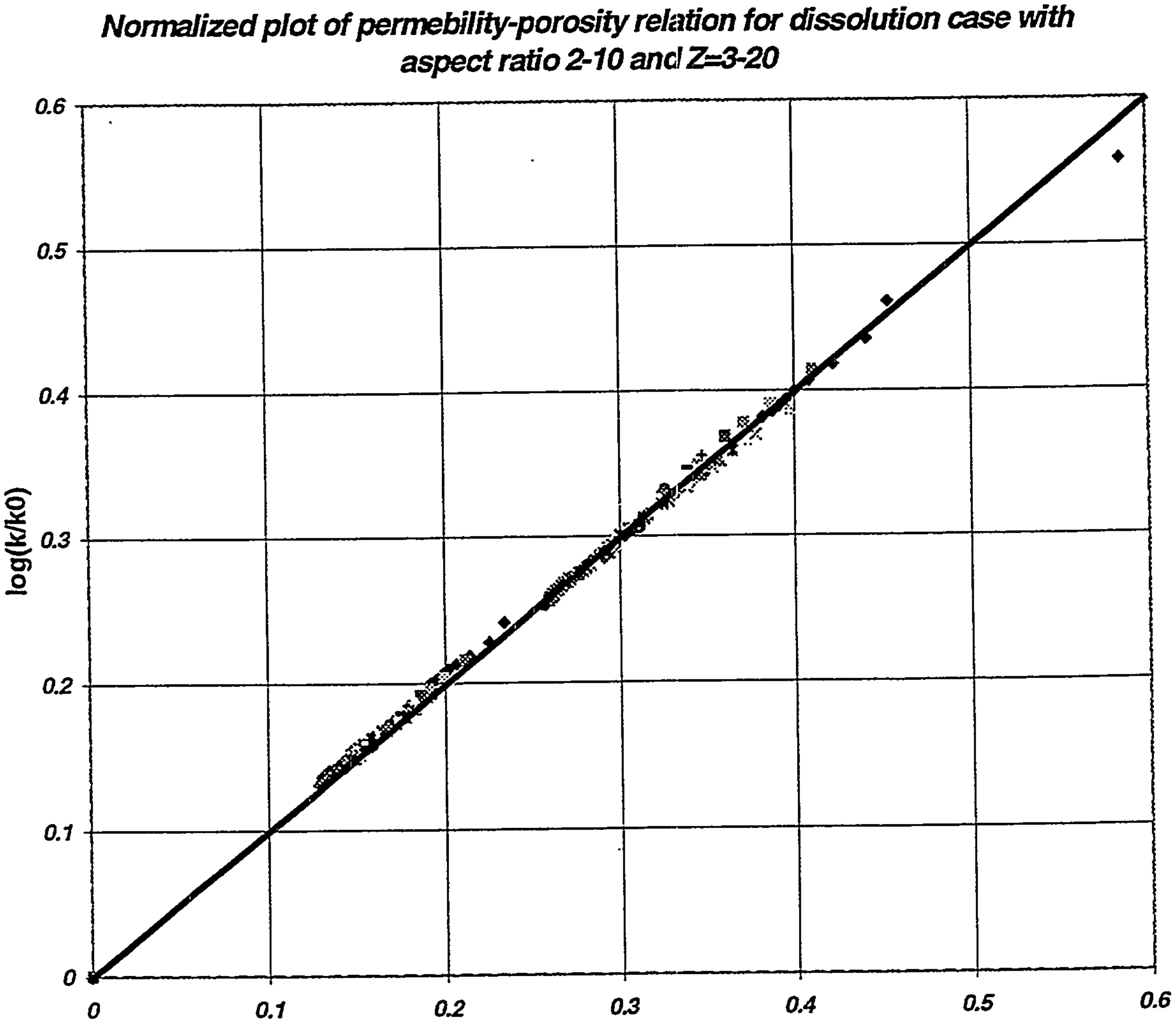

Figure 4.14: Normalized plot for dissolution case.

ranges of deposition, it is difficult to distinguish between deposition only at pore throats and pore-lining deposition of silica for expected pore body to throat aspect ratios and connectivity. Also, it is found that permeability change is most dramatic for networks with low connectivity or very small pore throats connected to relatively large bodies. For connectivity of 12 and greater at a fixed value of the throat to body aspect ratio, little variation in results is found as Z is increased.

Nomenclature

A = surface area

a,b = parameters in gamma distribution

B,D,E = coefficients for data reduction

C = silica concentration in the aqueous phase

C^o = equilibrium silica concentration

$C(x)$ = network generating function

f = fraction of pore throats available for flow

G = network conductivity distribution

g = conductivity distribution

J = Leverett J-function

k = permeability, Chap 3 , Chap 4

k = reaction rate constant, Chap 1

k^- = surface rate constant

L = distance between the producer and injector

M = mass of water available for deposition/dissolution

p = pressure

R = radius

r = rate of reaction

S = saturation of a phase

S_v = specific surface area of the porous medium

T = temperature

t = time, Chap 1

t = thickness of a deposited layer, Chap 4

u = darcy velocity

V = network volume distribution, Chap 4

V = volume of sample not occupied by mercury, Chap 3

V_{corr} = corrected volume of mercury in the sample

$V_{corr,850}$ = corrected volume of mercury in the sample at 850 psig

V_{sample} = volume of sample occupied by mercury

V_T = total sample volume

v = volume of a pore segment

X = fraction of throats not allowed to flow

X^A = network accessibility

x = direction of one-dimensional flow

x_D = dimensionless distance

Z = coordination number

z = distance in axial direction

Greek Symbols

α = frequency of occurrence

δ = Dirac delta function

Δ = difference operator

ϕ = porosity

Γ = gamma function

γ = power-law exponent

λ = radius non-dimensionalized by body size

μ = viscosity

θ = contact angle

ρ_l = density of water

σ = surface tension

ξ = pore length non-dimensionalized by body size

Subscripts

b = body

c = capillary, Chap 3

c = characteristic pore dimension, Chap 4

c = cross-sectional area for flow, Chap 4

eff = effective for flow

I = initial

i = fraction of original throats now blocked

J = injection

o = denotes properties before dissolution or precipiation

t = throat

nw = non wetting

w = wetting

$1,2$ = volumes deposited in precipitation model

References

1. Bhat, S.K., L.M. Castanier, and A.R. Kovscek: "Unpublished results: scanning electron microscopy and mercury porosimetry of diatomite," (1997).
2. Bohlmann, E.G., Mesmer, R.E., and Berlinski, P. : " Kinetics of Silica Deposition From Simulated Geothermal Brines," *Soc. Pet. Eng. J.* (August 1980).
3. Bunge, A.L. and C.J. Radke: "Migration of Alkaline Pulses in Reservoir Sands," *Soc. Pet. Eng. J.*, **22** (6) (1982) 998-1012.
4. Bruton, C.: Private Communication, Lawrence Livermore National laboratory (1996). C.R.C. Standard Mathematical tables,, Eleventh edition, Chemical Rubber Publishing Company, Cleveland, Ohio (1957).
5. C.R.C. Standard Mathematical tables, Eleventh edition, Chemical Rubber Publishing Company, Cleveland, Ohio (1957).
6. Dehghani, K. : "Caustic Consumption by Reservoir Rock at Elevated Temperatures," PhD thesis, University of Southern California (1983).
7. Fisher, M.E. and J.W. Essam: "Some Cluster Size and Percolation Problems," *Jour. of Mathematical Physics*, **2**(4) (1961) 609-619.
2. Fournier, R.O., and Rowe, J.J. : " The solubility of amorphous silica in water at high temperatures and pressures", *American Mineralogist* **62** (1977) 1120-1124.
3. Heiba, A.A.: "Porous Media: Fluid Distributions and Transport with Applications to Petroleum Recovery," PhD Thesis, University of Minnesota (1985) p. 565.
4. Heiba, A.A., H.T. Davis, and L.E. Scriven: "Effect of Wettability on Two-Phase Relative Permeabilities and Capillary Pressures," SPE 12172, in Proceedings of the SPE 58th Annual Technical Conference and Exhibition, San Francisco, CA (October 5-8, 1983).
5. Heiba, A.A., H.T. Davis, and L.E. Scriven: "Statistical Network Theory of Three-Phase Relative Permeabilities," SPE 12690, in Proceedings of the SPE/DOE Fourth Symposium on Enhanced Oil Recovery, Tulsa, OK (April, 1984).
6. Heiba, A.A., M. Sahimi, L.E. Scriven, and H.T. Davis: "Percolation Theory of Two-Phase Relative Permeability," *SPE Reservoir Engineering*, (Feb. 1992) 123-132.

7. Ilderton, D.C., Patzek, T.W., Rector, J.W., and Vinegar, H.J. : "Passive Imaging of Hydro-fractures in the South Belridge Diatomite," *SPE Formation Evaluation,* (March 1996) 46-54.
8. Johnston, R.M. and G.T. Shahin: "Interpretation of Steam Drive Pilots in the Belridge Diatomite," SPE 29621, in Proceedings of the SPE 65th Western Regional Meeting, Bakersfield, CA (March 8-10, 1995).
9. Koh, C.J., P.C. Dagenais, D.C. Larson, and A.S. Murer: "Permeability Damage in Diatomite Due to In-situ Silica Dissolution/Precipitation," SPE 35394, in Proceedings of the SPE/DOE Tenth Symposium on Improved Oil Recovery, Tulsa, OK (April 21-24, 1996).
10. Kovscek, A.R., R.M. Johnston, and T.W. Patzek: "Evaluation of Rock/Fracture Interactions During Steam Injection Through Vertical Hydraulic Fractures," *SPE Production and Facilities*, (May, 1997) 100-105.
11. Kovscek, A.R., R.M. Johnston, and T.W. Patzek: "Interpretation of Hydrofracture Geometry During Steam Injection Using Temperature Transients I. Model Formulation and Verification," *In Situ*, **20**(3) (1996) 251-288.
12. Kovscek, A.R., R.M. Johnston, and T.W. Patzek: "Interpretation of Hydrofracture Geometry During Steam Injection Using Temperature Transients II. Asymmetric Hydrofractures," *In Situ*, **20**(3) (1996) 289-309
13. Kumar, M. and F.D. Beatty: "Cyclic Steaming in Heavy Oil Diatomite," SPE 29623, in Proceedings of the SPE 65th Western Regional Meeting, Bakersfield, CA (March 8-10, 1995).
14. Larson, R.G. and H.T. Davis: "Conducting Backbone in Percolating Bethe Lattices," *J. Phys. C.: Solid State Phys.*, **15**(1982) 2327-2331.
15. Leverrett, M.C.: " Capillary Behaviour in Porous Solids", *Transactions of the American Institute of Mining and Metallurgical Engineers*, Vol. 142, (152-169).
16. Mohnot, S.M., Bae, J.H., and Foley, E.L.: " A Study of Mineral Alkali Reactions," SPE 13032, in Proceedings of the SPE 59th Annual Technical Conference, Houston, TX (September 16-19, 1984).

17. Murer, A.S., K.L. McClennen, T.K. Ellison, R.S. Timmer, D.C. Larson, K.D. Wolcott, T.M. Walker, and M.A. Thomsen: "Steam Injection Project in Heavy Oil Diatomite," SPE 38302, in Proceedings of the SPE 67th Annual Western Regional Meeting, Long Beach, CA (June 25-27, 1997).
18. Operating manual RUSKA Porometer; *Model No. 1051-801; Serial No. 31315.*
19. Operating manual RUSKA Gas Permeameter; *Model No. 1011-801 ; Serial No. 31496.*
20. Rimstidt, J.D., and Barnes, H.L. : " The Kinetics of Silica Water reactions," *Geochem. Cosmochim. Acta* **44** (1980) 1683-1699.
21. Ritter, H.L., and Drake, L.C.: " Pore-Size Distribution in Porous Materials, Pressure Porosimeter and Determination of Complete Macropore-Size Distributions"; *Industrial and Engineering Chemistry,* Vol 17, No 12 (782-791).
22. Saneie, S. and Y.C. Yortsos: "Kinetics of Silica Dissolution and Hydroxyl Ion Consumption in Alkaline Flooding," SPE 17409, in Proceedings of the CaliforniaRegional Meeting (March, 1985).
23. Schwartz, D.E.: "Characterizing the Lithology, Petrophysical Properties, and Depositional Setting of the Belridge Diatomite, South Belridge Field, Kern County, California", in *Studies of the Geology of the San Joaquin Basin,* S.A. Graham, and Olson, H.C., Editor. , The Pacific Section, Society of Economic Paleontologists and Mineralogists, Los Angeles, (1988) p. 281-301.
24. Stinchcombe, R.B.: "Conductivity and Spin-Wave Stiffness in Disordered Systems--An Exactly Soluble Model," *J. Phys. C.: Solid State Physics,* **7**(1974) 179-203.
25. Stosur, J.J. and A. David: "Petrophysical Evaluation of the Diatomite Formation of the Lost Hills Field, California," *Jour. Pet. Tech.*, **28** (1971) 1138-1144.
26. Thornton, S.D. and C.J. Radke: "Dissolution and Condensation Kinetics of Silica in Alkaline Solution," *Soc. Pet. Eng. Res. Eng.*, 3(2) (1988) 743-752.
27. Udell, K.S. and J.D. Lofy: "Permeability Reduction of Unconsolidated Media Caused by Stress-Induced Silica Dissolution," *SPE Formation Evaluation,* (Mar. 1989) 56-62.
28. Yortsos, Y.C. and M. Sharma: "Application of Percolation Theory to Noncatalytic Gas-Solid Reactions," *AIChE Journal,* **32**(1) (1986) 46-55.

Appendix I

The Silica Conservation Equation is

$$\frac{\partial}{\partial t}(C\phi\rho_w)+\frac{\partial}{\partial x}(Cu\rho_w)=r_i \tag{A1.1}$$

C is the silica concentration (mass of silica/mass of water), ϕ is the porosity of the medium, ρ_w is the water density, u is the darcy velocity of water flowing through the porous medium and r_i is rate of reaction. The dimensions of each term in Eq. A1.1 are mass of silica volume of water^{-1} time^{-1}.

Assuming that porosity remains constant, Eq. A1.1 can be written as,

$$\phi\rho_w\frac{\partial C}{\partial t}+u\rho_w\frac{\partial C}{\partial x}+\left[\frac{\partial}{\partial t}(\phi\rho_w)+\frac{\partial}{\partial x}(u\rho_w)\right]=r_i \tag{A1.2}$$

The water conservation equation is,

$$\frac{\partial}{\partial t}(\phi\rho_w)+\frac{\partial}{\partial x}(u\rho_w)=0 \tag{A1.3}$$

Assuming that the rate of reaction is first order and given by,

$$r_i=-k\left(C-C^0\right)\phi\rho_w \tag{A1.4}$$

k is the rate constant (time^{-1}) and C^o is the equilibrium concentration of silica in water at the temperature of reaction, the silica conservation equation reduces to,

$$\frac{\partial C}{\partial t}+\frac{u}{\phi}\frac{\partial C}{\partial x}=-k\left(C-C^0\right) \tag{A1.5}$$

Solving this equation subject to the following conditions,

- The initial concentration of silica in the medium is C_I.
- The injected phase has silica concentration of C_J.
- The temperature of the medium becomes T, which corresponds to an equilibrium silica concentration of C^0, and this temperature remains constant during the injection process.

These can be mathematically expressed as the following boundary and initial conditions subject to which the rate equation is to be solved.

Boundary condition (BC)

$$C(0,t) = C_J \tag{A1.6}$$

Initial condition (IC)

$$C(x,0) = C_I \tag{A1.7}$$

The differential equation Eq. A1.5 when converted into Laplace space become,

$$s\Psi - C(x,0) + \frac{u}{\phi}\frac{\partial \Psi}{\partial x} = -k\Psi + \frac{kC^0}{s} \tag{A1.8}$$

s is the parameter in Laplace space and Ψ is the concentration in Laplace space. The BC in Laplace space becomes,

$$\Psi(0,s) = \frac{C_J}{s} \tag{A1.9}$$

The differential equation Eq. A1.8 is an ODE and can be re-written as,

$$\frac{\partial \Psi}{\partial x}+\frac{\phi}{u}(s+k)\Psi = C_I + \frac{kC^0}{s} \tag{A1.10}$$

This equation is of the form,

$$\frac{dy}{dx}+P(x)y = Q(x)$$

The solution of this differential equation is,

$$y \times IF = \int IF \times Q dx + cons.$$

where,

$$IF = e^{\int P dx}$$

Thus, for Eq. A1.10, the IF is

$$IF = \exp\left(\frac{\phi}{u}[s+k]x\right) \tag{A1.11}$$

and,

$$Q = C_I + \frac{kC^0}{s} \tag{A1.12}$$

Thus the solution in Laplace space is,

$$\Psi = \frac{C_I + kC^0/s}{s+k} + A\exp\left(-\frac{\phi}{u}[s+k]x\right) \tag{A1.13}$$

where A is a constant. This constant is evaluated using the BC of Eq. A1.9 ,

$$A=\frac{C_J}{s}-\frac{C_I+kC^0/s}{s+k} \tag{A1.14}$$

The complete solution to the silica conservation equation in Laplace space is then,

$$\Psi(x,s)=F(s)+\left(\frac{C_J}{s}-F(s)\right)\exp\left(-\frac{\phi}{u}[s+k]x\right) \tag{A1.15}$$

where,

$$F(s)=\frac{C_I+kC^0/s}{s+k} \tag{A1.16}$$

To find the solution to silica conservation equation we need to find the inverse Laplace transform of the solution in Laplace space, *i.e.*, Eq. A1.15. To do that we will need to find the inverse Laplace transform of *F(s)*. The inverse Laplace transform of *F(s)* is found by breaking it into its partial fractions,

$$F(s)=\frac{C_I+kC^0/s}{s+k}=\frac{C^0}{s}+\frac{C_I-C^0}{s+k} \tag{A1.17}$$

Thus the inverse transform *f(t)* is given by,

$$f(t)=C^0+\left(C_I-C^0\right)\exp(-kt) \tag{A1.18}$$

The inverse Laplace transform of Eq. A1.15 is thus found using Eq. A1.18 to give,

$$C(x,t)=C^0+\left(C_I-C^0\right)\exp(-kt)+\left[\left(C_J-C^0\right)\exp\left(-\frac{\phi xk}{u}\right)-\left(C_I-C^0\right)\exp(-kt)\right]H\left(t-\frac{\phi x}{u}\right) \tag{A1.19}$$

The H in this equation is a step function. This general solution can be written also as,

$$\begin{aligned} C(x,t) &= C^0 + \left(C_I - C^0\right)\exp(-kt) \qquad ; \qquad t < \frac{\phi x}{u} \\ C(x,t) &= C^0 + \left[\left(C_J - C^0\right)\exp\left(-\frac{\phi xk}{u}\right)\right] \qquad ; \qquad t \geq \frac{\phi x}{u} \end{aligned} \tag{A1.20}$$

This is the general solution to the advective–reactive transport equation that is used in this report.

Appendix II

Possible Pore Bodies

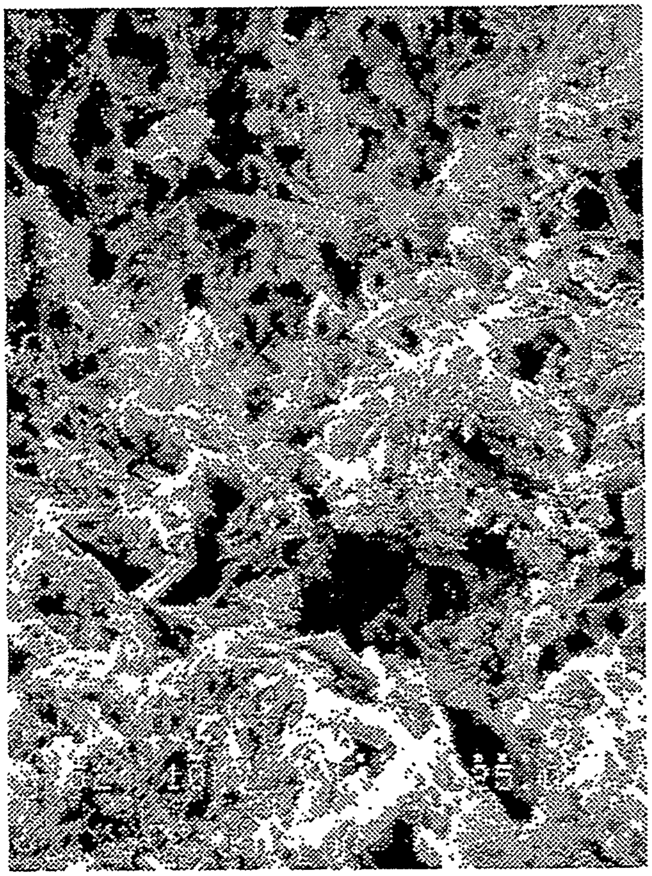

Figure A2.1 :Magnification=1200X

Scale:=25 μm

Flow paths that could be pore bodies

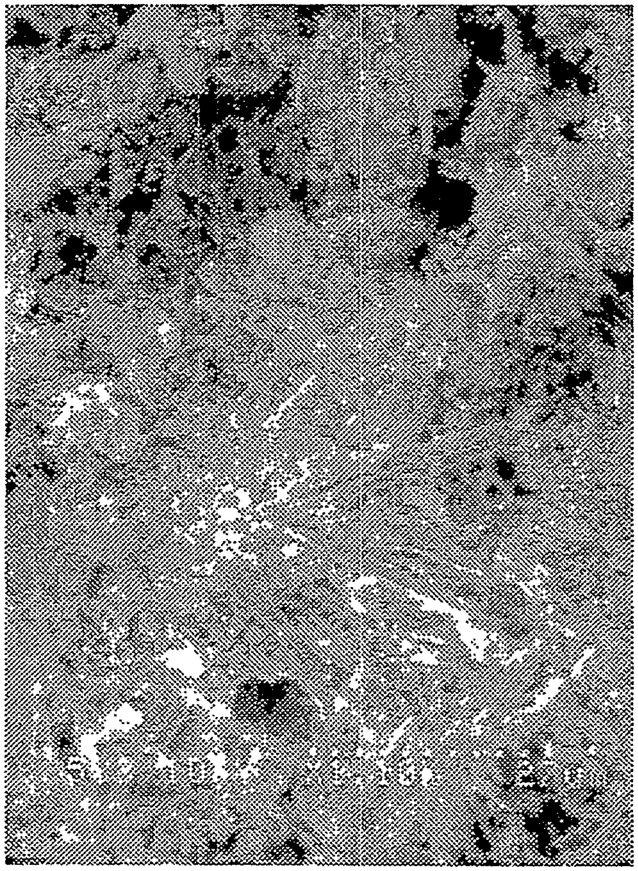

Figure A2.2 :Magnification=1100X
Scale:=27 μm

Flow paths that could be pore bodies

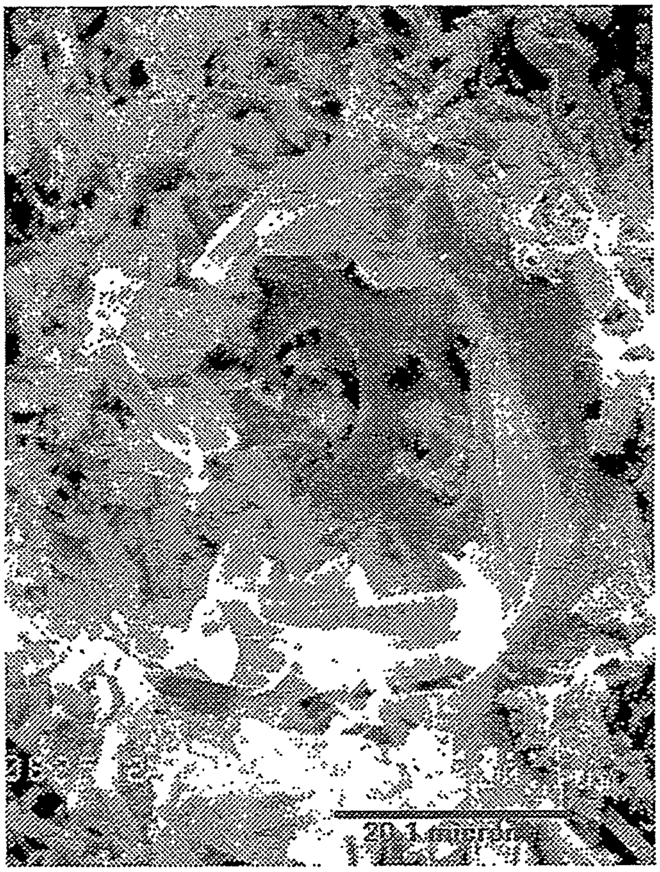

Figure A2.3 :Magnification=1490X
Scale:=20.1 μm

Flow paths that could be pore bodies

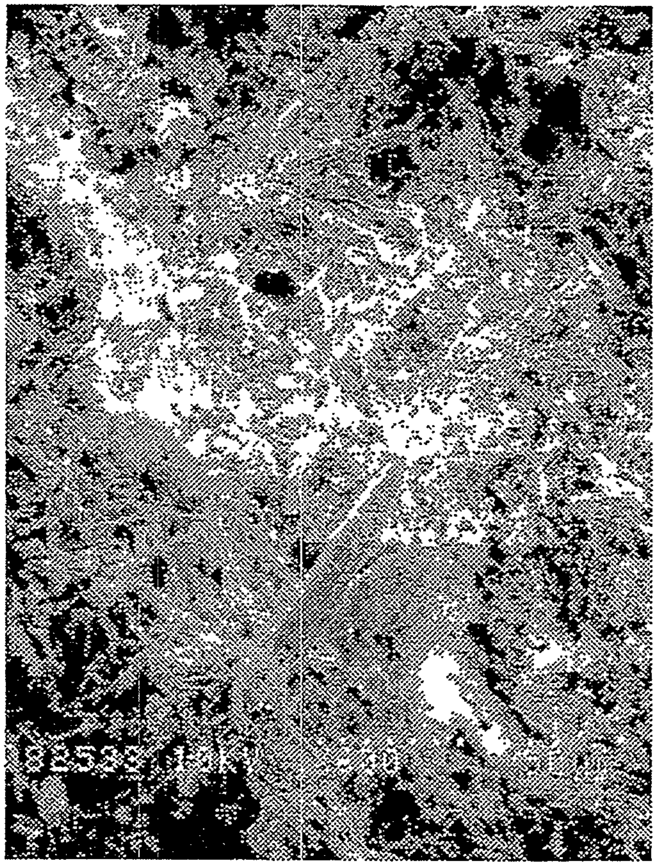

Figure A2.4 :Magnification=600X

Scale:=50 µm

Flow paths that could be pore bodies.

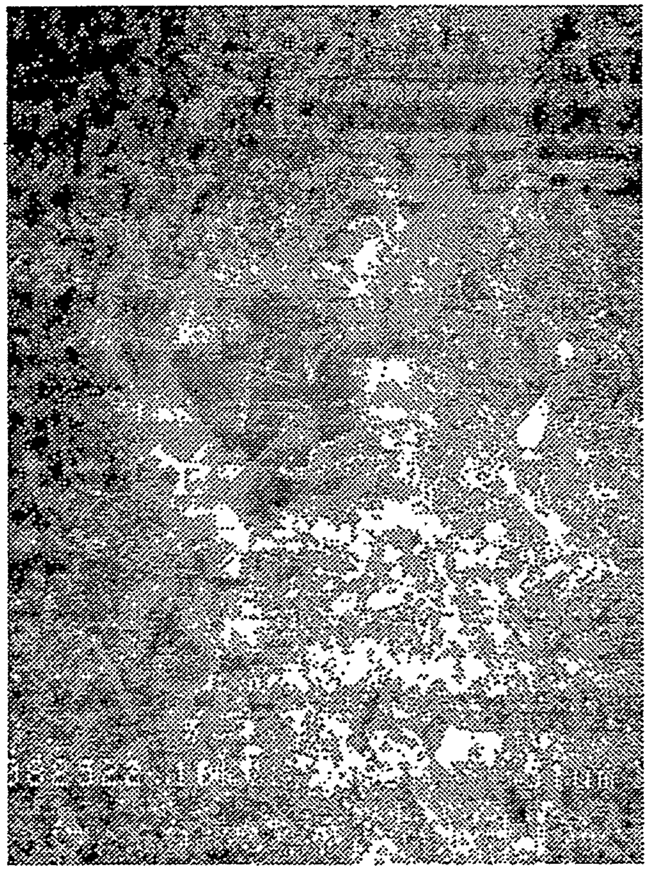

Figure A2.5 :Magnification=590X

Scale:=51 μm

Flow paths that could be pore bodies

Possible Pore-Throats

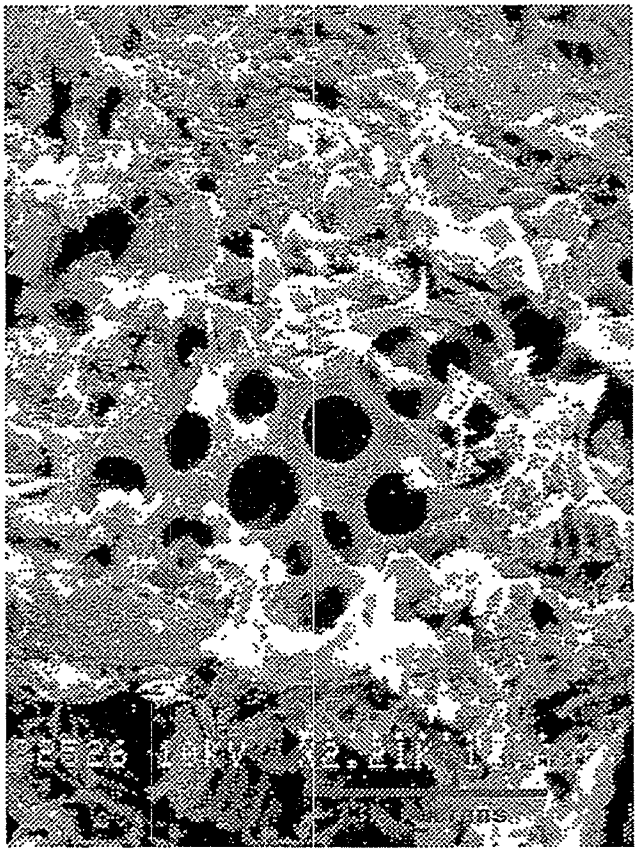

Figure A2.6 :Magnification=2210X

Scale:=13 µm

Flow paths that could be pore-throats

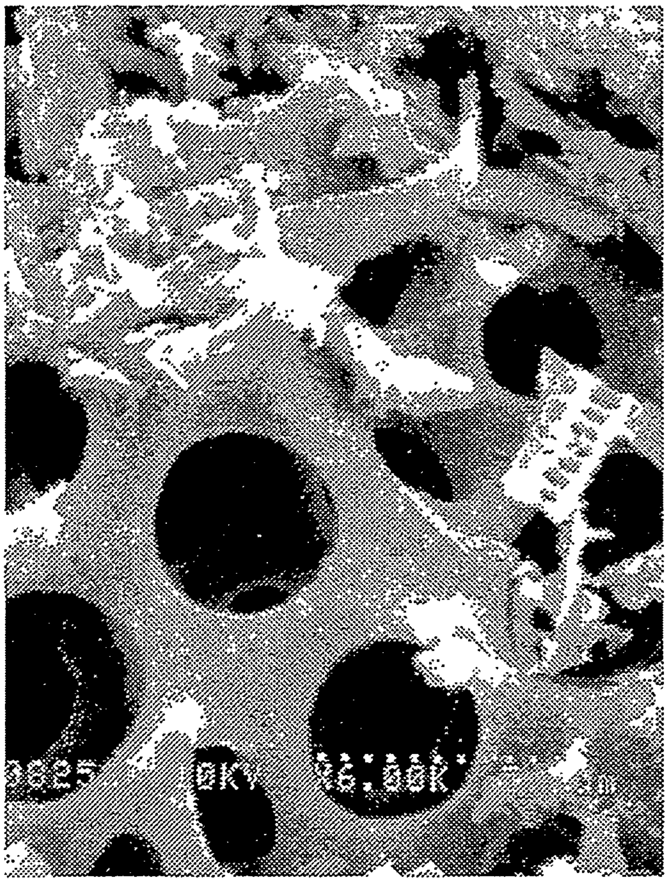

Figure A2.7 :Magnification=6000X

Scale:=5 µm

Higher magnification of the center of Fig. A2.6

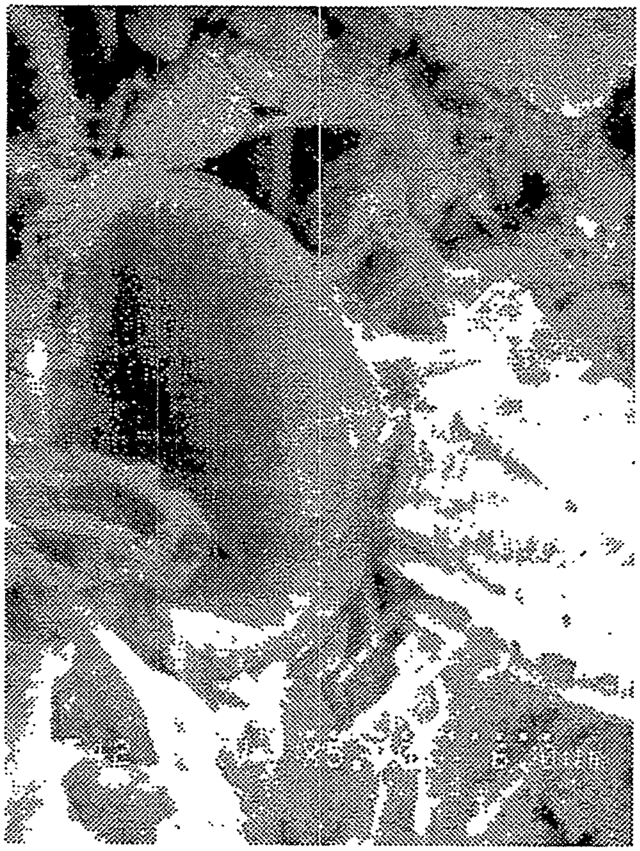

Figure A2.8 :Magnification=5000X
Scale:=6 µm

Flow path that could be pore-throats

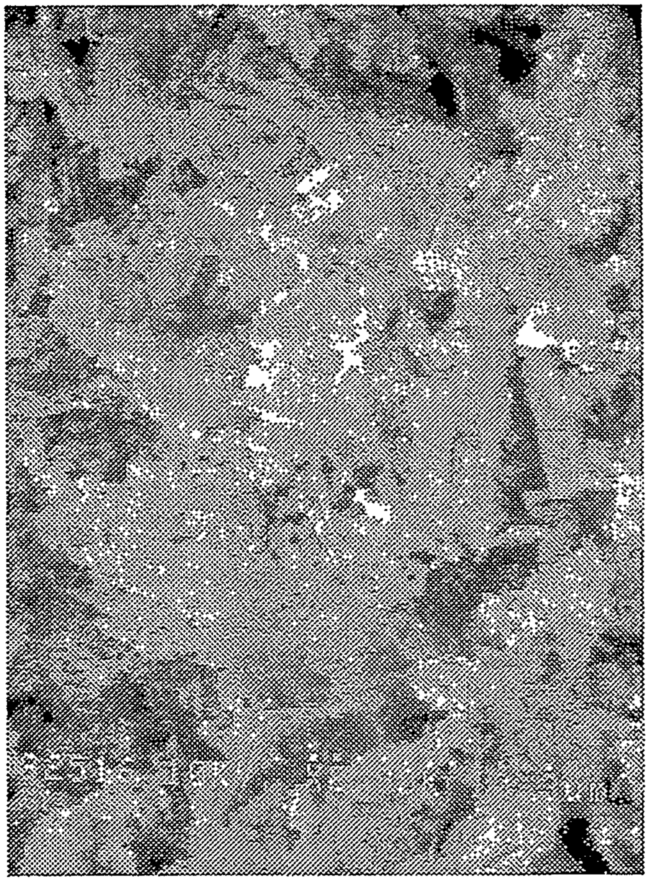

Figure A2.9 :Magnification=2900X
Scale:=10.3 μm

Lack of large scale flow paths in diatomite

Complete Diatoms

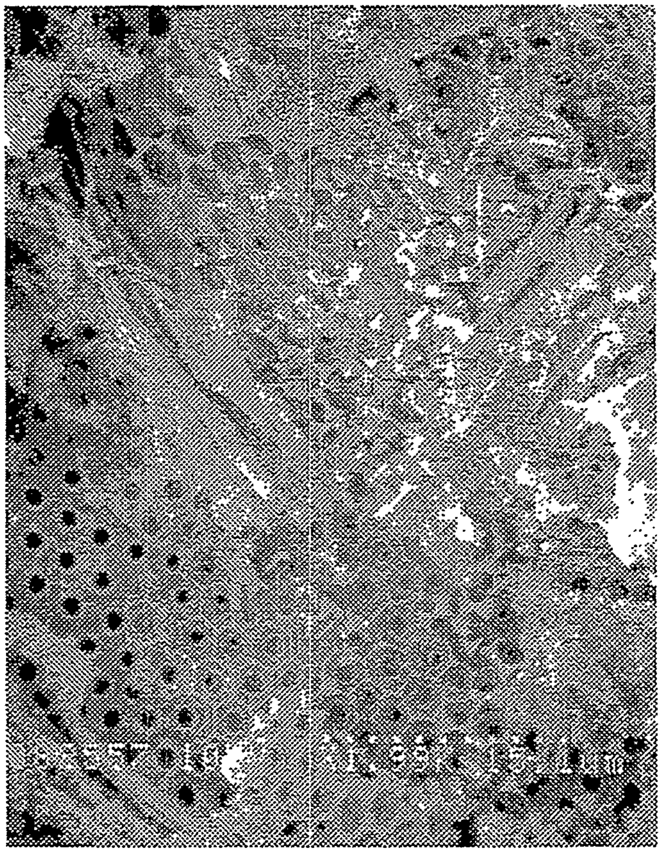

Figure A2.10 :Magnification=1990X
Scale:=15.1 µm

SEM of a complete diatom

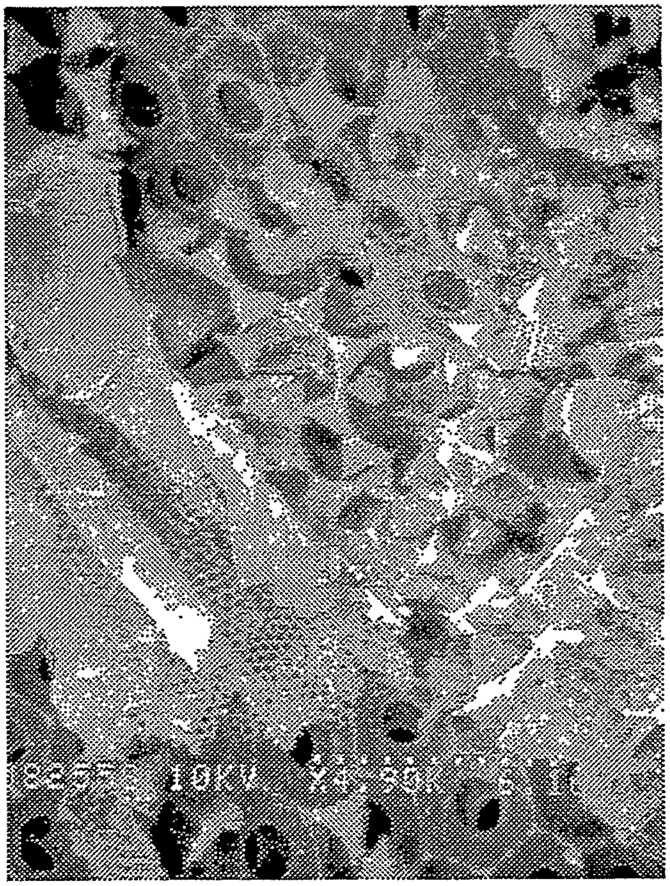

Figure A2.11 :Magnification=4900X

Scale:=6.1 µm

Center of the complete diatom of Fig. A2.10 at a higher magnification

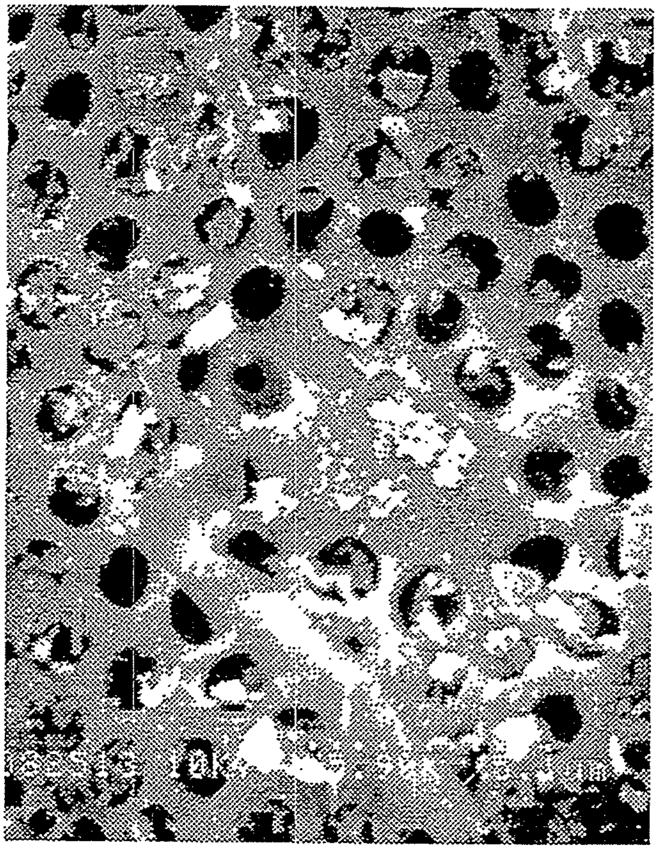

Figure A2.12 :Magnification=5900X

Scale:=5.1 μm

Center of the complete diatom of Fig. 3.9 at a higher magnification

Debris blocking diatomite flow paths

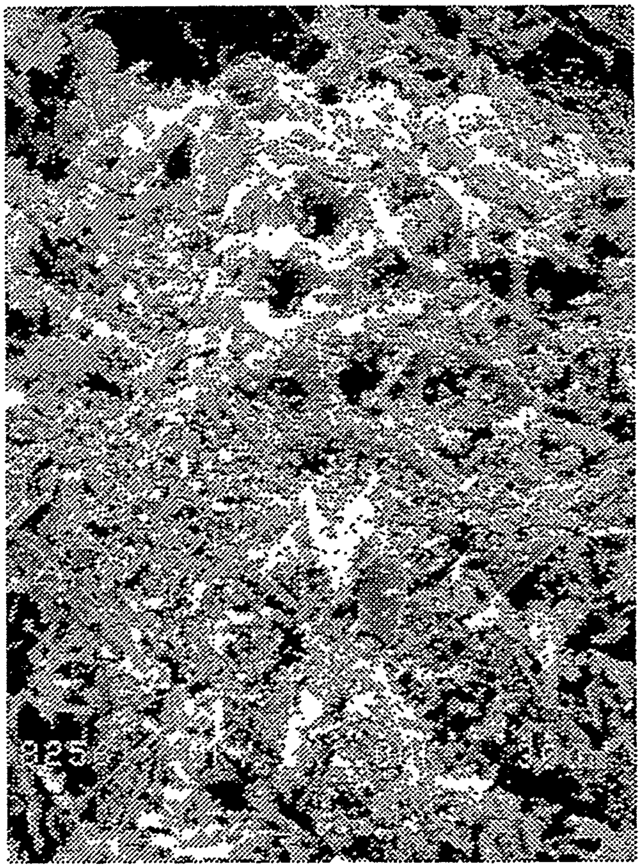

Figure A2.13 :Magnification=1000X
Scale:=30 µm

Crushed diatomite remains blocking possible flow paths

Figure A2.14 :Magnification=2000X
Scale:=15 μm

Center of Fig. A2.13 at a higher magnification

Appendix III

Pressure-Volume Data for Mercury Porosimetery

RUN 1

Vol reading of empty pycnometer (V_{em})=	50	cm^3
Vol reading of full pycnometer ($V_{full,1}$) @ atm=	2.25	cm^3
Vol of pycnometer (V_{pyc})=	47.75	cm^3
Vol reading of full pycnometer (V_{full}) @ 850 psig=	1.79	cm^3
Volume expansion of pycnometer =	0.46	cm^3
Volume reading with core @ atm=	9.225	cm^3
Bulk volume of sample =	6.975	cm^3

POROSITY calculation

Vol at reading with Hg in the sample @850psig=	4.5	cm^3
porosity =	0.61147	
pore vol =	4.265	

Mercury Intrusion Data/ Calculations

Table A3.1: Mercury Intrusion Data for RUN 1.

P(psig)	Volume Reading (cm^3)	V_{corr}^* cm^3	Volume of Hg in sample cm^3	S_{nw}
0	9.225	0	0	0
20	8.9	0.05	0.275	0.064478
48	8.8	0.10656	0.31844	0.074664
55	8.775	0.11825	0.33175	0.077784
103	8.7	0.171157	0.35384299	0.082964
140	8.595	0.185464	0.4445362	0.104229
149	8.5	0.188944	0.53605617	0.125687
155	8.3	0.191264	0.73373615	0.172037
162	8.1	0.193971	0.93102946	0.218295
175	7.9	0.198997	1.12600275	0.26401
192	7.7	0.205571	1.31942936	0.309362
223	7.5	0.217557	1.50744259	0.353445
245	7.3	0.226064	1.69893585	0.398344
268	7.1	0.234958	1.89004244	0.443152
290	6.9	0.243464	2.0815357	0.488051
310	6.7	0.251198	2.2738023	0.533131
332	6.5	0.259704	2.46529556	0.578029
358	6.3	0.269758	2.65524214	0.622566
380	6.1	0.278265	2.8467354	0.667464
410	5.9	0.289865	3.0351353	0.711638
448	5.7	0.304558	3.22044184	0.755086
485	5.5	0.318865	3.40613505	0.798625
532	5.3	0.337038	3.58796156	0.841257
590	5.1	0.359465	3.7655347	0.882892
660	4.9	0.386532	3.9384678	0.923439
750	4.7	0.421333	4.1036675	0.962173
850	4.5	0.46	4.2650005	1

- *This is volume correction due to pycnometer expansion under pressure calibrated separately. The calibration is at the end of this appendix.

Mercury Retraction Data/ Calculations

Table A3.2: Mercury Retraction Data for RUN 1.

P(psig)	Volume Reading (cm^3)	V_{corr}^* cm^3	Volume of Hg in sample cm^3	S_{nw}
850	0.46	4.5	4.2650005	1.000000117
725	0.411666	4.55	4.26333425	0.999609437
598	0.362559	4.6	4.26244134	0.99940008
500	0.324665	4.65	4.250335	0.996561547
425	0.295665	4.7	4.22933525	0.991637808
362	0.271305	4.75	4.20369546	0.985626134
320	0.255064	4.8	4.1699356	0.977710574
280	0.239598	4.85	4.1354024	0.969613693
250	0.227998	4.9	4.0970025	0.960610199
230	0.220264	4.95	4.0547359	0.950700094
210	0.212531	5	4.0124693	0.940789988
190	0.204797	5.05	3.9702027	0.930879883
172	0.197837	5.1	3.92716276	0.920788455
160	0.193197	5.15	3.8818028	0.91015306
140	0.185464	5.2	3.8395362	0.900242954
130	0.181597	5.255	3.7884029	0.888253904
122	0.178504	5.3	3.74649626	0.878428197
110	0.173864	5.35	3.7011363	0.867792802
103	0.171157	5.4	3.65384299	0.856704101
92	0.16376	5.45	3.61124	0.846715123
85	0.15725	5.5	3.56775	0.836518171
80	0.152	5.55	3.523	0.826025791
70	0.14	5.6	3.485	0.817116061
68	0.13736	5.65	3.43764	0.806011723
65	0.13325	5.7	3.39175	0.795252052
62	0.12896	5.75	3.34604	0.784534584
58	0.12296	5.8	3.30204	0.774218054
53	0.11501	5.85	3.25999	0.764358734
50	0.11	5.9	3.215	0.753810082
48	0.10656	5.95	3.16844	0.742893318
40	0.092	6	3.133	0.734583822
38	0.08816	6.05	3.08684	0.723760844
32	0.07616	6.1	3.04884	0.714851114
30	0.072	6.15	3.003	0.704103165
28	0.06776	6.2	2.95724	0.693373974
25	0.06125	6.25	2.91375	0.683177022
20	0.05	6.3	2.875	0.674091442

RUN 2

Vol reading of empty pycnometer (V_{em})= 48.87 cm^3
Vol reading of full pycnometer ($V_{full,1}$) @ atm= 1.28 cm^3
Vol of pycnometer (V_{pyc})= 47.59 cm^3
Vol reading of full pycnometer (V_{full}) @ 850 psig= 0.94 cm^3
Volume expansion of pycnometer = 0.34 cm^3
Volume reading with core @ atm= 6.57 cm^3
Bulk volume of sample = 5.29 cm^3

POROSITY Calculation

Vol at reading with Hg in the sample @850psig= 2.955 cm^3
Porosity = 0.619093
Pore vol = 3.275 cm^3

Mercury Intrusion Data/ Calculations

Table A3.3: Mercury Intrusion Data for RUN 2.

P(psig)	Volume Reading (cm^3)	V_{corr}^* cm^3	Volume of Hg in sample cm^3	S_{nw}
0	6.57	0	0	0
22	6.5	0.05456	0.01544	0.004715
63	6.4	0.13041	0.03959	0.012089
138	6.3	0.17861005	0.091389954	0.027905
148	6.2	0.18087672	0.189123284	0.057748
160	6.1	0.18359672	0.28640328	0.087451
168	6	0.18541006	0.384589944	0.117432
177	5.9	0.18745006	0.482549941	0.147343
185	5.8	0.1892634	0.580736605	0.177324
193	5.7	0.19107673	0.678923269	0.207305
203	5.6	0.1933434	0.776656599	0.237147
225	5.5	0.19833008	0.871669925	0.266159
238	5.4	0.20127675	0.968723254	0.295793
253	5.3	0.20467675	1.065323249	0.32529
260	5.2	0.20626342	1.16373658	0.355339
272	5.1	0.20898342	1.261016576	0.385043
290	5	0.21306343	1.35693657	0.414332
305	4.895	0.21646344	1.458536565	0.445355
315	4.8	0.21873011	1.551269895	0.47367
332	4.7	0.22258344	1.647416556	0.503028
345	4.6	0.22553012	1.744469885	0.532663
358	4.5	0.22847679	1.841523214	0.562297
370	4.4	0.23119679	1.93880321	0.592001
391	4.295	0.2359568	2.039043203	0.622609
402	4.2	0.23845013	2.131549866	0.650855
412	4.1	0.2407168	2.229283196	0.680697
438	4	0.24661015	2.323389854	0.709432
450	3.9	0.24933015	2.42066985	0.739136
482	3.8	0.25658349	2.513416506	0.767455
515	3.7	0.26406351	2.605936495	0.795706
530	3.595	0.26746351	2.70753649	0.826729
575	3.5	0.27766353	2.792336475	0.852622
650	3.3	0.29466355	2.97533645	0.9085
720	3.2	0.31053024	3.05946976	0.934189
780	3.1	0.32413026	3.14586974	0.960571
850	2.955	0.33999695	3.27500305	1.000001

Mercury Retraction Data/ Calculations

Table A3.4: Mercury Retraction Data for RUN 2.

P(psig)	Volume Reading (cm^3)	V$_{corr}$* cm^3	Volume of Hg in sample cm^3	S$_{nw}$
850	0.339997	2.955	3.27500305	1.000001
755	0.318464	3	3.251536415	0.992836
630	0.29013	3.05	3.22986979	0.98622
525	0.26633	3.1	3.203669825	0.97822
440	0.247063	3.15	3.17293652	0.968836
380	0.233463	3.2	3.13653654	0.957721
335	0.223263	3.25	3.096736555	0.945568
295	0.214197	3.3	3.055803235	0.93307
265	0.207397	3.35	3.012603245	0.919879
240	0.20173	3.4	2.96826992	0.906342
215	0.196063	3.45	2.923936595	0.892805
195	0.19153	3.5	2.878469935	0.878922
180	0.18813	3.55	2.83186994	0.864693
163	0.184277	3.6	2.785723279	0.850603
150	0.18133	3.65	2.73866995	0.836235
138	0.17861	3.71	2.681389954	0.818745
130	0.176797	3.75	2.64320329	0.807085
120	0.17453	3.8	2.59546996	0.79251
110	0.172263	3.85	2.54773663	0.777935
102	0.17045	3.9	2.499549966	0.763221
88	0.16016	3.95	2.45984	0.751096
82	0.15416	4	2.41584	0.737661
70	0.14	4.1	2.33	0.71145
65	0.13325	4.15	2.28675	0.698244
62	0.12896	4.2	2.24104	0.684287
60	0.126	4.25	2.194	0.669924
58	0.12296	4.3	2.14704	0.655585
50	0.11	4.35	2.11	0.644275
43	0.09761	4.45	2.02239	0.617524
38	0.08816	4.55	1.93184	0.589875
32	0.07616	4.65	1.84384	0.563005
22	0.05456	4.75	1.76544	0.539066
22	0.05456	4.85	1.66544	0.508531
20	0.05	4.95	1.57	0.479389

- ***Calibration of pycnometer with press for volume correction***

Table A3.5: Pycnometer Volume Correction Calibration Data.

P (psig)	ΔV ($V_{0,atm}$-V_{curr})	Vol reading (cm^3)
0	0	11.43
50	0.11	11.32
100	0.17	11.26
150	0.19	11.24
200	0.21	11.22
250	0.22	11.21
300	0.235	11.195
400	0.255	11.175
450	0.27	11.16
550	0.295	11.135
600	0.31	11.12
670	0.325	11.105
750	0.345	11.085
800	0.36	11.07
850	0.37	11.06

where $V_{0,atm}$ is volume reading at zero gauge pressure inside the pycnometer and V_{curr} is the volume reading at current pressure in the pycnometer.

This pressure versus volume change data was fit to two curves one valid up to 100 psig pressure and another above 100 psig as shown in the Figs A3.1 and A3.2.

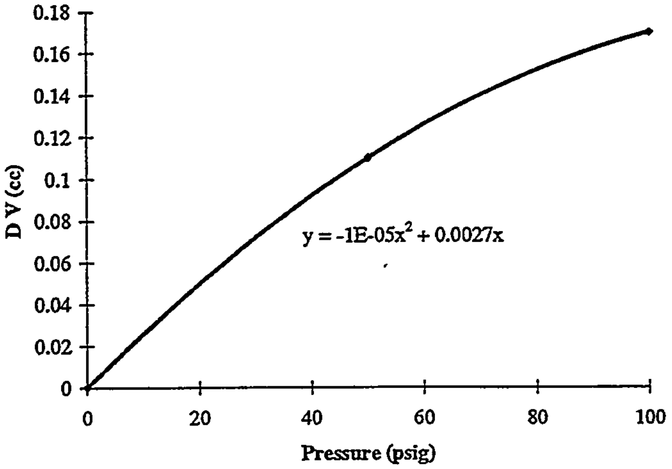

Figure A3.1: Pressure versus volume correction relation up to 100 psig.

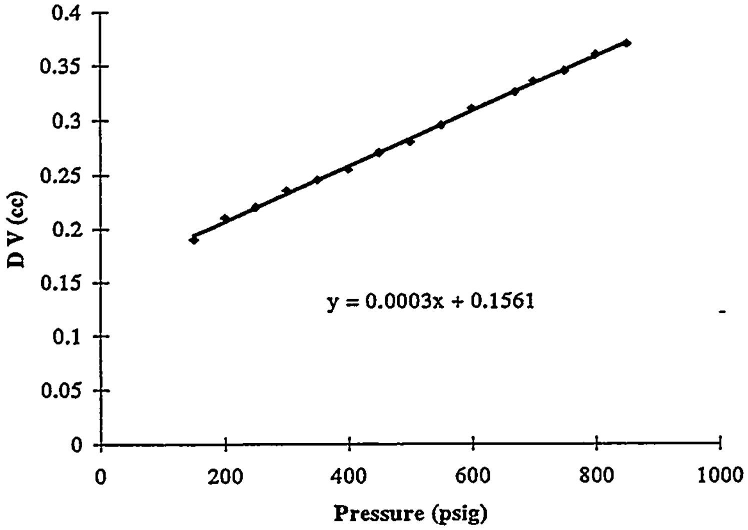

Figure A3.2: Pressure versus volume correction relation above 100 psig.

Appendix IV

Permeability Measurement Data

SAMPLE 1

Length =	1 inch =	2.54 cm
Diameter =	1 inch =	2.54 cm

X-area (cm^2) = 5.066119

P(avg.) Atm.	Flow (cm^3/min)	K_a(mD)
0.25	0.27	9.635088
0.5	0.53	9.45666
1	0.96	8.564523

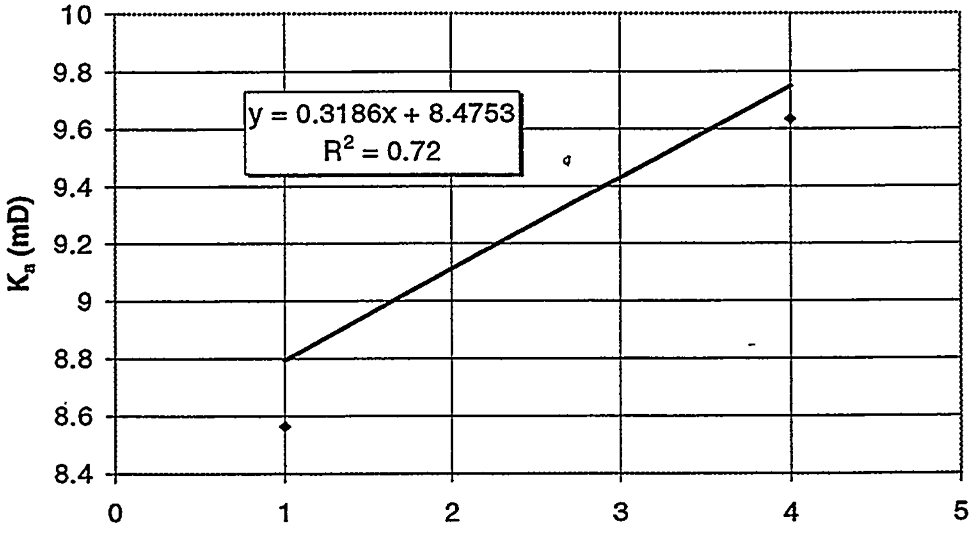

Figure A4.1: Absolute permeability correction of Sample 1 for Klinkenberg effect.

SAMPLE 2

Length = 1.06 inch = 2.6924 cm
Diameter = 1.015 inch = 2.5781 cm

X-area (cm^2) = 5.219242

P(avg) Atm	Flow (cm^3/min)	K_a(mD)
0.25	0.24	8.81205
0.5	0.44	8.077712
1	0.74	6.792622

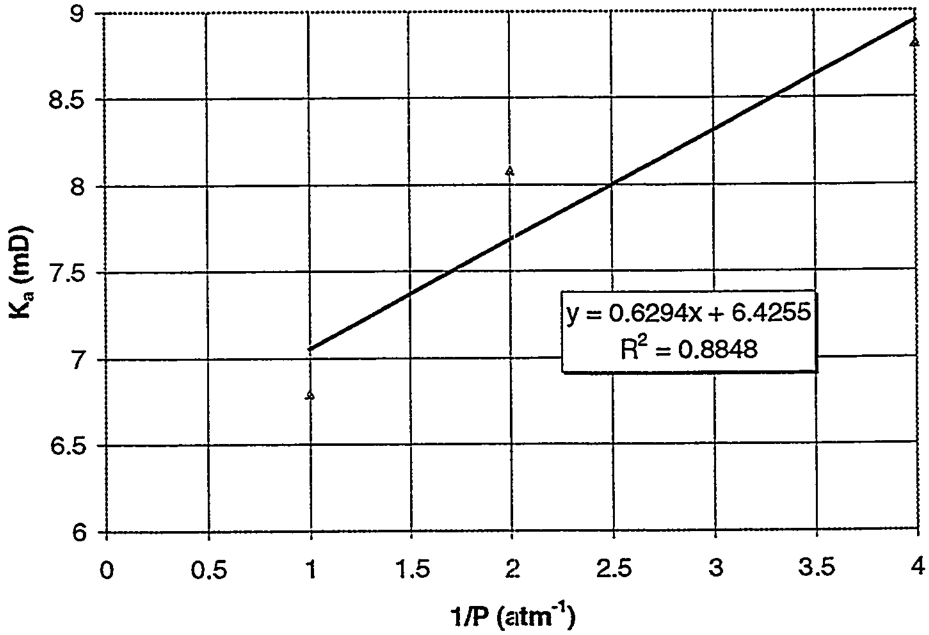

Figure A4.2: Absolute permeability correction of Sample 2 for Klinkenberg effect.

SAMPLE 3

Length = 0.68 inch = 1.7272 cm
Diameter = 1 inch = 2.54 cm

X-area (cm^2) = 5.066119

P(avg) Atm	Flow (cm^3/min)	K_a(mD)
0.25	0.4	9.706459
0.5	0.76	9.221136
1	1.45	8.796478

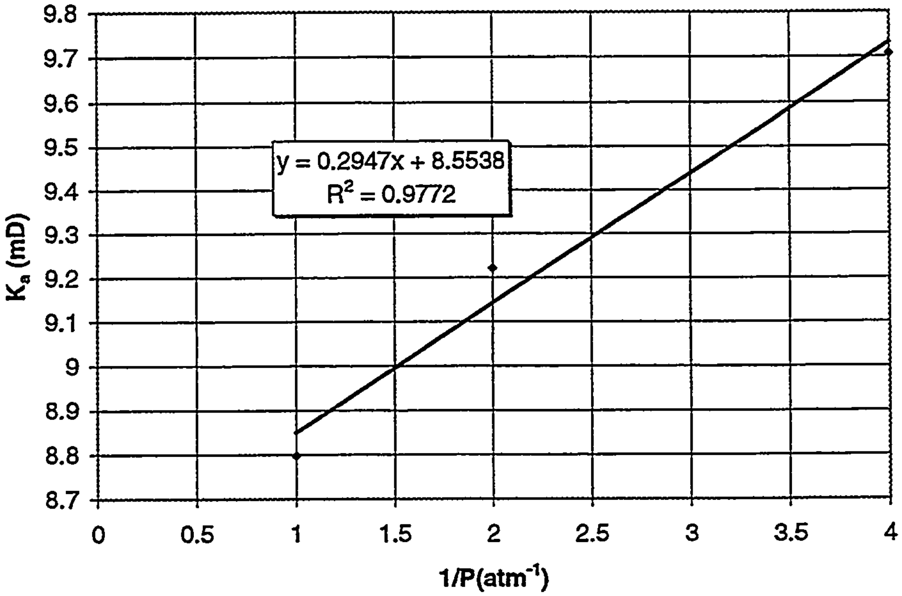

Figure A4.3: Absolute permeability correction of Sample 3 for Klinkenberg effect.

SAMPLE 4

Length = 0.85 inch = 2.159 cm
Diameter = 1 inch = 2.54 cm

X-area (cm^2)= 5.066119

P(avg) Atm	Flow (cm^3/min)	K_a(mD)
0.25	0.34	10.31311
0.5	0.64	9.706459
1	1.2	9.099805

Figure A4.4: Absolute permeability correction of Sample 4 for Klinkenberg effect.

Appendix V

Single-Pore Conductivity Calculations

The equation describing the constriction of a pore is given by,

$$\frac{R}{R_b}=\lambda=1-\frac{1-\lambda_t}{2}\left[1+Cos\left(\frac{2\pi x}{\xi R_b}\right)\right] \tag{A5.1}$$

where $\lambda_t=\frac{R_T}{R_b}$ is the aspect ratio of the pore, and $\xi=\frac{L}{R_b}$ is the dimensionless length of a single pore, R_b is the pore body size, R_t the pore throat size and L the length of a single pore.

We assume that at the pore-level flow is creeping flow, *i.e.,* the Hagen-Poisuelle equation for single-phase flow can be applied. This flow equation in differential form for a circular cross section is,

$$Q=\frac{\pi R^4}{8\mu}\frac{dp}{dx} \tag{A5.2}$$

where Q is the flow though the cross section, R is the radius of the cross section, μ is the viscosity of flowing fluid and *dp/dx* is the pressure gradient in the flow direction x. This equation is valid for Reynold number $R_e < 2100$. It is integrated over the entire pore length to find the pressure drop in the single pore in the following manner:

$$\Delta p_L=\frac{8\mu Q}{\pi}\int_{-\frac{L}{2}}^{\frac{L}{2}}\frac{dx}{R^4} \tag{A5.3}$$

Let $I = \int_{-\frac{l}{2}}^{\frac{l}{2}} \frac{dx}{R^4}$, and substituting Eq. A1.1 for R, we have,

$$I = \int_{-\xi R_b/2}^{\xi R_b/2} \frac{dx}{R_b^4 \left[1 - \left(\frac{1-\lambda_t}{2}\right)\left(1 + Cos\left(\frac{2\pi x}{\xi R_b}\right)\right)\right]^4}$$

Now if we make the substitution, $\theta = \frac{2\pi x}{\xi R_b}$ and $\alpha = \frac{1-\lambda_t}{2}$ we get the following integral

$$I = \frac{\xi}{2\pi R_b^3} \int_{-\pi}^{\pi} \frac{d\theta}{\left[1 - \alpha - \alpha Cos\theta\right]^4}$$

as the function being integrated is an even function,

$$I = \frac{\xi}{\pi R_b^3} \int_{0}^{\pi} \frac{d\theta}{\left(1 - \alpha - \alpha Cos\theta\right)^4}$$

Further, if we make the substitution $Z = \tan\frac{\theta}{2}$ we have $Cos\theta = \frac{1-Z^2}{1+Z^2}$ and $d\theta = \frac{2dZ}{1+Z^2}$ the integral becomes,

$$I = \frac{2\xi}{\pi R_b^3} \int_{0}^{\infty} \frac{dZ}{\left(1+Z^2\right)\left[1 - \alpha - \alpha\frac{1-Z^2}{1+Z^2}\right]^4}$$

or

$$I = \frac{2\xi}{\pi R_b^3} \int_{0}^{\infty} \frac{\left(1+Z^2\right)^3 dZ}{\left[(1-\alpha)\left(1+Z^2\right) - \alpha\left(1-Z^2\right)\right]^4}$$

or

$$I=\frac{2\xi}{\pi R_b^3}\int_0^\infty\frac{\left(1+Z^2\right)^3dZ}{\left[1-2\alpha+Z^2\right]^4}=\frac{2\xi}{\pi R_b^3}\int_0^\infty\frac{\left(1+Z^2\right)^3dZ}{\left(\lambda_t+Z^2\right)^4} \qquad \text{(A5.4)}$$

To solve the integral of Eq. A5.4, we use the method of partial fractions as indicated below,

$$\frac{\left(1+Z^2\right)^3}{\left(\lambda_t+Z^2\right)^4}\equiv\frac{A_1Z+B_1}{\lambda_t+Z^2}+\frac{A_2Z+B_2}{\left(\lambda_t+Z^2\right)^2}+\frac{A_3Z+B_3}{\left(\lambda_t+Z^2\right)^3}+\frac{A_4Z+B_4}{\left(\lambda_t+Z^2\right)^4}$$

or

$$\begin{aligned}Z^6+3Z^4+3Z^2+1\equiv{}&\left(A_1Z+B_1\right)\left(\lambda_t+Z^2\right)^3+\left(A_2Z+B_2\right)\left(\lambda_t+Z^2\right)^2\\&+\left(A_3Z+B_3\right)\left(\lambda_t+Z^2\right)+A_4Z+B_4\end{aligned}$$

Comparing coefficients of equal powers of Z on the both sides of the identity we get the values below,

$$\begin{aligned}A_1&=0 & A_2&=0\\ B_1&=1 & B_2&=3\left(1-\lambda_t\right)\\ A_3&=0 & A_4&=0\\ B_3&=3\left(1-\lambda_t\right)^2 & B_4&=\left(1-\lambda_t\right)^3\end{aligned}$$

Based on these partial fractions the integral I can be broken into four separate integrals as given below,

$$I=\frac{2\xi}{\pi R_b^3}\left(I_1+I_2+I_3+I_4\right) \qquad \text{(A5.5)}$$

where ,

$$I_1=\int_0^\infty \frac{dZ}{\lambda_t+Z^2} \qquad I_2=3(1-\lambda_t)\int_0^\infty \frac{dZ}{\left(\lambda_t+Z^2\right)^2}$$

$$I_3=3(1-\lambda_t)^2\int_0^\infty \frac{dZ}{\left(\lambda_t+Z^2\right)^3} \qquad I_4=(1-\lambda_t)^3\int_0^\infty \frac{dZ}{\left(\lambda_t+Z^2\right)^4}$$

Calculation of I_1:

$$I_1=\int_0^\infty \frac{dZ}{\lambda_t+Z^2}=\frac{1}{\sqrt{\lambda_t}}\tan^{-1}\left(\frac{Z}{\sqrt{\lambda_t}}\right)\Bigg|_0^\infty=\frac{\pi}{2\sqrt{\lambda_t}} \qquad \text{(A5.6)}$$

Calculation of I_2, I_3, I_4:

Let us define

$$I_n=\int_0^\infty \frac{dZ}{\left(\lambda_t+Z^2\right)^n} \qquad \text{where n = 2,3,4 ;}$$

If we make the substitution of $Z=\sqrt{\lambda_t}\tan\theta$, the integral becomes,

$$I_n=\frac{1}{\lambda_t^{n-1/2}}\int_0^{\pi/2}(Cos\theta)^{2(n-1)}d\theta \qquad \text{(A5.7)}$$

The integral part of Eq. A5.7 is a standard integral and we read it from the table of integrals (*CRC mathematical handbook*, 1957).

For I_2, n=2 and $2(n-1)$=2 and,

$$\int Cos^2\theta \quad d\theta=\frac{1}{4}Sin2\theta+\frac{\theta}{2}$$

For I_3, $n=3$ and $2(n-1)=4$ and,

$$\int Cos^4\theta \quad d\theta = \frac{1}{4}Cos^3\theta \quad Sin\theta + \frac{3}{8}Sin\theta \quad Cos\theta + \frac{3}{8}\theta$$

For I_4, $n=4$ and $2(n-1)=6$ and,

$$\int Cos^6\theta \quad d\theta = \frac{1}{6}Sin\theta \quad Cos^5\theta + \frac{5}{24}Sin\theta \quad Cos^3\theta + \frac{5}{16}Cos\theta \quad Sin\theta + \frac{5}{16}\theta$$

Thus,

$$I_2 = \frac{3(1-\lambda_t)}{\lambda_t^{3/2}}\left[\frac{1}{4}Sin2\theta + \frac{\theta}{2}\right]_0^{\pi/2} = \frac{3\pi(1-\lambda_t)}{4\lambda_t^{3/2}}$$

$$I_3 = \frac{3(1-\lambda_t)^2}{\lambda_t^{5/2}}\left[\frac{1}{4}Cos^3\theta \quad Sin\theta + \frac{3}{8}Sin\theta \quad Cos\theta + \frac{3}{8}\theta\right]_0^{\pi/2} = \frac{9\pi(1-\lambda_t)^2}{16\lambda_t^{5/2}}$$

$$I_4 = \frac{(1-\lambda_t)^3}{\lambda_t^{7/2}}\left[\frac{1}{6}Sin\theta \quad Cos^5\theta + \frac{5}{24}Sin\theta \quad Cos^3\theta + \frac{5}{16}Cos\theta \quad Sin\theta + \frac{5}{16}\theta\right]_0^{\pi/2} = \frac{5\pi(1-\lambda_t)^3}{16\lambda_t^{7/2}}$$

Using these values of I_1, I_2, I_3 and I_4 in Eq.(A5.5) we have,

$$I = \frac{2\xi}{\pi R_b^3}\left[\frac{\pi}{2\lambda_t^{1/2}} + \frac{3\pi(1-\lambda_t)}{4\lambda_t^{3/2}} + \frac{9\pi(1-\lambda_t)^2}{16\lambda_t^{5/2}} + \frac{5\pi(1-\lambda_t)^3}{16\lambda_t^{7/2}}\right]$$

or

$$I = \frac{\xi}{R_b^3\sqrt{\lambda_t}}\frac{9\lambda_t^2 - 6\lambda_t + 5}{8\lambda_t^3} \qquad \text{(A5.8)}$$

Combining Eqs. A1. 8 and A1.3 we get,

$$\Delta p_L = \frac{8\mu Q}{\pi}\frac{\xi}{R_b^3\sqrt{\lambda_t}}\frac{9\lambda_t^2-6\lambda_t+5}{8\lambda_t^3} \tag{A5.9}$$

This equation gives the pressure drop per wavelength of a sinusoidal pore in the case of single-phase flow.

If we define dimensionless conductivity associated with a pore as,

$$g = \frac{QL}{\Delta p_L}\frac{8\mu}{\pi R_c^4} \tag{A5.10}$$

where R_c is some characteristic dimension used to render the distribution of sizes in g dimensionless, we can define dimensionless conductivity of the single pore as ,

$$g(R_b, R_t) = \frac{8R_b^4\sqrt{\lambda_t}}{R_c^4\left(9\lambda_t^2-6\lambda_t+5\right)} \tag{A5.11}$$

If we define dimensionless body and throat dimensions of the pore as

$r_b = \frac{R_b}{R_c}$ and $r_t = \frac{R_t}{R_c}$ then dimensionless conductivity can be written as,

$$g(r_t, \lambda_t) = \frac{8r_t^4}{\sqrt{\lambda_t}\left(9\lambda_t^2-6\lambda_t+5\right)} \tag{A5.12}$$

This is the single-pore conductivity equation that is used in network calculations of this report.

Appendix VI

Single-Pore Volume Calculations

The equation describing the constriction of a pore is,

$$\frac{R}{R_b} = \lambda = 1 - \frac{1-\lambda_t}{2}\left[1 + Cos\left(\frac{2\pi x}{\xi R_b}\right)\right] \tag{A6.1}$$

where $\lambda_t = \frac{R_T}{R_b}$ is the aspect ratio, and $\xi = \frac{L}{R_b}$ is the dimensionless length, R_b is the pore-body size, R_t the pore-throat size, and L the wavelength of the single pore. The volume per wavelength of a single pore is found by,

$$V_L = \int_{-\frac{L}{2}}^{\frac{L}{2}} \pi R^2 dx \tag{A6.2}$$

Substituting Eq. A6.1 for R in Eq. A2.2 we have,

$$V_L = \int_{-\xi R_b/2}^{\xi R_b/2} \pi R_b^2 \left[1 - \left(\frac{1-\lambda_t}{2}\right)\left(1 + Cos\left(\frac{2\pi x}{\xi R_b}\right)\right)\right]^2 dx$$

Now we make the substitution, $\theta = \frac{2\pi x}{\xi R_b}$, $\alpha = \frac{1-\lambda_t}{2}$ and obtain the following integral

$$V_L = \frac{1}{2}\xi R_b^3 \int_{-\pi}^{\pi} [1 - \alpha - \alpha Cos\theta]^2 d\theta$$

since the function being integrated is an even function,

$$V_L = \xi R_b^3 \int_0^{\pi} [1-\alpha-\alpha Cos\theta]^2 \, d\theta$$

or,

$$V_L = \xi R_b^3 \int_0^{\pi} \left[(1-\alpha)^2 - 2\alpha(1-\alpha)Cos\theta + \alpha^2 Cos^2\theta\right] d\theta \tag{A6.3}$$

From the table of integrals (*CRC mathematical handbook*[1]) we know that,

$$\int Cos^2\theta \quad d\theta = \frac{1}{4} Sin 2\theta + \frac{\theta}{2}$$

$$\int Cos\theta \quad d\theta = Sin\theta$$

Using these results in Eq. (A6.3) we get ,

$$V_L = \xi R_b^3 \left[(1-\alpha)^2 \theta - 2\alpha(1-\alpha) Sin\theta + \alpha^2 \left(\frac{1}{4} Sin 2\theta + \frac{\theta}{2}\right)\right]_0^{\pi} = \frac{\xi \pi R_b^3}{2}\left[2(1-\alpha)^2 + \alpha^2\right]$$

Putting back $\alpha = \dfrac{1-\lambda_t}{2}$ in the expression, after simplification we obtain,

$$V_L = \frac{\pi \xi R_b^3}{8}\left(3\lambda_t^2 + 2\lambda_t + 3\right) \tag{A6.4}$$

The pore volume per unit length is thus,

$$V = \frac{\pi R_b^2}{8}\left(3\lambda_t^2 + 2\lambda_t + 3\right) \tag{A6.5}$$

If we define dimensionless volume per unit length associated with a pore as,

$$v = \frac{V}{R_c^2} \tag{A2.6}$$

where R_c is some characteristic dimension used to render V dimensionless, we can define dimensionless volume of the single pore as ,

$$v(r_b,\lambda_t)=\frac{\pi r_b^2}{8}\left(3\lambda_t^2+2\lambda_t+3\right) \tag{A6.7}$$

where $r_b=\dfrac{R_b}{R_c}$ and $r_t=\dfrac{R_t}{R_c}$ are dimensionless pore-body and throat-sizes, respectively.

This is the single pore volume equation that is used in network calculations of this report.

Appendix VII

Single-Pore Uniform Deposition Calculations

Let δT be the thickness of the deposited layer along the pore walls. The new pore dimensions at the end of this deposition step are

$$R_{b,new} = R_b - \delta T \tag{A7.1}$$

$$R_{t,new} = R_t - \delta T \tag{A7.2}$$

From Appendix VI Eq. A6.5, we already know that the volume of a single pore per unit length is,

$$V = \frac{\pi R_b^2}{8}\left(3\lambda_t^2 + 2\lambda_t + 3\right) \tag{A6.5}$$

This equation is rewritten as,

$$V = \frac{\pi}{8}\left(3R_t^2 + 2R_t R_b + 3R_b^2\right) \tag{A7.3}$$

Using Eqs. A7.1 and A7.2 in Eq. A7.3 we can find the volume deposited as,

$$\delta V = V_{old} - V_{new} = \frac{\pi}{8}\left[3R_t^2 + 2R_t R_b + 3R_b^2 - 3(R_t - \delta T)^2 - 2(R_t - \delta T)(R_b - \delta T) - 3(R_b - \delta T)^2\right]$$

...(A7.4)

On expanding the terms of Eq. A3.4 and simplifying we get,

$$\delta V = \pi \delta T(R_b + R_t - \delta T) \tag{A7.5}$$

To find the dimensionless volume deposited per unit pore-length we again define,

$$\delta v=\frac{\delta V}{R_c^2} \tag{A7.6}$$

Thus, effective dimensionless amount deposited is,

$$\delta v=\pi\delta t\left(r_b+r_t-\delta t\right) \tag{A6.7}$$

where,

$$\delta t=\frac{\delta T}{R_c} \tag{A6.8}$$

This is the deposition equation that we use in network calculations for the uniform deposition case.

Appendix VIII

Series Approximations Used in Network Calculations

Effective Conductivity Approximation

For a Bethe lattice of coordination number Z, the effective conductivity for the bond percolation problem is,

$$G_{eff} = -ZC'(0) \tag{A8.1}$$

where $C'(0)$ is the value of first derivative of C(x) evaluated at zero, and C(x) is called the generating function. This generating function satisfies the following recursive integral equation in Laplace space (Stinchcombe, 1974).

$$\int_0^\infty e^{-tx}C(x)dx = \frac{1-f}{t} + f\int_0^\infty G(g)\left\{\frac{1+t}{g} + \frac{g^2}{(t+g)^2}\int_0^\infty \exp\left(\frac{x-g}{g+t}\right)C(x)^{Z-1}dx\right\}dg \tag{A8.2}$$

A series approximation to find $C'(0)$ is Heiba (1984).

$$0 = 1 - Q_j\int_0^\infty G(g)dg\sum_{k=1}^{z-1}\left[C_k^{z-1}(1-s)^{z-1-k}s^k\frac{kg}{gs+kC'(0)} - a_2\frac{kg^2C'(0)}{\{gs+kC'(0)\}^3}\right] \tag{A8.3}$$

where C^{z-1}_k is the kth binomial coefficient. The coefficient a_2 is given by the following expression,

$$a_2 = s - Q_j + Q_j\int_0^\infty G(g)dg\sum_{k=0}^{z-1}\left[C_k^{z-1}(1-s)^{z-1-k}s^k\left\{1-\frac{kgs}{gs-kC'(0)}\right\}^2\right] \tag{A8.4}$$

The s used in these equations is the root of

$$s - Q_j + Q_j(1-s)^{Z-1} = 0, \quad \text{where, } 0 < s \leq 1 \tag{A8.5}$$

Larson and Davis Approximation for Accessibility Function

The expression that is used to find the accessible fraction of a Bethe lattice at any stage of deposition has been calculated analytically by Essam & Fischer (1961) to be,

$$X^A = \begin{cases} f\left[1 - \left(\dfrac{f^*}{f}\right)^{2Z-2/Z-2}\right] & ; f \geq f_c \\ 0 & ; f < f_c \end{cases} \tag{A8.9}$$

where f is the fraction of open bonds in the network and f_c is the percolation threshold. The value of f^* is root of the following equation,

$$f^*(1-f^*)^{Z-2} - f(1-f)^{Z-2} = 0 \tag{A8.10}$$

such that $f^* \to 0$ as $f \to 0$ or $f \to 1$. The series approximation to this system of equations is given by Larson & Davis (1982) ,

$$X^A = f\{1 - R^{2(Z-1)}\} \tag{A8.11}$$

with R being the root of

$$\sum_{i=2}^{Z-1} R^{Z-i} + \frac{f-1}{f} = 0 \tag{A8.12}$$

Appendix IX

Error Analysis Study of the Curve-Fitting Approach

This analysis was performed to investigate the amount of error that is introduced if we use the relations generated by curve fitting (Table 4.1) to predict permeability change instead of a full scale network model. The aim, is to see how good the power-law model is in the deposition ranges concerned. The approach used for this analysis is:

- Permeability change versus porosity change data is generated by the network model. This data is taken as the reference.
- Depending on the pore-evolution mechanism, a relation from Table 4.1 is used to predict the permeability change for the porosity changes of the reference data.
- The 0-10% deposition range is divided into separate intervals, and the deviation between network model results and correlation results investigated.

Parameters Used in the Study

This appendix shows the detailed study done for a deposition case, considering that deposition is occurring at pore-throats only. The porous medium parameters considered are

i) Connectivity, $Z=3$

ii) Aspect ratio, $\lambda_t=6$.

Based on these parameters, the network model is used to predict the permeability change as a function of porosity change. The data obtained from the network calculations is listed in Table A9.1, and is used as the reference data.

Table A9.1: Reference data generated by the Network Model Calculations.

ϕ/ϕ_0	k/k_0	$\log \phi/\phi_0$	$\log k/k_0$
1	1	0	0
0.998925	0.977542	-0.00046712	-0.00986457
0.997726	0.954044	-0.00098871	-0.0204316
0.996418	0.930077	-0.00155844	-0.0314811
0.995012	0.905867	-0.00217168	-0.04293556
0.993517	0.881553	-0.0028247	-0.05475157
0.991942	0.857238	-0.00351372	-0.06689859
0.990292	0.833	-0.00423673	-0.079355
0.988574	0.808898	-0.00499082	-0.09210624
0.986792	0.784986	-0.00577438	-0.10513809
0.983053	0.73789	-0.00742307	-0.13200838
0.981103	0.714771	-0.0082854	-0.14583308
0.979104	0.691975	-0.00917118	-0.1599096
0.977059	0.669524	-0.01007921	-0.17423385
0.97497	0.647435	-0.01100875	-0.18880383
0.970669	0.604412	-0.01292884	-0.21866692
0.968461	0.583502	-0.01391786	-0.23395765
0.966218	0.563008	-0.01492488	-0.24948543
0.963942	0.542937	-0.0159491	-0.26525056
0.961632	0.523295	-0.01699109	-0.28125341
0.959292	0.504089	-0.01804918	-0.29749278
0.956923	0.485321	-0.01912301	-0.31397092
0.954526	0.466995	-0.02021224	-0.33068777
0.952102	0.44911	-0.02131652	-0.34764727
0.949652	0.43168	-0.02243551	-0.36483807
0.947178	0.414684	-0.0235684	-0.38228272
0.944681	0.398134	-0.02471482	-0.39997073
0.942161	0.382026	-0.02587488	-0.41790708
0.93962	0.36636	-0.02704775	-0.43609195
0.937058	0.351131	-0.02823353	-0.45453083
0.934477	0.336333	-0.02943138	-0.47323052
0.931877	0.321976	-0.03064141	-0.4921765
0.929259	0.308036	-0.03186322	-0.51139852
0.926625	0.294521	-0.03309599	-0.53088373
0.923973	0.281424	-0.03434072	-0.55063887
0.921306	0.268739	-0.0355961	-0.5706693
0.918624	0.256461	-0.03686221	-0.59097867
0.913218	0.233099	-0.03942554	-0.63245959
0.910495	0.222004	-0.04072243	-0.6536392
0.90776	0.21129	-0.04202896	-0.67512106

In the next step based on the values of parameters Z and λ_t and the relations read from Table 4.1 for the pore-throat deposition case, the power law coefficient is predicted for a 10% deposition range as follows,

$$\gamma = B(\lambda_t) + \frac{D(\lambda_t)}{Z - E(\lambda_t)} \tag{A9.1}$$

where,

$$B(\lambda_t) = -0.0311\lambda_t^2 + 0.5699\lambda_t + 2.8841 \tag{A9.2}$$

$$D(\lambda_t) = 0.0128\lambda_t^3 - 0.3715\lambda_t^2 - 3.876\lambda_t + 2.9961 \tag{A9.3}$$

$$E(\lambda_t) = -0.0185\lambda_t + 1.6878 \tag{A9.4}$$

The value obtained for γ is 16.169. This value of γ is used to predict permeability change given a porosity change, according to

$$\frac{k}{k_0} = \left(\frac{\phi}{\phi_0}\right)^{\gamma} \tag{A9.5}$$

The results of Eq. A9.5 are compared to permeability change values listed in Table A9.1. The values of permeability change predicted by both methods are listed in Table A9.2.

The comparison between these two data sets of permeability change is done graphically. The first comparison, shown in Fig. A9.1 for a deposition range of 10%, checks the validity of power-law model. This is done by trying to fit the $\log(\phi/\phi_o)$ versus $\log(k/k_0)$ data to two types of straight lines. One line passes through the origin and is the power-law relation. The other one is a best fit, which is not restricted to pass through the origin. From the results of this comparison, it is clear that using power-law over best fit under predicts the permeability changes. The maximum deviation is seen at very low deposition levels. Even in those regions the error is restricted to 5 % as indicated by the error bars.

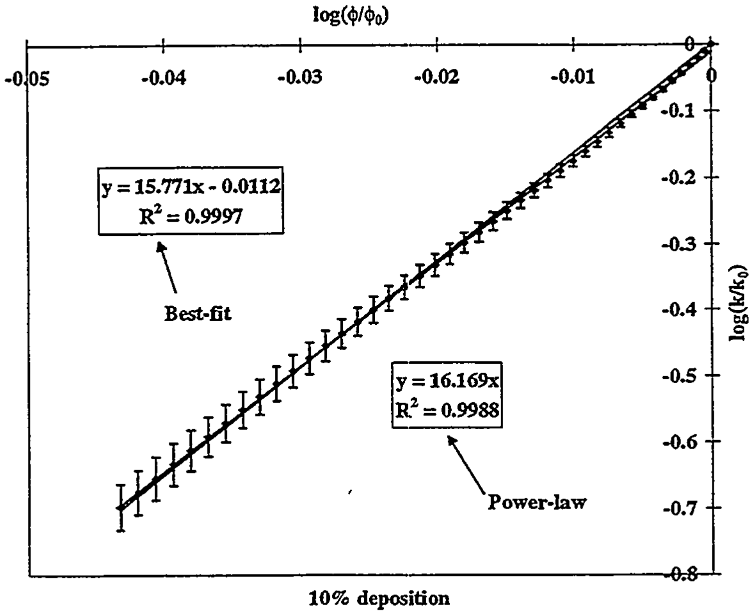

Figure A9.1: Power-law versus best-fit comparison with 5% error bars

The other aspect of the power-law relation that was studied was the range of its validity. The deposition range of 10% was subdivided into lower ranges and separate power-law models were fit to these smaller deposition ranges. The results of these smaller models were compared to the results of the power-law model derived values for 10% deposition, and the error introduced investigated. The smaller deposition ranges considered are 1%, 2.5%, 5% and 7.5%. The results obtained are indicated in Figs. A9.2-A9.5.

Based on these graphs we conclude that the error introduced as a result of using the same power law model for 0-10% deposition range causes larger error for low deposition cases compared to higher deposition cases. Although, this error value is high, of the order of 20% on the log-scale, it results in very small errors in absolute sense as the deposition range is only 1%. As a matter of fact, when we plot the k/k_0 versus ϕ/ϕ_0 on a simple arithmetic graph, the values obtained by using the power-law model and the network calculations are within 3% error.

Table A9.2: Comparison of Permeability Data Generated by the Use of Power-Law Model with the Network Model Results

$K/k_0^{(\text{ref. data})}$	$k/k_0^{*(\text{power-law})}$	$\text{Log } \phi/\phi_0$	$\text{Log } k/k_0^{*(\text{power-law})}$
1	1	0	0
0.977542	0.982759327	-0.00046712	-0.007552826
0.954044	0.963859082	-0.00098871	-0.015986456
0.930077	0.943629814	-0.00155844	-0.025198346
0.905867	0.92232946	-0.00217168	-0.035113919
0.881553	0.900176082	-0.0028247	-0.045672531
0.857238	0.877377814	-0.00351372	-0.056813352
0.833	0.854075616	-0.00423673	-0.068503677
0.808898	0.830430895	-0.00499082	-0.080696502
0.784986	0.806555114	-0.00577438	-0.093365951
0.73789	0.758536403	-0.00742307	-0.120023572
0.714771	0.734570405	-0.0082854	-0.133966573
0.691975	0.710740836	-0.00917118	-0.148288731
0.669524	0.687114709	-0.01007921	-0.162970754
0.647435	0.663742403	-0.01100875	-0.178000437
0.604412	0.617950353	-0.01292884	-0.209046416
0.583502	0.595610112	-0.01391786	-0.225037938
0.563008	0.573693167	-0.01492488	-0.241320323
0.542937	0.552228805	-0.0159491	-0.257880943
0.523295	0.531215837	-0.01699109	-0.274728986
0.504089	0.510696465	-0.01804918	-0.291837148
0.485321	0.490681972	-0.01912301	-0.309199898
0.466995	0.47118161	-0.02021224	-0.326811668
0.44911	0.452202696	-0.02131652	-0.344666853
0.43168	0.433750705	-0.02243551	-0.362759806
0.414684	0.41583647	-0.0235684	-0.381077424
0.398134	0.398461243	-0.02471482	-0.399613914
0.382026	0.381618231	-0.02587488	-0.418370886
0.36636	0.365312865	-0.02704775	-0.437335033
0.351131	0.34953615	-0.02823353	-0.456507902
0.336333	0.334290445	-0.02943138	-0.475876037
0.321976	0.319564912	-0.03064141	-0.495440912
0.308036	0.305353942	-0.03186322	-0.515196469
0.294521	0.291656049	-0.03309599	-0.535129012
0.281424	0.278448516	-0.03434072	-0.555255092
0.268739	0.26573371	-0.0355961	-0.575553349
0.256461	0.253498205	-0.03686221	-0.596025112
0.233099	0.230424415	-0.03942554	-0.637471507
0.222004	0.219562897	-0.04072243	-0.658441048
0.21129	0.209138397	-0.04202896	-0.679566224

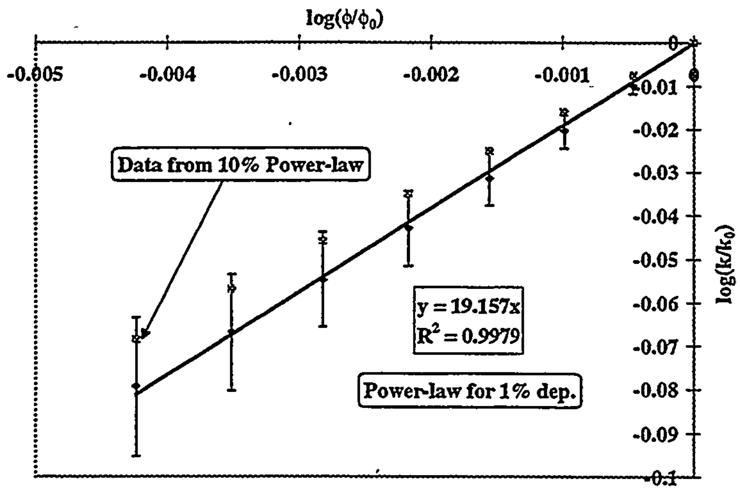

Figure A9.2: Power-law model for 1% deposition and 20% error bars

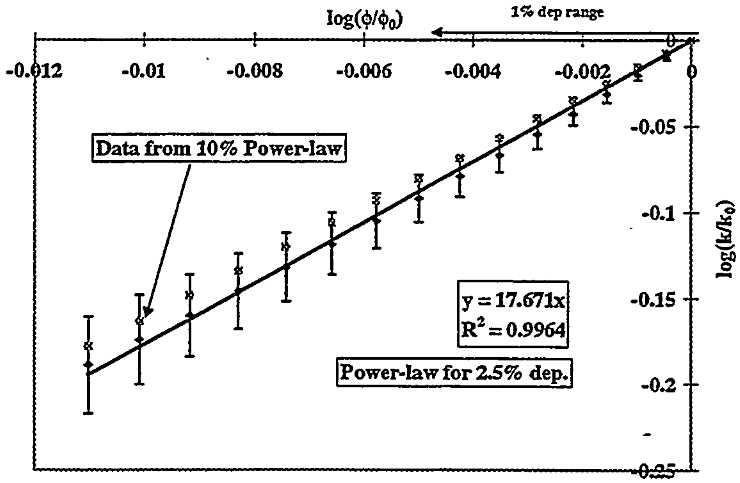

Figure A9.3: Power-law model for 2.5% deposition and 15% error bars

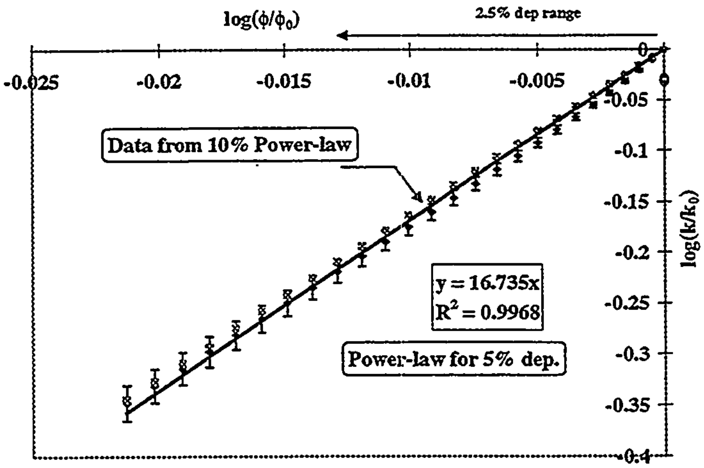

Figure A9.4: Power-law model for 5% deposition and 5% error bars

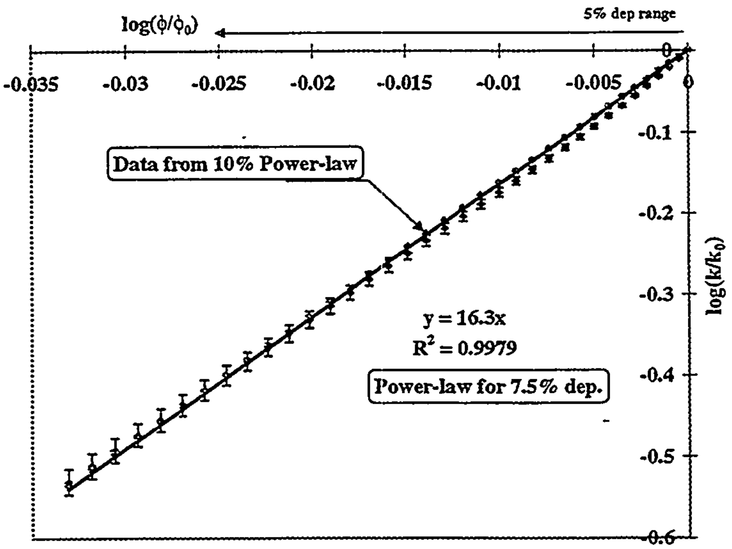

Figure A9.5: Power-law model for 7.5% deposition and 3% error bars

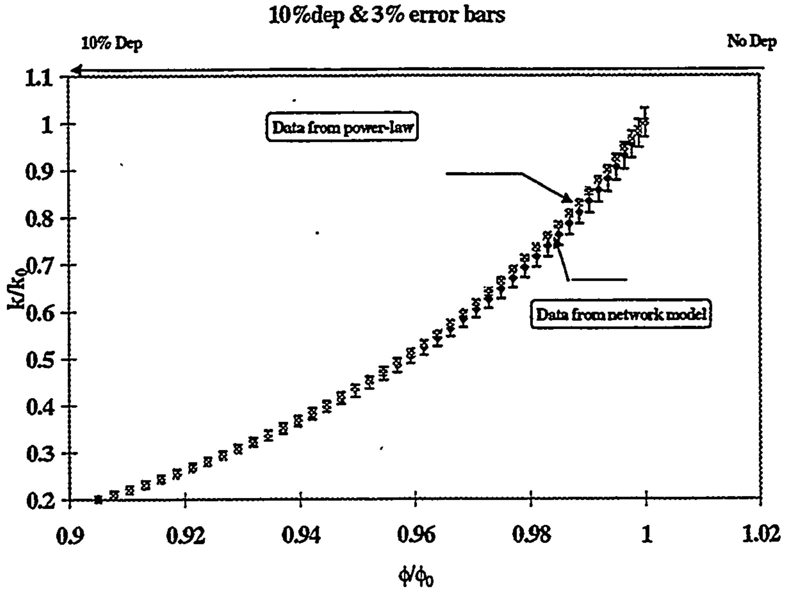

Figure A9.6: Comparison of power-law model and network model results with 3% error bars

Appendix X

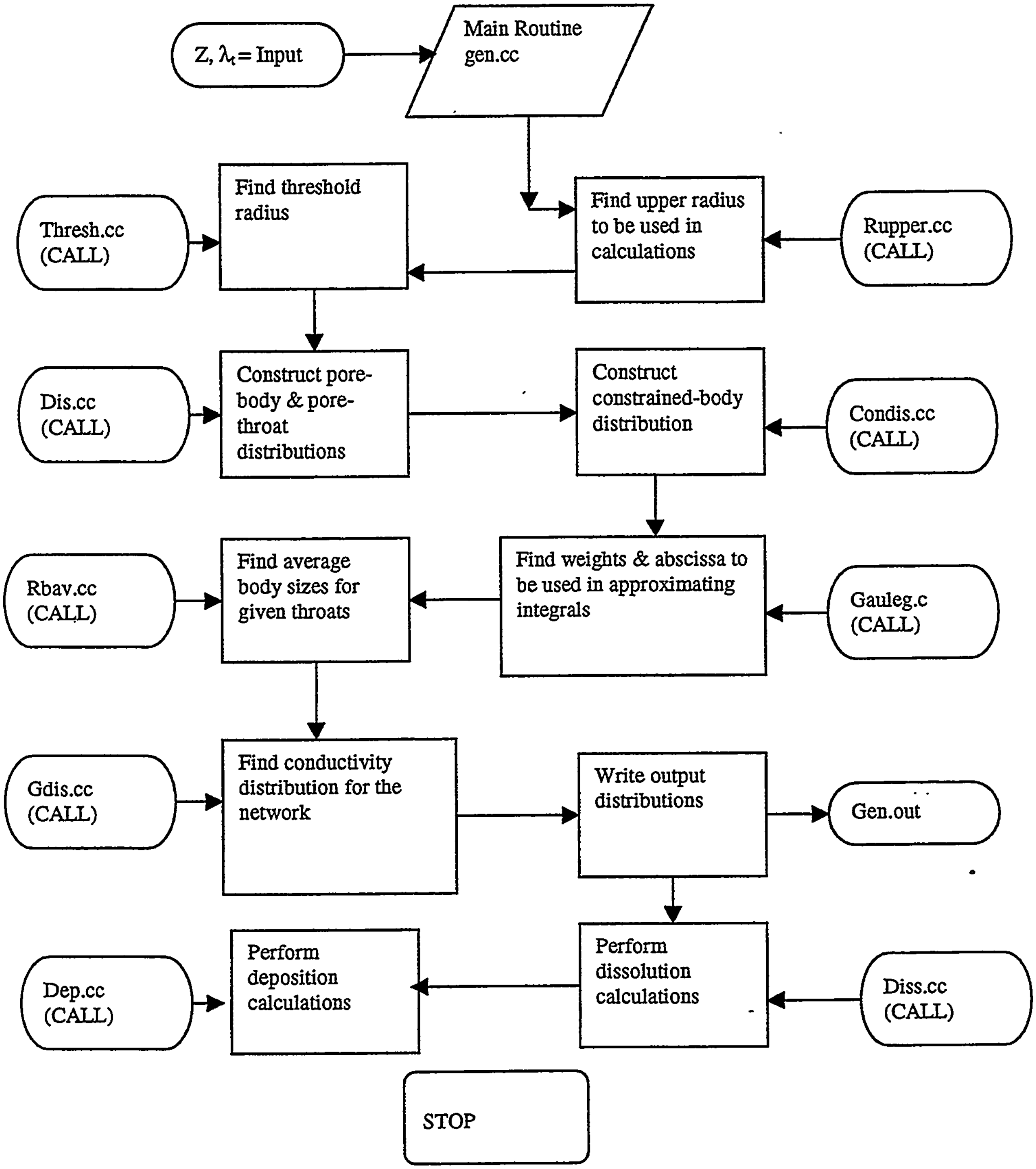

Figure A10.1: Flow chart for main routine.

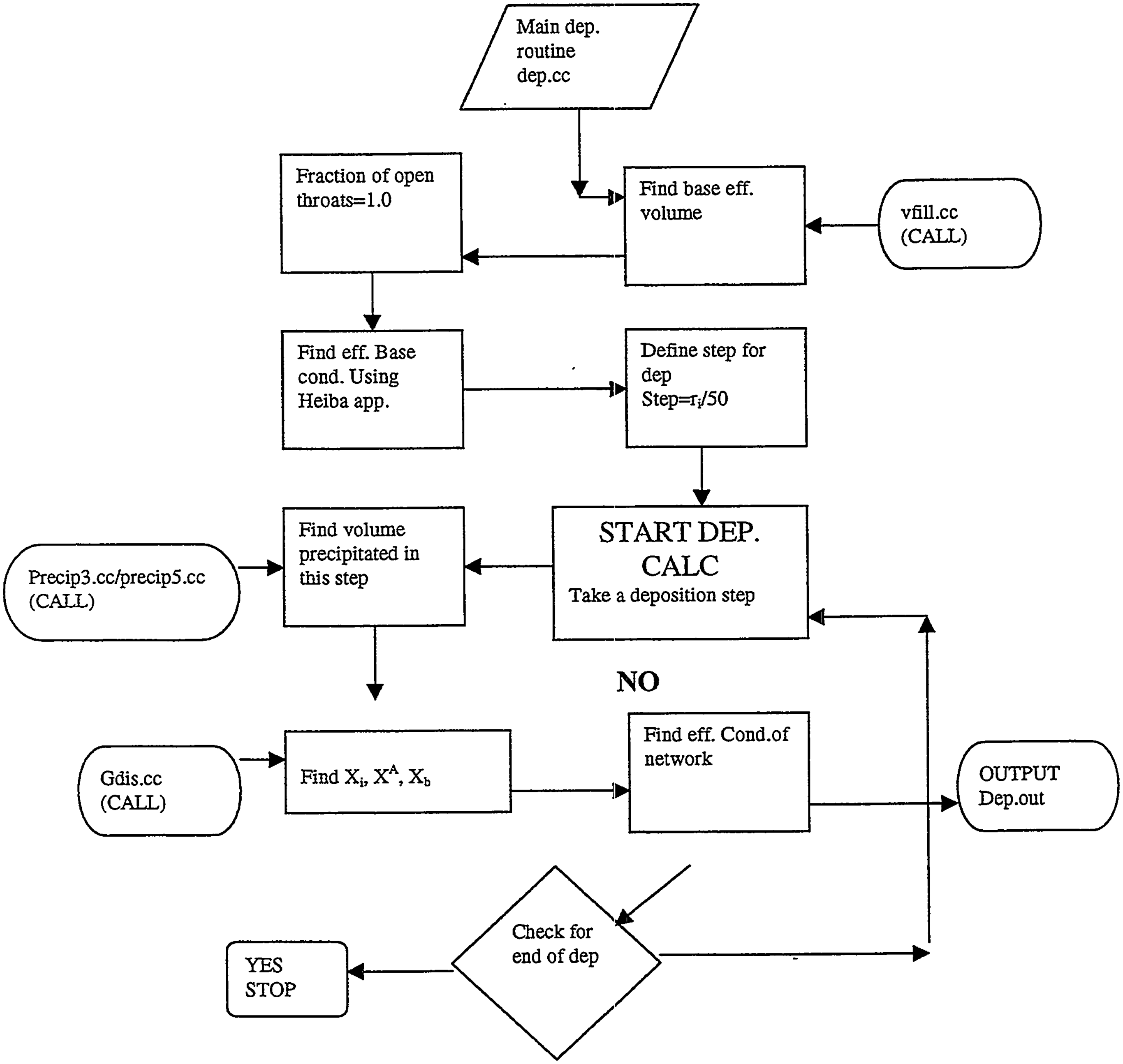

Figure A10.2: Flow chart for deposition routine.

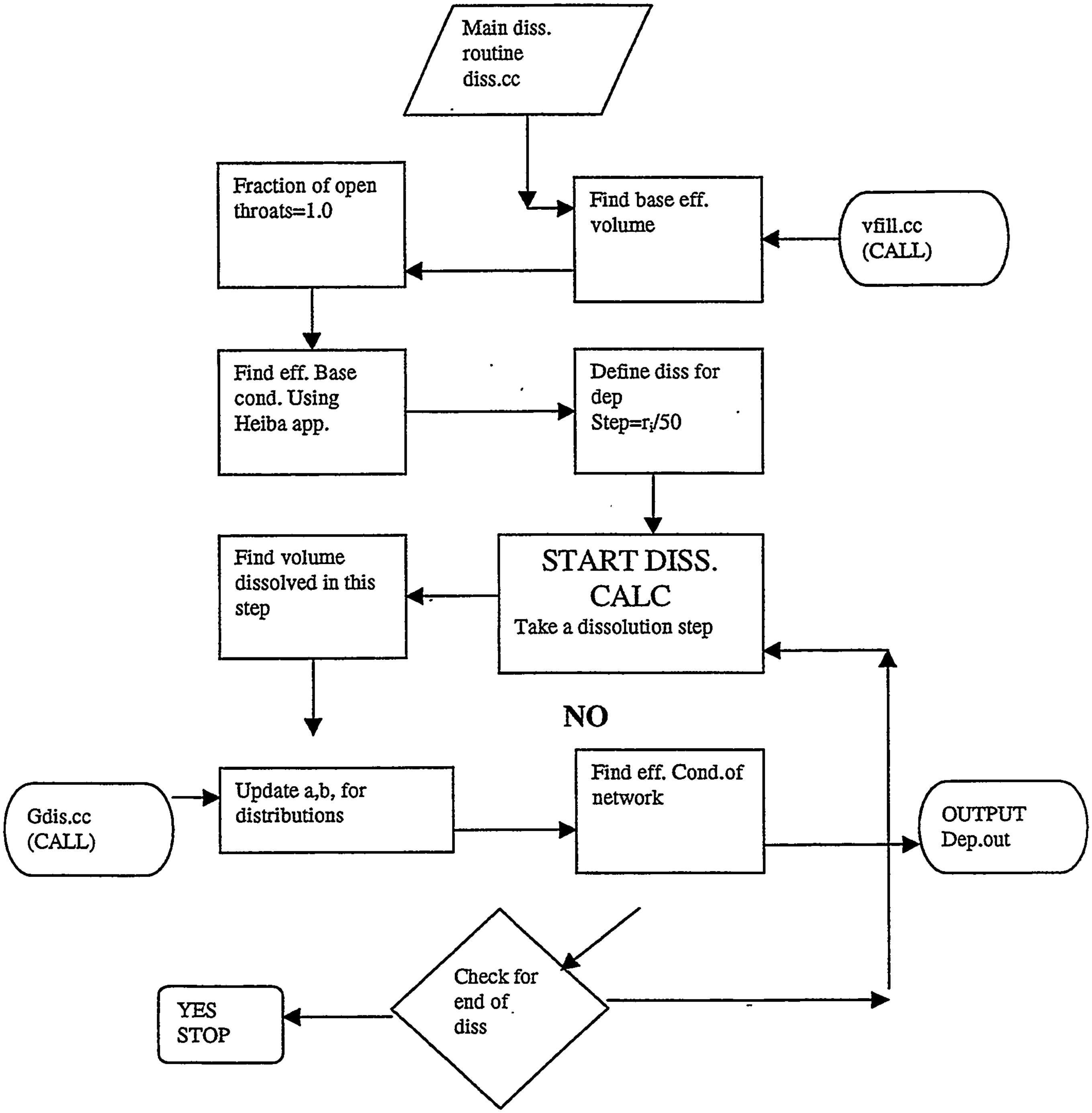

Figure A10.3: Flow chart for dissolution routine.

Appendix XI

Copy of C++ Code of the network model

Please contact the authors at the Petroleum Engineering Department, Stanford University for the code.